Spectral Properties of the One- and Two-Quasi-Particle Channel in the Polarized Phase of the Kitaev Model with External Magnetic Field

MASTER'S THESIS IN PHYSICS

Presented by
Andreas Schellenberger
02.11.2021

INSTITUTE FOR THEORETICAL PHYSICS I
FRIEDRICH-ALEXANDER-UNIVERSITÄT ERLANGEN-NÜRNBERG

Supervised by
Max Hörmann and Prof. Dr. Kai Phillip Schmidt

Abstract

In this thesis the polarized phase of the Kitaev honeycomb model with an external magnetic field is investigated. Using the method of perturbative continuous unitary transformations (pCUTs) in the high-field limit, the properties of the system can be examined for different quasi-particle numbers, independently. Apart from presenting results for the one quasi-particle case for various parameter values of the magnetic field and the Kitaev interactions, the two quasi-particle subspace is investigated to gain insight of the correlated processes of multiple quasi-particles. Using a uniform magnetic field and antiferromagnetic Kitaev couplings, the existence of three anti-bound states in the two quasi-particle sector is shown. The driving mechanism of the anti-bound-state formation is found in the nearest neighbor density-density interactions. By calculating dynamical correlation functions of the one and two quasi-particle subspace, a comparable strong spectral feature is identified with the two quasi-particle anti-bound states, as proposed by Gohlke et al. in their density matrix renormalization group (DMRG) study.

Zusammenfassung

In dieser Arbeit wird die polarisierte Phase des „Kitaev honeycomb“-Modells mit einem externen magnetischen Feld betrachtet. Unter Verwendung der Methode der „perturbative continuous unitary transformations“ (pCUTs) im Limes großer magnetischer Felder, werden die Eigenschaften des Systems für verschiedene Zahlen an Quasi-Teilchen unabhängig voneinander betrachtet. Abgesehen von der Diskussion des Ein-Teilchen-Falls für verschiedene Werte des magnetischen Felds und der Kitaev-Wechselwirkungen, wird der Zwei-Teilchen-Kanal untersucht, um Einblicke in die korrelierten Prozesse mehrerer wechselwirkender Quasi-Teilchen zu erhalten. Unter der Verwendung eines uniformen magnetischen Feldes und antiferromagnetischer Kitaev-Wechselwirkungen wird die Existenz von drei antigebundenen Zuständen im Zwei-Teilchen-Sektor gezeigt. Der entscheidende Mechanismus, der zur Bildung der antigebundenen Zustände führt, ist eine Dichte-Dichte-Wechselwirkung zwischen benachbarten Teilchen. Indem die spektralen Größen wie der dynamische Strukturfaktor im Ein- und Zwei-Teilchen-Raum berechnet werden, kann ein relativ starkes spektrales Merkmal mit den antigebundenen Zuständen identifiziert werden, welches ursprünglich von Gohlke et al. in ihrer „density matrix renormalization group“ (DMRG) Arbeit postuliert wurde.

Contents

Chapter 1

Introduction

In contrast to common belief, the edge of solvable systems is never far away. Especially when noticing all the various processes in nature, which can be described by the numerous fields of science, it seems unimaginable that astonishing simple systems cannot be solved analytically. Probably the most prominent example is the three-body problem [1, 2]. This model inhibits three point particles p_1, p_2, p_3 with individual masses m_1, m_2, m_3 which only interact via Newton's law of gravitation by establishing a force $F_{i,j}$ between two particles p_i, p_j which is proportional to $m_i m_j / r^2$ where r is the distance between the two particles. When looking at the pure simplicity of this system, it is fascinating and perhaps even disturbing that no general analytical solution exists for this three-body system. With this problem in mind, it seems a losing game trying to understand systems with macroscopically many particles interacting with different forces.

The way out of this misery leads to one of the most important 'tools' of physics. As it was impossible to solve the system of differential equations for the general three-body system, the field of research swapped to the investigation of limiting cases [3–5]. A common example is the (restricted) solar system only considering sun, earth, and moon [6]. As the mass of the moon is very small in comparison to the masses of earth and sun, the approximation was made to set $m_{\text{moon}} \approx 0$. The presented system is known as the restricted three-body problem. This limiting case leads to a set of equations thar are much easier to analyze and understand. The focus on a small subset of configurations that are relevant for the physical application to be investigated offers new possibilities to analyze the system which was not solvable before. This approach of reducing configuration space according to the concrete physical problem can be found throughout all fields of physics and is also the foundation for the physical systems we will investigate in this thesis.

When examining solid systems in quantum mechanics we face the same problems as described above. Only armed with the solution of a simple two-particle system (commonly known as the hydrogen atom) [7, chapter 3.5], we have to consider a huge number of atoms (which are hard to tackle for themselves) that interact with each other in various ways. As it is impossible to solve the system in its whole complexity, we have to make assumptions regarding the material.

A possible outcome are so-called *effective models* [8, chapter 1]. These models give us the opportunity to investigate the basic properties of the system and understand them more intuitively as most of the complexity is removed. In our case the two main assumptions are a predefined lattice structure of the materials leading to a description of the system in momentum space (see section 3.1) and only considering magnetic interactions (see section 2.1). The latter is justified by focusing on small temperatures $T \approx 0$ and materials where we can assume localized electrons around the individual atoms [8].

These simplifications result in a quite intuitive way of describing our system. Starting from a system where spins are located on a predefined lattice (in our case a honeycomb lattice) we can define regions in the parameter space called *phases* (as solid, liquid, and gas in the case of water), where the physical properties of the system are roughly the same. An example would be (almost) all spins being aligned in one direction. In these phases, we can define so-called *quasi-particles* (QP) which are an elementary excitation of the respective ground state. This changes our picture in mind from a lattice full of spins pointing in a specific direction to a (normally) almost empty lattice with a few quasi-particles on it. More rigorous information will be given in section 2.3.2 where we introduce the concept of quasi-particles [9, p.1-2]. The dynamics of these quasi-particles is being described by the Hamiltonian when applying second-quantization [8]. For most systems it suffices to restrict the dynamics of the particles only to the adjacent points of the lattice [10]. As last step, we can apply a perturbative continuous unitary transformation (pCUT) to the Hamiltonian [9, 11, 12]. This unitary transformation chooses a new basis where the number of quasi-particles is conserved under application of the Hamiltonian.

Summing up these steps, we are able to describe a very complicated many-body system with interactions as quasi-particles moving locally restricted on a discrete lattice with a conserved number of quasi-particles. The benefit of this picture lies in the more intuitive way of describing excitations of our system. We can map certain features in physical relevant quantities like energy to certain processes of quasi-particles. This results in not only being able to solve the system (for the defined limiting case) but also understanding the physical impact of certain microscopic processes described by quasi-particles.

As pCUT guarantees a constant number of quasi-particles in time evolution, we can investigate the different particle channels (meaning a state with a certain number of quasi-particles in it) separately. Often, we focus only on the one quasi-particle (1QP) sector as this first excitation suffices to describe the physical properties of the system in quite good approximation. The higher quasi-particles channels are normally suppressed and therefore play no major role. Nonetheless, it can be promising to investigate higher particle sectors. When having states with more than one quasi-particle, the individual particles are not described as free particles anymore but can interact with each other. This again gives a new type of process to understand and describe physical quantities which can be measured. Later in this thesis, we will discover two quasi-particles which are closely bound together forming an anti-bound state increasing the energy of the corresponding state. In the following chapters we will examine the one and two quasi-particle sector and will investigate the impact of the quasi-particle interactions in 2QP in more detail (see section 4.2).

The fundamental approach of investigating limiting cases and using approximations mentioned at the beginning will go along with this thesis. We will use several assumptions to get to the structure of quasi-particles as described above, approximate the physical quantities with a series expansion and extrapolate results using physical arguments. Some of those assumptions will also break down for certain parameter values, as will be discussed in section 4.2.2. But overall, these claims let us calculate physical quantities of our system and understand the microscopic reasons for the macroscopic structure of our investigated model.

In the following, we first introduce the model which we will investigate in chapter 2. First, we give an overview of the original 'Kitaev honeycomb model' as it was written down by Kitaev [13]. We will add an external magnetic field to restrict ourselves to 'strong' fields and define the quasi-particles in this phase. After the definition of the model, we go on with the discussion of the methods we use for handling the model in chapter 3. Most prominently, we will introduce the pCUT method to ensure the conservation of quasi-particles as stated above. With methods and model defined, we go on with the discussion of the results in chapter 4. This chapter is divided into the 1QP (see section 4.1) and 2QP (see section 4.2) discussion. The discussion is focused on the dispersion of the polarized phase and basic spectral quantities. At the end we will compare our results to those of some density matrix renormalization group (DMRG) calculations [14] with the focus on identifying the impact of the 2QP sector. Lastly, chapter 5 sums up the results and gives an outlook for further steps regarding the model.

Chapter 2

Kitaev model in a field

This thesis focuses on the so-called *Kitaev honeycomb model*, which was introduced by Kitaev in 2006 [13]. The phase diagram of the model consists of exotic phases with topological excitations called *anyons*, as will be discussed in section 2.2. The bare model can be solved exactly, which makes the model attractive, as one can investigate the behavior of the unconventional phases in an analytic manner. Kitaev showed that these anyons can be used in *topological quantum computing*. The main advantage in contrast to other approaches is the protection from decoherence of the installed quantum memory due to the structure of the anyons. For more information see [13] or for a more pedagogical approach [15].

For our Hamiltonian, we will add a magnetic field term (as done in [14, 16–19]). This field is considered to be the dominant contribution of the system, forcing it into the polarized phase which will be introduced in section 2.3. In this section we will define the ground state and the elementary quasi-particle excitations of the polarized phase.

2.1 Hamiltonian

The Kitaev honeycomb model is defined as a system of *spin-1/2* particles. One spin-1/2 particle is described by a two-dimensional Hilbert space $\mathbb{C}^2$ [7, chapter 6]. The measurement of the spin in a certain direction can be performed by the *Pauli-matrices*

$$\sigma^x = \begin{pmatrix} 0 & 1 \\ 1 & 0 \end{pmatrix}, \sigma^y = \begin{pmatrix} 0 & -i \\ i & 0 \end{pmatrix}, \text{ and } \sigma^z = \begin{pmatrix} 1 & 0 \\ 0 & -1 \end{pmatrix} .$$

On the *quantization axis* z, we denote the two outcomes ± 1 as spin up $\uparrow$ and spin down $\downarrow$. For N spin-1/2 particles we operate on the 2^N dimensional Hilbert space $\mathcal{V} = \left(\mathbb{C}^2\right)^N$ with Pauli-matrices σ_i^α acting only on particle i and applying the identity operator on all other particles. The particles are distributed on a 2D plane in a honeycomb lattice, as can be seen in figure 2.1. The honeycomb lattice consists of primitive cells with two particles which are spread on

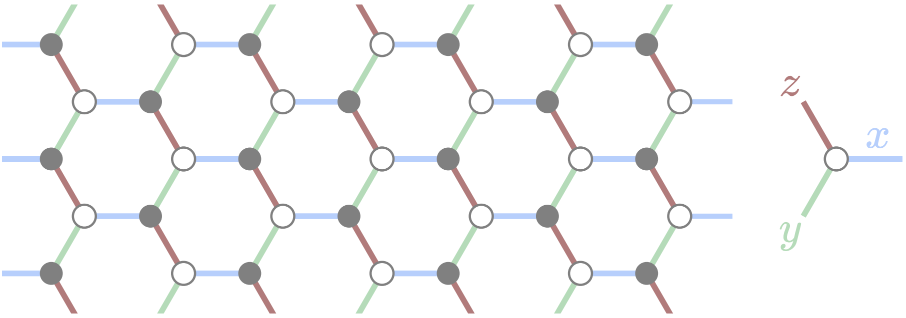

Figure 2.1: Visualization of the Kitaev honeycomb model. The single spin 1/2 particles are located on the vertices of the hexagonal lattice, showed as circles. The gray and white colors of the circles visualize the primitive cell with two sites in it. All spins are coupled to their nearest neighbors following the colored lines. Each line represents one sort of coupling, as defined in equation 2.1.1. The α-coupling with $\alpha \in \{x, y, z\}$ couples the α-component of two spins i, j with the Ising-term $\sigma_i^\alpha \sigma_j^\alpha$.

a quadratic lattice, as visualized in the figure. For more information about the formal definition of primitive cells, see section 3.1 in the methods chapter. The individual particles interact with their nearest neighbors (drawn in the figure as colored bonds) as denoted in the following Hamiltonian:

$$H_{\text{Kitaev}} = -J_x \sum_{x-\text{links } i,j} \sigma_i^x \sigma_j^x - J_y \sum_{y-\text{links } i,j} \sigma_i^y \sigma_j^y - J_z \sum_{z-\text{links } i,j} \sigma_i^z \sigma_j^z \,, \quad (2.1.1)$$

where J_x, J_y, J_z are adjustable parameters. It is important to mention that the type of coupling depends on the 'orientation' of the coupling, as can be seen in figure 2.1. Not only the amplitude of the coupling can be set individually with the J_x, J_y, J_z, but also the direction of the spin-coupling differs. Assuming positive J_α for all directions $\alpha \in \{x, y, z\}$, the coupling $\sigma_i^\alpha \sigma_j^\alpha$ is minimized if the α-component of the spins at the locations i, j is parallel to each other. As *Heisenberg's uncertainty principle* holds, we can not probe the spins in our model in such a way that they fulfill all couplings at the same time optimally. So, not all terms in the Hamiltonian can be minimized at once. This effect is called *frustration* and is the key mechanism to let the model realize highly non-trivial quantum-phases [13, 20].

For this thesis we add a magnetic field term to the Hamiltonian H_{Kitaev}. The magnetic field is of arbitrary direction and interacts with all spins due to their intrinsic magnetic moment $\mu \propto \vec{\sigma}$ where $\vec{\sigma} = (\sigma^x, \sigma^y, \sigma^z)^T$ is the vector of the Pauli matrices. We obtain

$$H = H_{\text{field}} + H_{\text{Kitaev}} = - \sum_{i,\, \alpha \in \{x,y,z\}} h_\alpha \sigma_i^\alpha - \sum_{\substack{\alpha\text{-links } i,j \\ \alpha \in \{x,y,z\}}} J_\alpha \sigma_i^\alpha \sigma_j^\alpha \quad (2.1.2)$$

as our new Hamiltonian, where $\vec{h} = (h_x, h_y, h_z)^T$ is the magnetic field vector. For applying the pCUT method, we need to have our H_{field} term in diagonal form (for more information why this is needed, see section 3.2). For doing so, we construct a unitary transformation U which transforms H_{field} into the desired shape, reading

$$U^\dagger H_{\text{field}} U = \sum_i \begin{pmatrix} \lambda_+ & 0 \\ 0 & \lambda_- \end{pmatrix}_i ,$$

where $\lambda_\pm = \pm\sqrt{h_x^2 + h_y^2 + h_z^2}$ are the eigenvalues of the 2x2-matrix describing the interaction of the magnetic field with one particle i. The eigenvalues are proportional to the magnitude $h := \sqrt{h_x^2 + h_y^2 + h_z^2}$ of the magnetic field. When applying U on H in equation 2.1.2, we rotate the Kitaev part to match with our diagonalized field term. We obtain

$$\mathcal{H} = U^\dagger H U = \mathcal{H}_{\text{field}} + \mathcal{H}_{\text{Kitaev}} = -h \sum_i \sigma_i^z - \sum_{\substack{\alpha\text{-links } i,j \\ \alpha,\beta,\gamma \in \{x,y,z\}}} \frac{1}{h^2} J_\gamma C_\gamma^{\alpha\beta} \sigma_i^\alpha \sigma_j^\beta \tag{2.1.3}$$

with three matrices C_x, C_y, C_z where $C_\gamma^{\alpha\beta}$ denotes the corresponding entry in the 3x3 matrix C_γ. When we calculate $U^\dagger H_{\text{Kitaev}} U$ we get the C_γ matrices of the form

$$C_x = \frac{1}{h_x^2 + h_y^2} \begin{pmatrix} h_x^2 h_z^2 & -h_x h_y h_z h & h_x^2 h_z \sqrt{h_x^2 + h_y^2} \\ -h_x h_y h_z h & h_y h & h_x h_y h \sqrt{h_x^2 + h_y^2} \\ h_x^2 h_z \sqrt{h_x^2 + h_y^2} & h_x h_y h \sqrt{h_x^2 + h_y^2} & h_x^2 \end{pmatrix}$$

$$C_y = \frac{1}{h_x^2 + h_y^2} \begin{pmatrix} h_y^2 h_z^2 & h_x h_y h_z h & h_y^2 h_z \sqrt{h_x^2 + h_y^2} \\ h_x h_y h_z h & h_x^2 h & h_x h_y h \sqrt{h_x^2 + h_y^2} \\ h_y^2 h_z \sqrt{h_x^2 + h_y^2} & h_x h_y h \sqrt{h_x^2 + h_y^2} & h_y^2 \end{pmatrix}$$

$$C_z = \begin{pmatrix} h_x^2 + h_y^2 & 0 & -h_z \sqrt{h_x^2 + h_y^2} \\ 0 & 0 & 0 \\ -h_z \sqrt{h_x^2 + h_y^2} & 0 & h_z^2 \end{pmatrix} .$$

Most of the time we will restrict ourselves to the case of an *uniform* magnetic field $\vec{h} = (1, 1, 1)^T$ and uniform *antiferromagnetic* interactions $J_x = J_y = J_z < 0$. This follows the standard in literature for the Kitaev model in a magnetic field [14, 16, 17, 21, 22].

Before changing the notation of the Hamiltonian to second quantization by introducing creation and annihilation-operators, we will give a short overview of the phase diagram—with and without the magnetic field.

2.2 Overview of the phase diagram

As mentioned before, what makes the Kitaev-honeycomb model especially interesting is the possibility of solving its ground-state phase diagram analytically. The following paragraphs shall give an overview over the most important steps,

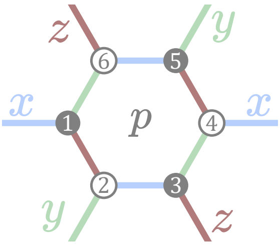

Figure 2.2: Visualization of one plaquette p, defined as one hexagon of the honeycomb lattice. On every plaquette we can define a operator $W_p = \sigma_1^x \sigma_2^y \sigma_3^z \sigma_4^x \sigma_5^y \sigma_6^z$ acting on the spins in the plaquette. This operator commutes with all other plaquette operators $W_{p'}$ with $p' \neq p$ and with the Hamiltonian.

for more information see Kitaev's paper, which also includes many more information about the structure and mathematical foundation of his findings [13].

When starting with the original model without an external magnetic field in equation 2.1.1, one can introduce a *plaquette operator* $W_p = \sigma_1^x \sigma_2^y \sigma_3^z \sigma_4^x \sigma_5^y \sigma_6^z$ with the Pauli-matrices acting on the spins around a hexagonal plaquette p, as visualized in figure 2.2. These W_p commute with each other and also commute with the Hamiltonian. This simplifies the search for eigenstates of the Hamiltonian by dividing the total Hilbert space into eigenspaces of the individual W_p. The possible eigenvalues for W_p are $w_p = \pm 1$. One can show with Lieb's theorem [23] that the state with minimum energy must fulfill $w_p = 1$ for all plaquettes on the lattice, called vortex-free. Using this result and a transformation of the Pauli matrices to Majorana operators c_i, the Hamiltonian can be rewritten in a quadratic form

$$H_{\text{vortex-free}} = \frac{i}{2} \sum_{\substack{\alpha\text{-links } i,j \\ \alpha \in \{x,y,z\}}} J_\alpha c_i c_j \,. \tag{2.2.1}$$

Because of the new Hamiltonian's translational invariance, $H_{\text{vortex-free}}$ can be diagonalized with a Fourier transformation, which will be discussed in general in section 3.1. The energy of a Majorana fermion excitation above the ground state is given by

$$\varepsilon(q) = \pm 2 |J_x e^{i\phi_1(q)} + J_y e^{i\phi_2(q)} + J_z| \,, \tag{2.2.2}$$

where $\phi_1(q), \phi_2(q)$ are phases depending on the momentum q. The overall phase diagram is characterized by whether the spectrum $\varepsilon(q)$ is gapless—meaning $\varepsilon(q) = 0$ for at least one q—or not. It turns out that the spectrum is gapless if and only if the triangle inequalities

$$|J_x| \leq |J_y| + |J_z|, \quad |J_y| \leq |J_x| + |J_z|, \quad |J_z| \leq |J_x| + |J_y| \tag{2.2.3}$$

are fulfilled. The spectrum can be visualized as a triangle of constant with $J_x + J_y + J_z = 1$ as done in figure 2.3. The edges of the triangle set one of the J_α parameters to zero and the corners of the triangle stand for only one not vanishing parameter $J_\alpha = 1$, respectively. Phase B in the center of the phase diagram satisfies the inequalities 2.2.3, being a gapless phase as motivated by

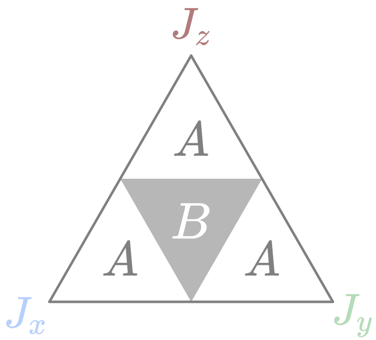

Figure 2.3: Ground state phase diagram of the Kitaev honeycomb model as defined in equation 2.1.1. The triangle is defined as the subspace $J_x + J_y + J_z = 1$ with positive J_x, J_y, J_z. The corners of the triangle—denoted with J_x, J_y, J_z—correspond to the limiting cases of only one non-vanishing parameter $J_\alpha = 1$, respectively. For each edge of the triangle one of the three parameters is set to 0. The phases denoted by A are gapped phases. The phase B in the middle fulfilling equation 2.2.3 is a gapless phase.

equations 2.2.2 and 2.2.3. The other phases denoted by A are gapped phases, meaning the fermionic excitation has a finite energy.

Above the ground state of the gapped A phases are two types of elementary excitations called electric charges and magnetic vortices. These excitations inhibit anyonic statistics, distinguishing them from fermions or bosons which only acquire a phase factor of -1 or $+1$ under particle exchange, respectively. In the case of these anyon excitations, we get a non-trivial phase when moving one particle around another. These 'moving' operations are called *braiding*, meaning due to the non-trivial phase the movement of the particles around each other is encoded in the phase of the state. For the gapless B phase this is not directly possible, as the correlations between different quasi-particles does not decay exponentially with distance which is needed for braiding operations.

As outlined above, the main difference of phase A and B lies in the gapped or gapless spectrum of the fermionic excitations, respectively. Even though the gapless spectrum of phase B is protected against perturbations that are symmetric regarding time-reversal, it can be broken by an external magnetic field as introduced in equation 2.1.2. Doing perturbation theory on the effective Hamiltonian in equation 2.2.1, a gap opens in third order being proportional to $(h_x h_y h_z)/J^2$ with $J := J_x = J_y = J_z$. The acquired gap gives rise to non-abelian anyons. Their braiding is not just described by non-trivial phase factors but a multidimensional 'braid group' [13, chapter 8]. When turning the magnetic field to larger $|\vec{h}|$, we expect another phase transition to the topologically trivial *polarized phase* where all spins are aligned with respect to the magnetic field direction.

Following Kitaev's arguments, this model can be used for *topological quantum computation*, where quantum gates can be realized using braiding. The therefore needed non-abelian anyons are obtained for phase B with an infinitesimal magnetic field. The main advantage in comparison to other approaches is the protection from decoherence for the quantum information encoded in the system. This should make the scalability of topological quantum computation

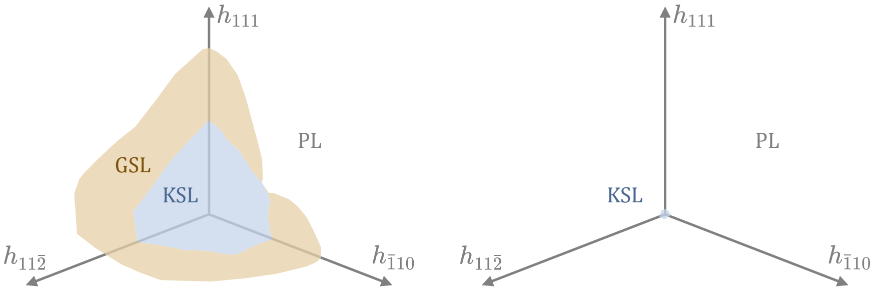

Figure 2.4: Phase diagram of the Kitaev honeycomb model in a magnetic field as defined in equation 2.1.2. The Kitaev coupling is fixed at $J := J_x = J_y = J_z$ resulting in phase B for vanishing magnetic field in figure 2.3. The magnetic field strength and direction is varied. The left plot is made for an antiferromagnetic coupling $J < 0$ the right one for ferromagnetic coupling $J > 0$. For $J < 0$ the phase diagram consists of three phases, starting with the gapped Kitaev spin liquid (KSL), over the gapless spin liquid (GSL), to the polarized phase (PL). For $J > 0$ the GSL phase was not detected and the phase transition from KSL to PL takes place for way smaller magnetic fields. The phase diagram was examined by [17] and was adopted for this thesis.

easier than for other systems (like superconducting quantum computing [24] or trapped ion quantum computing [25]) that have to work with error correction routines to deal with the problem of decoherence [26].

The rough overview of the phase diagram can be examined in more detail, as done by Hickey and Trebst [17, 27] for varying $\vec{h}$ and fixed J using exact diagonalization (ED) or by Gohlke, Moessner, and Pollmann using the density matrix renormalization group (DMRG) [14]. The surprise was the discovery of an additional phase between the gapped Kitaev phase—called Kitaev spin liquid (KSL)—and the polarized phase (PL), as can be seen in figure 2.4. For antiferromagnetic couplings $J < 0$ and certain directions of the magnetic field (as $\hat{h} = (1, 1, 1)^T$) an intermediate gapless phase—called gapless spin liquid (GSL)—was observed for moderate magnetic fields. For ferromagnetic interactions $J > 0$, the GSL does not appear and the KSL transitions to the PL phase for magnetic fields an order of magnitude lower as for antiferromagnetic couplings. The new-found GSL phase is expected to be a gapless quantum spin liquid as the density of low-energy states is drastically increased in contrast to the KSL and PL phases [17, figure 3]. Apart from ED and DMRG there are also different approaches to calculate physical quantities of such strongly entangled systems. One such ansatz is using a quantum simulation (QS) to access such quantities as the ground state [28, 29]. The advantage can be a way better scalability, as we can use the quantum nature of the qubits. Recently, Bespalova and Kyriienko proposed a quantum protocol to obtain the ground state of the Kitaev honeycomb model with and without a magnetic field, potentially opening another way to study the phase diagram [30].

Apart from the Kitaev couplings J_α and the magnetic field $\vec{h}$ there are additional parameters which can be varied. In [27] the lattice was varied to the structure of the decorated honeycomb and the square octagon. Also for these lattices each spin interacts with three nearest neighbors with the three spatial dimensions of the spin. Another variation can be done for the used particles itself. For this thesis we have defined the system containing spin-1/2 particles. As described at the beginning of section 2.1, the spin-1/2 particles are defined on the Hilbert space $\mathbb{C}^2$, thus having two possible values under measurement. This property can be modified by going to higher spin values. The Kitaev honeycomb model was investigated with a magnetic field for spin 1 particles by [31] using DMRG calculation and by [32] using ED. In contrast to our case, the ground state of the pure Kitaev model without an magnetic field can not be found analytically. As for spin 1/2, they found a gapless phase between the Kitaev spin liquid and the polarized phase for antiferromagnetic interactions. Also for the ferromagnetic J the phase transition from the KSL phase to the polarized phase happens like for the spin 1/2 case. The further investigation of higher spin numbers as 3/2 in [33] is of current interest.

To sum things up, this shall give a rough overview of the phase diagram for varying $\vec{J}$ and $\vec{h}$ parameters. In the following, we will restrict ourselves to the polarized phase with $\|\vec{h}\| \gg \|\vec{J}\|$. Starting from the limit $\vec{J} = 0$, we will establish the Kitaev couplings as a perturbation of our system in a magnetic field. We will only loosely touch the other phases when talking about the gap in the polarized phase. So, for the rest of this model chapter we will concentrate on the polarized phase and its ground state and elementary excitations.

2.3 The polarized phase

After giving a rough overview over the whole phase diagram, from now on we will concentrate on the polarized phase (PL) with $\|\vec{h}\| \gg \|\vec{J}\|$. We will also use the shorthand notation $h \gg J$ to rank the strength of the two parameters. In this section we will investigate the ground state and the elementary excitations in this limit of large magnetic fields. For the description of these excitations above the ground state, we will transform our Hamiltonian in equation 2.1.2 using second quantization, interpreting the excitations as quasi-particles.

The structure of the Hamiltonian after transformation is appropriate for the pCUT method. This will give us the opportunity to separate the single quasi-particle channels (meaning the number of quasi-particles) from each other and discuss them separately. We will introduce the pCUT method with its prerequisites in section 3.2.

2.3.1 Ground state

When setting the Kitaev interactions $J_x = J_y = J_z = 0$, the Hamiltonian in equation 2.1.2 reduces to non-interacting spins in a uniform magnetic field, reading

$$H_{\text{field}} = - \sum_{i,\, \alpha \in \{x,y,z\}} h_\alpha \sigma_i^\alpha \,.$$

As introduced in section 2.1, we denote the state of a spin on a site as $|\uparrow\rangle$ if $\sigma^z |\uparrow\rangle = +1 |\uparrow\rangle$ and $|\downarrow\rangle$ if $\sigma^z |\downarrow\rangle = -1 |\downarrow\rangle$. We see from the form of the Hamiltonian H_{field} that the energy of the system is minimized if all spins are oriented along the magnetic field. To simplify notation and calculations we rotate our system to align the magnetic field along the z-axis, as we did in equation 2.1.3. In the limit of no Kitaev interactions the rotated Hamiltonian is already diagonal and reads

$$\mathcal{H}_{\text{field}} = -h \sum_i \sigma_i^z \, . \tag{2.3.1}$$

For a state of minimal energy, all spins have to point upwards to get a -1 eigenvalue for each summand in the Hamiltonian. So, we can define the unique *ground state* as $|\Uparrow\rangle := |\uparrow\uparrow\cdots\rangle$ with all spins pointing upwards along the rotated magnetic field, where $|\uparrow\uparrow\cdots\rangle \in \mathcal{V}$ is a state in the Hilbert space of all spins $\mathcal{V} = \left(\mathbb{C}^2\right)^N$. We can calculate the energy of $|\Uparrow\rangle$ for vanishing Kitaev couplings directly as

$$E_0 = \langle\Uparrow| \, \mathcal{H}_{\text{field}} \, |\Uparrow\rangle = -hN \, .$$

It is easy to prove that a spin-flip of any of the spins in $|\Uparrow\rangle$ raises the energy of the state. This statement ensures that we have found the only ground state for the system in the limit $J = 0$. We suppose that we stay in the polarized phase and $|\Uparrow\rangle$ is adiabatically connected to the actual ground state of the system when adding the Kitaev model as a small perturbation $J \ll h$. This follows from the gapped spectrum of $\mathcal{H}_{\text{field}}$ in equation 2.3.1 which we will discuss in the following section. From now on we denote $\mathcal{H}_{\text{field}}$ as the *unperturbed Hamiltonian* and $\mathcal{H}_{\text{Kitaev}}$ as the *perturbation*.

2.3.2 Quasi-particles

After introducing the ground state $|\Uparrow\rangle$, we now discuss the elementary excitations in the polarized phase, meaning states whose energy is increased minimally with respect to the ground state energy E_0.

As the unperturbed Hamiltonian is already in diagonal form after rotation, we can easily calculate the spectrum and the corresponding eigenstates. The possible eigenvalues of $\mathcal{H}_{\text{field}}$ are

$$E_k := -h(N + 2k) \quad k \in \{0, 1, \ldots, N\} \, ,$$

with the corresponding eigenspaces

$$\mathcal{V}_k := \text{span}(\{|s\rangle \mid k \text{ spins} \downarrow , \text{ rest} \uparrow\}) \, . \tag{2.3.2}$$

As can be seen, the eigenenergies E_k behave like a shifted harmonic oscillator, with $k = 0$ being the ground state, $k = 1$ being the first excitation, $k = 2$ the second, and so on. Thus it is convenient to introduce creation and annihilation operators $b^\dagger, b$ in second quantization to describe the excitation levels denoted by k, done with the *Matsubara-Matsuda transformation* [34]. This transformation identifies one spin down at position i with one quasi-particle that is created and annihilated with $b_i^\dagger, b_i$. So, the creation $b_i^\dagger$ of a quasi-particle corresponds to the flipping of the spin at position i from up to down and vice versa for the annihilation operator b_i. We can visualize this transformation as done in

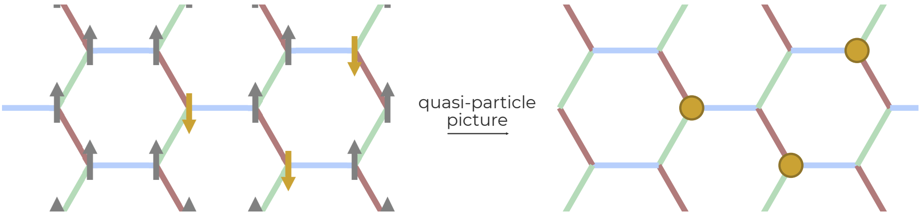

Figure 2.5: Visualization of the quasi-particle picture. The original model is defined in terms of spin 1/2 particles at all sites. The two possible configurations are spin up ↑ and spin down ↓. From $\mathcal{H}_{\text{field}}$ we see that a spin down increases the overall energy. As the energy increases linearly when flipping spins, we can treat all spin downs as quasi-particles moving on an empty lattice. Each empty site in the quasi-particle picture corresponds to a spin up, meaning a particle in the ground state with respect to the field Hamiltonian.

figure 2.5 by going from the 'real' material consisting of spins to the second quantization image with quasi-particles at the sites with spin down.

The defined quasi-particles fulfill the *hardcore boson* statistics. This means that only one particle can occupy each site on the lattice (as there is no 'double down spin') but the exchange of two particles obeys the *boson statistics*. In formulars this reads

$$b_i b_i = b_i^\dagger b_i^\dagger = 0 \quad [b_i, b_j^\dagger] = \delta_{ij}(1 - 2n_i)\,, \tag{2.3.3}$$

with $n_i := b_i^\dagger b_i$ being the number-operator and δ_{ij} the Kronecker delta. As we have identified spin flips with $b^\dagger, b$, we can rewrite the Pauli matrices in terms of these creation and annihilation operators as

$$\sigma_i^x = b_i^\dagger + b_i, \quad \sigma_i^y = i(b_i - b_i^\dagger), \quad \sigma_i^z = 2n_i - 1\,. \tag{2.3.4}$$

Using these rules we can express our unperturbed Hamiltonian $\mathcal{H}_{\text{field}}$ in second quantization as

$$\mathcal{H}_{\text{field}} = -h(N - 2\sum_i n_i)\,.$$

This form of the Hamiltonian gives us the above discussed insight in a more intuitive way. Starting with an energy of $-hN$ in the ground state, each quasi-particle—counted with n_i—adds an energy of $2h$.

For normalization reasons, we want our quasi-particles to add an energy of 1 to the system. So, from now on we will look at a new Hamiltonian divided by $2h$. To keep notation neat, we will use the same term $\mathcal{H}_{\text{field}}$ for this normalized Hamiltonian, which is an abuse of notation.

For further discussions of the various quasi-particle channels we introduce a general notation for the n *quasi-particle states* in the following way: We denote $|n, i_1, i_2, \ldots, i_n\rangle$ as a state with n quasi-particles in it located at the positions $i_1, i_2, \ldots, i_n$. Such a state lives in the (transformed) eigenspace $\mathcal{V}_n$ introduced in equation 2.3.2. For discussion, we will only be interested in the ground state $|0\rangle$, and the 1QP and 2QP channels $|1, i_1\rangle\,, |2, i_1, i_2\rangle$ in the sections 4.1 and 4.2, respectively.

As simple as the description of the unperturbed system got with the transformation, it is interesting to look at the complete Hamiltonian $\mathcal{H}$ from equation 2.1.3 in second quantization. For doing so, we apply the Matsubara-Matsuda transformation from equation 2.3.4 on the perturbation part, too. We will write the Hamiltonian already in the form needed to apply pCUT on it, dividing up the perturbative part into different number of quasi-particles which get created or annihilated during the respective process. We denote these terms as T_n, with n being the number of particles to be created for $n > 0$ or annihilated for $n < 0$. As further notation, we introduce $t_n^\alpha(i,j)$ as a process with n created or annihilated particles on the sites i, j that are connected with an α-interaction. As result we get

$$\begin{aligned}\mathcal{H} &= -\frac{N}{2} + \sum_i n_i + T_0 + T_{\pm 1} + T_{\pm 2} \\ &= -\frac{N}{2} + \sum_i n_i + \sum_{\substack{\alpha\text{-links } i,j \\ \alpha\in\{x,y,z\}}} t_0^\alpha(i,j) + t_{\pm 1}^\alpha(i,j) + t_{\pm 2}^\alpha(i,j)\end{aligned} \tag{2.3.5}$$

with the following t-operators

$$\begin{aligned}t_0^\alpha(i,j) &= J_\alpha C\left[h_\alpha^2(1-2n_j-2n_i+4n_in_j) + (h_\beta^2+h_\gamma^2)(b_i^\dagger b_j + b_i b_j^\dagger)\right] \\ t_{-1}^x(i,j) &= J_x C\left(\frac{h_x^2 h_z + i h_x h_y h}{\sqrt{h_x^2+h_y^2}}\right)(b_i + b_j - 2b_i n_j - 2b_j n_i) \\ t_{-1}^y(i,j) &= J_y C\left(\frac{h_y^2 h_z - i h_x h_y h}{\sqrt{h_x^2+h_y^2}}\right)(b_i + b_j - 2b_i n_j - 2b_j n_i) \\ t_{-1}^z(i,j) &= J_z C(-h_z\sqrt{h_x^2+h_y^2})(b_i + b_j - 2b_i n_j - 2b_j n_i) \\ t_{-2}^x(i,j) &= J_x C\left(\frac{h_x^2 h_z^2 - h_y^2 h^2 + 2i h_x h_y h_z h}{h_x^2+h_y^2}\right) b_i b_j \\ t_{-2}^y(i,j) &= J_y C\left(\frac{h_y^2 h_z^2 - h_x^2 h^2 - 2i h_x h_y h_z h}{h_x^2+h_y^2}\right) b_i b_j \\ t_{-2}^z(i,j) &= J_z C(h_x^2+h_y^2) b_i b_j\,,\end{aligned} \tag{2.3.6}$$

using $C := -\frac{1}{2h^3}$ as global coefficient for all perturbation terms and $\beta \neq \gamma \neq \alpha$ being the three different directions x, y, z. Furthermore, for the creation terms $t_n^\alpha(i,j)$ with $n > 0$ stands

$$t_n^\alpha(i,j) = \left[t_{-n}^\alpha(i,j)\right]^\dagger\ .$$

We see that for $\mathcal{H}$ we can create and annihilate up to 2 particles. In contrast to the unperturbed Hamiltonian this means that the quasi-particle number is not conserved. So, it is not possible to investigate single quasi-particle sectors, as they are coupled to each other. To eliminate these couplings between the different QP sectors, we will use the pCUT transformation, which is introduced in section 3.2.

For most of the discussion we will restrict the configuration space to a uniform magnetic field $h_x = h_y = h_z = 1$. This simplifies the t-operators to

$$\begin{aligned}
t_0^\alpha(i,j) &= J_\alpha C\left[(1-2n_j-2n_i+4n_in_j)+2(b_i^\dagger b_j+b_ib_j^\dagger)\right]\\
t_{-1}^x(i,j) &= J_xC\left(\frac{1+i\sqrt{3}}{\sqrt{2}}\right)(b_i+b_j-2b_in_j-2b_jn_i)\\
t_{-1}^y(i,j) &= J_yC\left(\frac{1-i\sqrt{3}}{\sqrt{2}}\right)(b_i+b_j-2b_in_j-2b_jn_i)\\
t_{-1}^z(i,j) &= -J_zC\sqrt{2}(b_i+b_j-2b_in_j-2b_jn_i)\\
t_{-2}^x(i,j) &= J_xC(-1+i\sqrt{3})b_ib_j\\
t_{-2}^y(i,j) &= J_yC(-1-i\sqrt{3})b_ib_j\\
t_{-2}^z(i,j) &= 2J_zCb_ib_j\ ,
\end{aligned}$$

with $C := -\frac{1}{6\sqrt{3}}$. When looking at the prefactors of the operators in $t_n^\alpha(i,j)$ for fixed n, we see that the absolute value for different α is the same. Only the phase of the complex number is different. This corresponds to the symmetry of setting all h_α to the same value and can simplify calculations with the model.

Chapter 3

Methods

After giving an introduction to the Kitaev honeycomb model in a magnetic field, in this chapter we will introduce the techniques to calculate and analyze physical quantities like the energy of different states and dynamical correlation functions. The first important tool we will use is the Fourier transformation which will be introduced in section 3.1. As outlined in the introduction, the main difficulty one has to overcome when calculating quantities of a model for a solid-state system is the macroscopical number of involved particles. The crucial idea to deal with this problem is the repeating pattern of positions of the particles introduced as a lattice. This *translational invariance* can be used to effectively reduce the degrees of freedom by moving from real to momentum space and using the total momentum conservation.

As introduced in section 2.3, we treat the Kitaev interactions as perturbation to the magnetic field. For doing so, we use the pCUT method which we will introduce in section 3.2 to calculate a *perturbation series* with the J_x, J_y, J_z as *perturbation parameters*, having $|J_\alpha| \ll |h|$. Furthermore, the pCUT method enables us to look at the single quasi-particle sectors independently. For making the calculation of the perturbation series feasible, we will use the *linked cluster theorem* which ensures that we can extract physical quantities in the *thermodynamic limit* $N \to \infty$ by only calculating on finite clusters.

As we are not only interested in the ground states behavior when applying the perturbation but in the one and two quasi-particle sector, too, we will introduce options to calculate the different particle sectors and compare them via the free particle approximations in the sections 3.2.3 and 3.3.

It is important to have in mind that the calculated series are only ensured to be valid in the limit $J_\alpha \ll h$. We will max out this limit by choosing large J_α and run into some problems, which will be discussed in section 4.2.2. To enlarge the area of convergence, we will calculate the perturbation series in high order and use extrapolation techniques. For doing so, we will concentrate on the so-called Padé and dlog-Padé methods, which are introduced in section 3.4.

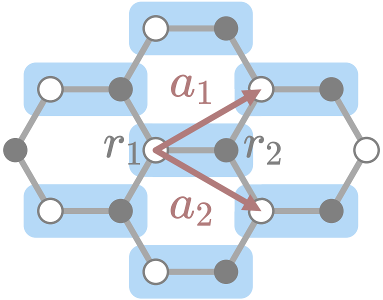

Figure 3.1: Visualization of the honeycomb lattice. The chosen primitive cell from the main text is marked in blue. The primitive cell consists of two sites at the positions r_1, r_2. We can construct the lattice by adding the two lattice vectors a_1, a_2 with arbitrary coefficients in $\mathbb{Z}$.

3.1 Fourier transformation

As outlined before, the Fourier transformation uses the special ordering of the particles in a model. As we assume for our model that the spins are distributed on a defined lattice structure also our defined quasi-particles from section 2.3.2 are located on that structure.

First, we introduce some general nomenclature. A lattice structure starts with a *unit cell*. The unit cell can be basically of any shape and is defined in that way that repeating the unit cell in defined directions (called *lattice vectors*) gives us back the complete lattice structure. Furthermore, we define the *primitive cell* as the smallest possible unit cell. More formally, our unit cell consists of $u \in \mathbb{N}$ sites at the positions $r_1, \ldots, r_u$. We define the linear independent lattice vectors $a_1, \ldots, a_l$, with $l \in \mathbb{N}$ determining the dimensionality of the lattice. We repeat the structure of the unit cell by writing down the set of all sites of the lattice $\mathcal{S}$ as

$$\mathcal{S} = \{r_i + \sum_{k=1}^{l} C_k a_k \mid i \in \{1, \ldots, u\}, C_k \in \mathbb{Z}\} . \tag{3.1.1}$$

This means, we choose a specific unit cell with the term $R_{C_1,\ldots,C_l} := \sum_{k=1}^{l} C_k a_k$ and specify the site in this specific cell with r_i. In our case of the honeycomb lattice we have $u = l = 2$ with the primitive cell vectors

$$r_1 = (0,0)^T, r_2 = (2,0)^T \tag{3.1.2}$$

and the lattice vectors

$$a_1 = (3, \sqrt{3})^T, a_2 = (3, -\sqrt{3}) \tag{3.1.3}$$

as shown in figure 3.1. The vectors are chosen in an appropriate length scale.

Furthermore, we define the *reciprocal lattice* as the Fourier transform of the lattice in real space defined above. We choose to name our lattice vectors $b_1, \ldots, b_l$, being of the same number as those from the original lattice. Using the definition $G_{D_1,\ldots,D_l} := \sum_{k=1}^{l} D_k b_k$ with $D_k \in \mathbb{Z}$ and the Fourier transform, we observe the condition $G_{D_1,\ldots,D_l} \cdot R_{C_1,\ldots,C_l} \in 2\pi\mathbb{Z}$ as necessary for our lattice vectors in the reciprocal lattice. To fulfill this condition, it suffices to satisfy the condition of the *dual basis*

$$a_i b_j = 2\pi\delta_{ij} \quad \forall i,j \in \{1,\ldots,l\}\,. \tag{3.1.4}$$

We will use the reciprocal lattice vectors later on to define the momentum of the quasi-particles with respect to this basis.

The crucial part that will simplify our calculations is the invariance of our Hamiltonian and the commutation relations under translation of the quasi-particles in terms of $R_{C_1,\ldots,C_l}$. More concrete, having a general n-QP state $|n,i_1,\ldots,i_n\rangle$, as defined in section 2.3.2, we can rewrite this state as

$$|n,i_1,\ldots,i_n\rangle =: |n,r^{(1)}+R^{(1)},\ldots,r^{(n)}+R^{(n)}\rangle\ ,$$

using our new notation of a position $i_j =: r^{(j)}+R^{(j)}$ with $r^{(j)} \in \{r_1,\ldots,r_u\}$ and $R^{(j)} := R_{C_1^{(j)},\ldots,C_l^{(j)}}$ with $C_m^{(j)} \in \mathbb{Z}$. Nonetheless, as this notation is not as compact as before, we will stick to our short notation as long as possible. We can define the acting $A(n,i_1,\ldots,i_n) := \mathcal{H}\,|n,i_1,\ldots,i_n\rangle$ of the Hamiltonian $\mathcal{H}$ onto this state. Using the invariance of the Hamiltonian, we get the acting $\tilde{A}$ of states $|n,i_1+d,\ldots,i_n+d\rangle$ translated by a vector $d := R_{C_1,\ldots,C_l}$, by just adding the translation vector to all particles in the original result A, resulting in $\tilde{A} \equiv A(n,i_1+d,\ldots,i_n+d)$.

As our calculation does not depend on the absolute positions of the quasi-particles but their relative positions, we can define the distance in unit cells as $\delta_{ij} := R^{(j)} - R^{(i)}$. Using this relative distance, we can rewrite the state with only one absolute position of 'particle 1' as

$$\begin{aligned} &|n,R^{(1)};\delta_{12},\ldots,\delta_{1n};r^{(1)},\ldots,r^{(n)}\rangle \\ :=\ &|n,r^{(1)}+R^{(1)},r^{(2)}+R^{(1)}+\delta_{12},\ldots,r^{(n)}+R^{(1)}+\delta_{1n}\rangle\ , \end{aligned} \tag{3.1.5}$$

where the first particle is given with absolute position $i_1 = r^{(1)}+R^{(1)}$ and all others with relative distances δ_{ij}.

As long as we are operating on finite clusters (having bounded $0 \le C_k \le C_k^{\max}$ in equation 3.1.1), we have to take care of the boundaries of the lattice. To fulfill the above statement for all positions on the finite cluster we use *periodic boundary conditions* to identify the opposite boundaries with each other to form a l-torus. In our model with $u = l = 2$, we identify the left sites with those on the right and on the top with those on the bottom as sketched in figure 3.2 for a small finite system. The green diamond-formed area is the periodically identified lattice which can be visualized by copying the system along the lattice vectors. Exemplary, one site is marked in yellow. If this yellow site is moved into a certain direction out of the green area, another yellow site moves back in, fulfilling the identification of the boundaries.

A short comment about the used states: The definition of the states as done in section 2.3.2 and in equation 3.1.9 is not uniquely defined for $n \ge 2$. As the quasi-particles are indistinguishable, the states $|2,i_1,i_2\rangle$ and $|2,i_2,i_1\rangle$ are the same. In theory, we can deal with this problem by introducing an *equivalence relation* by permuting all positions as

$$[|n,i_1,\ldots,i_n\rangle] := \{|n,i_{\pi(1)},\ldots,i_{\pi(n)}\rangle \mid \pi \in S_n\}\,, \tag{3.1.6}$$

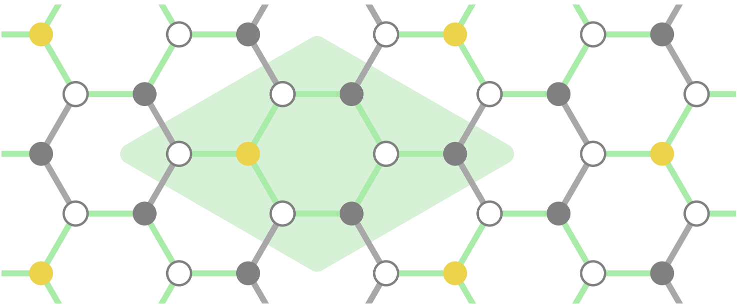

Figure 3.2: Visualization of the periodic boundary conditions for the honeycomb lattice. The 'real' finite lattice from which we start is marked with a green background. By taking the diamond and moving it along the lattice vectors, we can periodically enlarge our original cluster. The original and duplicated clusters are marked with green bonds. The periodic coupling is done with the bonds marked in gray. Every operation on the original cluster is copied on all duplicated clusters. So, when moving a particle (e.g., the one marked in yellow) out of the original cluster, the particle moves back in coming from one of the duplicates. In that way we have periodically identified the boundaries of the diamond with each other.

with S_n being the *symmetric group* of n elements. When implementing these equivalence classes, we choose a unique element of each class, by defining an order of positions in real space. For 1D this would easily be implemented by taking i_1 as the left-most particle and i_n as the right-most one. For our model defined on the 2D honeycomb lattice we define an analogue left-right order as sketched in figure 3.3. We define distances δ_{ij} as *positive distances* if they follow this left-right order.

To use the described translational invariance, we can either transform our Hamiltonian or our states to momentum space via Fourier transformation. We choose to define our n-QP state in k-space as

$$\begin{aligned}&|n,k;\delta_{12},\dots,\delta_{1n};r^{(1)},\dots,r^{(n)}\rangle\\&:=\frac{1}{\sqrt{N}}\sum_{C_1,\dots,C_l}e^{ikR_{\mathrm{CM}}}\,|n,R_{C_1,\dots,C_l};\delta_{12},\dots,\delta_{1n};r^{(1)},\dots,r^{(n)}\rangle\ ,\end{aligned}\tag{3.1.7}$$

where we sum over all unit cells in the lattice by varying $C_1,\dots,C_l$ and with N being the number of lattice sites. The *center of mass* coordinate is defined as $R_{\mathrm{CM}} := R_{C_1,\dots,C_l} + \sum_j^n \delta_{1j}/n$. We define k as the total *momentum* of the quasi-particles, determining the phase between the different unit cells with the exponential. Effectively, the sum in equation 3.1.7 moves the formation of the used n-particle state across the lattice, without changing the relative positions of the single particles. To take care of the periodic boundary conditions, we have to restrict the momentum in order to have the same phase on sites which are identified with each other. When restricting the C_i in equation 3.1.1 to $0 \leq C_i \leq C_i^{\max}$ with a finite positive number $C_i^{\max}$ we obtain the restriction

$$k\cdot C_i^{\max}a_i = n\cdot 2\pi\,,$$

with $n\in\mathbb{Z}$. As this restriction holds for all a_i with $i\in\{1,\dots,l\}$, we use the definition of the dual basis in equation 3.1.4 to decompose the momentum k

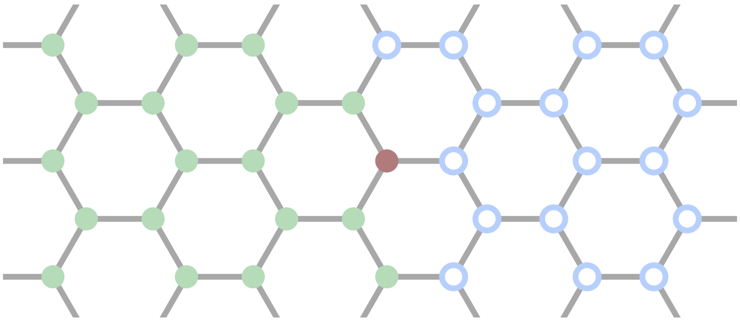

Figure 3.3: Left-right order of the lattice. Considering the red site, all green full sites are labeled as 'left' and all blue contour sites are labeled as 'right'. As the lattice is two-dimensional, the ambiguity of the same x-position is solved by labeling the left/right position depending on the relative y-position. The orientation is used to define a unique multi-particle state as theoretically done in equation 3.1.6.

into the dual basis as

$$k = \sum_{i=1}^{l} \frac{n_i}{C_i^{\max}} b_i \tag{3.1.8}$$

with $n_i \in \mathbb{Z}$. When going to the thermodynamic limes $C_i^{\max} \to \infty$, we go from a discrete definition of k to a continuous variable, as the distances between the allowed momenta become infinitesimal small.

As we will consider up to two quasi-particles and $u = l = 2$, the general momentum state reduces to

$$\begin{aligned} |1,k;r\rangle &= \frac{1}{\sqrt{N}} \sum_{C_1,C_2} e^{ikR_{C_1,C_2}} |1, R_{C_1,C_2}; r\rangle \\ |2,k;\delta;r^{(1)},r^{(2)}\rangle &= \frac{1}{\sqrt{N}} \sum_{C_1,C_2} e^{ik(R_{C_1,C_2}+\delta/2)} |1, R_{C_1,C_2}; \delta; r^{(1)}, r^{(2)}\rangle \ , \end{aligned} \tag{3.1.9}$$

with $r, r^{(1)}, r^{(2)} \in \{a_1, a_2\}$ being defined at the beginning of this section.

As already stated before, we will show that applying the pCUT transformation onto the Hamiltonian in equation 2.1.3 results in a particle conserving effective Hamiltonian H_{eff}. This means that applying H_{eff} onto any state will not change the number of quasi-particles. So, the only possible action is a hopping of an arbitrary number of quasi-particles. We can write H_{eff} generally as

$$H_{\text{eff}} = \sum_{\substack{\delta_1,\ldots,\delta_n \\ r_1,\ldots,r_n \\ \tilde{r}_1,\ldots,\tilde{r}_n}} c_{\delta_1,\ldots,\delta_n}^{r_1,\ldots,r_n \to \tilde{r}_1,\ldots,\tilde{r}_n} \sum_{R_1,\ldots,R_n} \prod_i b^\dagger_{R_i+\delta_i;\tilde{r}_i} \prod_i b_{R_i;r_i} \ , \tag{3.1.10}$$

with $c_{\delta_1,\ldots,\delta_n}^{r_1,\ldots,r_n \to \tilde{r}_1,\ldots,\tilde{r}_n}$ being a constant depending on the specific hopping and $b^{(\dagger)}_{R_i+\delta_i;\tilde{r}_i}$ being the creation or annihilation operator for a quasi-particle at the position $R_i+\delta_i+\tilde{r}_i$. With the two products we annihilate n particles at the given positions and create them back at new positions moved by δ_i along the lattice vectors. Having this abstract formulation of the Hamiltonian and the general

k-space state from equation 3.1.7, we can now derive the simplification from the translational invariance. For doing so we look at general matrix elements in the momentum basis and calculate the result by inserting the definition of the k-states:

$$\begin{aligned}\langle n, \tilde{k}; \tilde{\delta}_{12}, \dots, \tilde{\delta}_{1n}; \tilde{r}^{(1)}, \dots, \tilde{r}^{(n)} \mid H_{\text{eff}} \mid n, k; \delta_{12}, \dots, \delta_{1n}; r^{(1)}, \dots, r^{(n)} \rangle = \\ = \delta_{\tilde{k},k} \sum_{\delta_1,\dots,\delta_n} c_{\delta_1,\dots,\delta_n}^{r^{(1)},\dots,r^{(n)} \to \tilde{r}^{(1)},\dots,\tilde{r}^{(n)}} e^{-ik\delta_{\text{CM}}} \\ \times \langle n, \tilde{k}; \tilde{\delta}_{12}, \dots, \tilde{\delta}_{1n} \mid n, k; \delta_{12} + \delta_2 - \delta_1, \dots, \delta_{1n} + \delta_n - \delta_1 \rangle \ ,\end{aligned} \tag{3.1.11}$$

with $\delta_{\text{CM}} := \sum_i^n \delta_i / n$ being the movement of the center of mass. The braket at the end denotes the distances in unit cells between the individual particles has to be the same between the bra and the ket state. As stated at the beginning of this section, the state is chosen to be unique, e.g., only allowing 'positive' distances.

Overall, what is the benefit of calculating the effective Hamiltonian in k-space as done in equation 3.1.11? In short, we get rid of one degree of freedom for the states. In the definition of an arbitrary state in k-space (equation 3.1.7) we transform one degree of freedom in real space—namely the position of particle 1—into the total momentum of all particles. As the total momentum is conserved by the Hamiltonian due to the term $\delta_{\tilde{k},k}$ in equation 3.1.11, we get rid of this degree of freedom when calculating the Hamiltonian matrix. This results in a block-diagonalization of the Hamiltonian, where each block corresponds to one specific total momentum. So, we can diagonalize the Hamiltonian matrix for each momentum independently, reducing the dimensionality of the single problems, as we can focus on the single 'momentum blocks' in the Hamiltonian. This gets clearer when looking at the one and two quasi-particle case of equation 3.1.11:

$$\langle 1, \tilde{k}; \tilde{r} \mid H_{\text{eff}} \mid 1, k; r \rangle = \delta_{\tilde{k},k} \sum_{\delta} c_{\delta}^{r \to \tilde{r}} e^{-ik\delta_{\text{CM}}} \tag{3.1.12}$$

$$\begin{aligned}\langle 2, \tilde{k}; \tilde{\delta}; \tilde{r}_1, \tilde{r}_2 \mid H_{\text{eff}} \mid 1, k; \delta; r_1, r_2 \rangle = \delta_{\tilde{k},k} \sum_{\delta_1,\delta_2} c_{\delta_1,\delta_2}^{r_1,r_2 \to \tilde{r}_1,\tilde{r}_2} e^{-ik\delta_{\text{CM}}} \\ \times \langle 2, \tilde{k}; \tilde{\delta} \mid 2, k; \delta + \delta_2 - \delta_1 \rangle \ .\end{aligned} \tag{3.1.13}$$

For the 1QP case in equation 3.1.12, we are left with the $\tilde{r}, r$ parameters for fixed momentum. So, the corresponding matrix of the effective Hamiltonian is of size $u \times u$ corresponding to the number of sites in the unit cell. For the honeycomb model we have to diagonalize a 2×2 matrix for obtaining the energy eigenvalues. For 2QP, we have an additional degree of freedom determining the distance between the two particles. As we are aiming to describe an infinite lattice, we have an infinite number of allowed distances, resulting in an infinite dimensional Hilbert-space the effective Hamiltonian is acting on. To still be able to calculate the eigenvalues of this Hamiltonian, we cut our Hilbert-space for high distances as they should play no major role. This can be justified by the *linked cluster theorem* discussed in section 3.2.2 which states that the effective Hamiltonian only acts locally around the quasi-particles in a given state for finite perturbation orders.

Summarizing, we are able to calculate the eigenvalues of the effective Hamiltonian for one quasi-particle in the thermodynamic limit. For 2QP, even as we are not able to calculate the eigenvalues in the thermodynamic limit, we get better approximations as we are able to discard one degree of freedom for fixed momenta.

3.2 Perturbative Continuous Unitary Transformations (pCUTs)

As to this point of the thesis, we have already used the claim that we can transform the Hamiltonian 2.1.2 in such a way that it will be quasi-particle conserving. This helped us in the previous section to define the new effective Hamiltonian 3.1.10 only moving quasi-particles around. The following section will first give an overview of the mathematical derivation of the transformation and an explanation why it is sufficient to focus on finite clusters when using the transformed Hamiltonian. As we are not restricted to the 1QP channel, we will clarify the calculations to get properties of the different quasi-particle channels. We will end the section by introducing the calculation of spectral properties of the model using the same transformation applied onto the Hamiltonian.

3.2.1 Overview of the derivation

The method of perturbative continuous unitary transformations (pCUTs) bases on the method of continuous unitary transformations (CUTs). The idea of CUT is to perform a basis change to simplify the problem to solve. A basis change is accomplished by introducing a unitary transformation U that can—depending on the used 'picture'—be applied on a state $|s\rangle$ with $U|s\rangle$ or on the observables $\mathcal{O}$ with $U^\dagger \mathcal{O} U$. In contrast to the Fourier transformation, which we introduced in the previous section 3.1, we will apply the transformation onto the observable, namely the Hamiltonian.

The main challenge is to find a suitable unitary transformation that really 'simplifies' the problem. As the basis change has to depend on the physical system one is looking at, it is often difficult finding such a transformation our even generalizing the simplification to a class of physical problems.

At this point Wegner's idea comes in to not only applying one but an infinite series of unitary transformations [11]. In the limit of infinitesimal transformations, one gets to a continuous transformation, a so-called CUT. We can introduce a positive real number $l \in \mathbb{R}_0^+$ which labels the 'position' of the CUT. So, an observable $\mathcal{O}$ is transformed to the rotated operator $\mathcal{O}(l)$ as

$$\mathcal{O}(l) = U^\dagger(l) \mathcal{O} U(l)\,, \tag{3.2.1}$$

where we define $\mathcal{O}(0) = \mathcal{O}$ being the original operator and $\mathcal{O}_{\text{eff}} = \lim_{l\to\infty} \mathcal{O}(l)$ the fully transformed effective observable which hopefully will be in a 'simpler' form.

The question remains how to choose the transformation $U(l)$. In the following we will restrict ourselves to the pCUT method which simplifies the Hamiltonian to conserve the number of quasi-particles. For further general information about the CUT method, see the article by Wegner [11] or the detailed introduction by Knetter in his PhD thesis [9].

As motivated, each choice of transformation will only be helpful for a subspace of possible Hamiltonians. So, when applying the pCUT method our Hamiltonian has to match some requirements as listed in the original paper by Knetter and Uhrig [35], generalized to multiple perturbations, as done in [36].

1. The Hamiltonian H can be written into an unperturbed part H_0 and a number of perturbations $V_1, \ldots, V_M$ depending on the perturbation parameters $\lambda_1, \ldots, \lambda_F$, respectively, thus reading $H = H_0 + \sum_{f=1}^{F} \lambda_f V_f$ with $F \in \mathbb{N}$. For the Hamiltonian in equation 2.3.5 we have $F = 3$ with $\lambda_i \equiv J_i$.
2. The unperturbed Hamiltonian H_0 must have an equidistant spectrum which is bounded from below. This was already motivated in section 2.3.2, as the constant distances between the energies corresponds to the addition or subtraction of quasi-particles. We can normalize the Hamiltonian in that way, that we can write the energies of H_0 as $E_i = i$ with $i \in \mathbb{N}_0$. We can express the unperturbed Hamiltonian as

   $$H_0 = \sum_{i \in \mathbb{N}_0} E_i \left|U_i\right\rangle \left\langle U_i\right| ,$$

   where U_i is the eigenspace to the eigenvalue E_i. We denote i as the number of quasi-particles. This implies that the number of quasi-particles is conserved by H_0.
3. The perturbations V_f link the different quasi-particle subspaces U_i, U_j in that way that the difference $\delta = |i - j|$ is bounded from above. So, we can write

   $$V_f = \sum_{n=-N}^{N} T_n^{(f)} ,$$

   where $T_n^{(f)}$ creates or annihilates n quasi-particles for positive or negative n, respectively. In section 2.3.2 we have already written down our Hamiltonian in this form. More formal we can define the action of $T_n \in \{T_n^{(1)}, \ldots, T_n^{(F)}\}$ as commutator between H_0 and T_n with

   $$[H_0, T_n] = nT_n ,$$

   meaning that the ‘number of quasi-particles’—as measured by the unperturbed H_0—changes by n whether T_n is applied before H_0 or afterwards. As we have already seen in equation 2.3.5, for our model we can bound the couplings by $N = 2$.

As outlined above, we now want to apply CUTs onto the Hamiltonian as written in equation 3.2.1. To keep track of $H(l)$ with $l \in \mathbb{R}_0^+$, we define the infinitesimal *generator* $\eta(l)$ as rate of change in the so-called *flow equation*:

$$\frac{\mathrm{d}H(l)}{\mathrm{d}l} = [\eta(l), H(l)] . \tag{3.2.2}$$

We now make an ansatz for $H(l)$ reading

$$\begin{aligned} H(l) &= H_0 + \sum_{\sum_f^F k_f = k}^{\infty} \left[\prod_f^F \lambda_f^{k_f} \right] V(l) \\ &= H_0 + \sum_{\sum_f^F k_f = k}^{\infty} \left[\prod_f^F \lambda_f^{k_f} \right] \sum_{\substack{|\vec{m}|=k \\ \vec{f}}} F(l;\vec{m}) T(\vec{m},\vec{f}) \end{aligned} \tag{3.2.3}$$

where $F(l;\vec{m})$ are real-valued functions we will have to determine by using equation 3.2.2. The $F(l;\vec{m})$ do not depend on $\vec{f}$, specifying which perturbations V_f are used in $T(\vec{m},\vec{f})$. The outer sum starts at $k = 1$ and additionally varies the k_f parameters with the given restriction. The other symbols are defined as

$$\begin{aligned} \vec{m} &= (m_1, \ldots, m_k), \quad \text{with } m_i \in \mathbb{Z} \cap [-N, N] \text{ and } |\vec{m}| := k \\ \vec{f} &= (f_1, \ldots, f_k), \quad \text{with } f_i \in \mathbb{N} \cap [1, F] \text{ and } k_f = |\{f_i \mid f_i = f\}| \\ T(\vec{m},\vec{f}) &= T_{m_1}^{(f_1)} \cdots T_{m_k}^{(f_k)} . \end{aligned} \tag{3.2.4}$$

The ansatz of equation 3.2.3 can be understood as a perturbation series of all λ_f. The individual summands correspond to a series of particle annihilation and creation operators with a coefficient $F(l;\vec{m})$ which depends on the transformation parameter l. When thinking about the optimal outcome of $H(l)$ for $l \to \infty$, we want all coefficients to be zero which correspond to processes changing the total quasi-particle number. We write this goal into the generator η, reading

$$\eta(l) = \sum_{\sum_f^F k_f = k}^{\infty} \left[\prod_f^F \lambda_f^{k_f} \right] \sum_{\substack{|\vec{m}|=k \\ \vec{f}}} \operatorname{sgn}(M(\vec{m})) F(l;\vec{m}) T(\vec{m},\vec{f}) \tag{3.2.5}$$

where we define $M(\vec{m})$ as

$$M(\vec{m}) = \sum_{i=1}^{k} m_i ,$$

denoting the total number of created or annihilated quasi-particles. Plugging M into the signum function corresponds to a vanishing generator if we have achieved our goal, namely only allowing quasi-particle conserving actions.

What is left is determining the functions $F(l;\vec{m})$. For doing so, we plug equations 3.2.3 and 3.2.5 into flow equation 3.2.2 obtaining a set of coupled differential equations. For details on solving these differential equations see [9, 35]. After determining the $F(l;\vec{m})$, we can perform the limit $l \to \infty$ onto our ansatz in equation 3.2.3 to obtain the effective Hamiltonian

$$H_{\text{eff}} = H_0 + \sum_{\sum_f^F k_f = k}^{\infty} \left[\prod_f^F \lambda_f^{k_f} \right] \sum_{\substack{|\vec{m}|=k \\ M(\vec{m})=0 \\ \vec{f}}} C(\vec{m}) T(\vec{m},\vec{f}) , \tag{3.2.6}$$

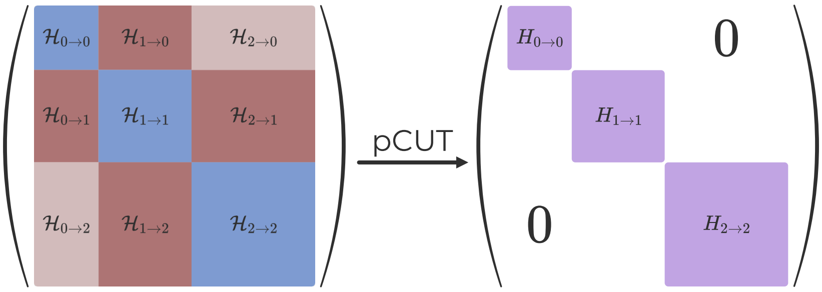

Figure 3.4: Visualization of the block-diagonalization of the pCUT method. On the left is the original Hamiltonian $\mathcal{H} \equiv H(l=0)$, which is structured into the different quasi-particle subspaces as introduced in section 2.3.2. The complete Hamiltonian goes on for higher number of quasi-particles and is only restricted for this visualization to processes for up to two quasi-particles. The term $\mathcal{H}_{i\to j}$ takes a state in the i-QP subspace and transforms the state to a j-QP state. For $\mathcal{H}$, we find couplings between different QP-channels up to a number distance of N, as described in the main text. Using pCUT, we apply continuous transformations resulting in the Hamiltonian $H \equiv H(l=\infty) \equiv H_{\text{eff}}$. This effective Hamiltonian has no couplings left between different QP-channels because $H_{i\to j} = 0$ for $i \neq j$. As the H matrix is now block-diagonal, we can solve the different quasi-particles subspaces independently.

with $C(\vec{m}) := \lim_{l\to\infty} F(l;\vec{m})$. As the summation only considers $M(\vec{m}) = 0$, all processes changing the quasi-particle number have vanished due to the continuous transformation. It should be mentioned that the $C(\vec{m})$ coefficients do not depend on the specific model but only on the above assumptions for our Hamiltonian. So, one can calculate the $C(\vec{m})$ coefficients once and apply them via equation 3.2.6 to the desired model. We can use the form of our Hamiltonian in equation 2.3.5 to directly plug in the different $T(\vec{m})$ processes.

Summing up the section, we have reached a much simpler Hamiltonian by applying a continuous transformation, as we can now independently explore the different quasi-particle sectors. A visualization of the pCUT can be seen in figure 3.4. Starting from an Hamiltonian $H(l=0)$ which connects the different quasi-particle channels with each other due to the perturbation, we end up with an effective Hamiltonian $H(l=\infty)$ of block-diagonal form after the application of pCUT.

3.2.2 Linked Cluster Theorem

After applying the pCUT onto our Hamiltonian, we are left with an Hamiltonian H_{eff} in equation 3.2.6 which is block diagonal with respect to the number of quasi-particles. Nonetheless, the goal of calculating quantities as the energy in the thermodynamic limit remains challenging. Naively, we would still have to do computations on an infinite-dimensional subspace, as the lattice is of infinite size. Apparently, this is either feasible or even possible. To be able to extract the thermodynamic limit we have to make use of a *linked cluster expansion*, meaning calculating the effective Hamiltonian on finite clusters in order to extract the thermodynamic quantities in the end. In the following we will give a short overview over the main arguments of the linked cluster expansions. For more information see the PhDs of Knetter [9] or Cöster [37].

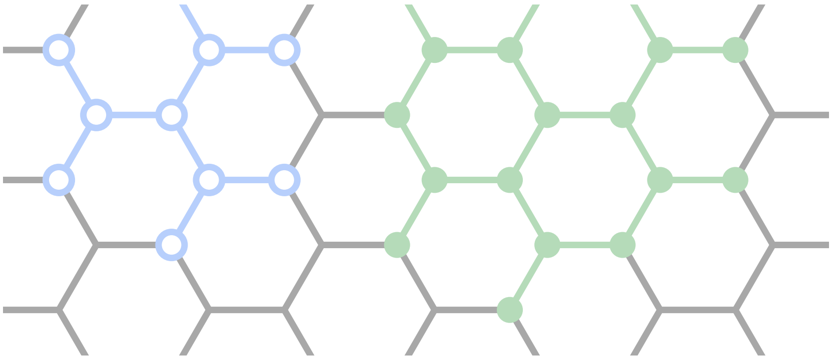

Figure 3.5: An example for graphs in our 2D honeycomb lattice. The two colored graphs are finite subgraphs of the graph G_{lat} of the overall lattice. The graphs are disconnected because they share no sites with each other and there are no direct bonds between the two colorized graphs.

We start with some definitions, following the structure of [9].

Definition 3.1.

1. A *graph* G is a pair of two sets V, L where V is a set of vertices and L is a set of paired vertices in V called links. We write $G \equiv (V, L)$.
2. A graph $G = (V, L)$ is called 'finite graph' or 'cluster' if $\#V < \infty$.
3. We call $\tilde{G} = (\tilde{V}, \tilde{L})$ a *subgraph* if and only if (short iff) $\tilde{G}$ is a graph and $\tilde{V} \subset V, \tilde{L} \subset L$.

We can define the lattice of our model introduced in section 2.1 as a graph G_{lat}, by defining the lattice sites as vertices and the couplings between the sites as links. We will be interested in finite subgraphs which we can use to calculate our physical quantities. Next, we have to subclassify the connections between graphs, by introducing the terms 'linked' and 'disconnected'.

Definition 3.2.

1. Two graphs $A = (V_A, L_A), B = (V_B, L_B)$ are disconnected iff $V_A \cap V_B = \emptyset$ and there is no link in L_A, L_B between elements of V_A and V_B. Otherwise A and B are linked.
2. We call $C = (V_A \cup V_B, L_A \cup L_B) =: A \cup B$ a *linked cluster* if A and B are linked.

An example of these definitions is shown in figure 3.5. The colorized clusters are disconnected because they share no sites and there are no bonds which connect the two clusters. We now have to look at the way operators, namely our Hamiltonian, are working on the different type of graphs.

Definition 3.3.

1. Given an operator $\mathcal{O}$ acting on the full Hilbert space $\mathcal{S}$ of a graph G. We denote $\mathcal{O}^A$ as an operator only acting on a subspace $\mathcal{S}^A$ of a subgraph A of G. It has to stand $\mathcal{O}^A \equiv \mathcal{O}$ for the subspace $\mathcal{S}^A$.
2. Given $C = A \cup B$ with disconnected clusters A, B. We call an operator $\mathcal{O}^C$ *cluster-additive* iff the operator can be decomposed as

   $$\mathcal{O}^C = \mathcal{O}^A \otimes \mathrm{id}^B + \mathrm{id}^A \otimes \mathcal{O}^B$$

   acting independently on the two disconnected clusters.

It is easy to show that the original Hamiltonian $H(l = 0)$ as well as the effective Hamiltonian H_{eff} from equation 3.2.6 are cluster-additive [37, section 2.2.2], as the flow equation acts independently on disconnected clusters. The reason is that H_{eff} only acts locally, meaning the quasi-particle can only move along the bonds which were previously defined as the links of our model-graph G_{lat}. So, we can calculate H^C_{eff} as

$$H^C_{\text{eff}} = H^A_{\text{eff}} \otimes \mathrm{id}^B + \mathrm{id}^A \otimes H^B_{\text{eff}} ,$$

with $C = A \cup B$ and A, B being disconnected clusters. We will see in the following section that we have no cluster-additivity when restricting our Hamiltonian to certain quasi-particle numbers. This will make it a bit more difficult to extract the physical quantities for the QP-channels, independently.

Following the idea called *linked cluster theorem* of Gelfand et al. [38], we can neglect all calculations on disconnected clusters for cluster-additive operators. So, only linked clusters remain to be operated on. This procedure is called *linked cluster expansion*. We can now eventually use this theorem to subdivide our connected clusters into all possible clusters, performing a graph decomposition, as done in [39, 40]. As our model consists of a comparable heavy structure, we will stick to larger connected cluster when calculating physical quantities. The size of the connected cluster is determined by the order up to which we want to calculate the perturbation of the effective Hamiltonian. This is the case as the $T(\vec{m}, \vec{f})$ operators in equation 3.2.6 can act on sites whose distance is proportional to the perturbation order. As stated in equation 3.2.4, the number of T_{m_o} operations depends on order k and the single T_{m_o} can be decomposed into local interaction terms $t^{\alpha}_{m_o}(i, j)$ between neighbored sites i, j, as shown in equation 2.3.5. For more information about the actual construction of the needed clusters to calculate quantities in the thermodynamic limit for one and two quasi-particles, see appendix A.

3.2.3 Extracting single QP-channels

Naively one could think we now have all tools at hand to calculate our wanted physical quantities. As an example, we could calculate the braket of a 2QP state as $\langle 2, \tilde{i}, \tilde{j} \mid H_{\text{eff}} \mid 2, i, j\rangle$ expecting to calculate the hopping amplitude for the two quasi-particle sector in the thermodynamic limit. This is not the case in general (for this example we move into problems for $\tilde{i} = i$ and $\tilde{j} = j$) as for some hoppings we have to take lower particle channels into consideration. To see the problem more clearly, we write the effective Hamiltonian as

$$H_{\text{eff}} =: \sum_{n=0}^{\infty} H_n \,, \tag{3.2.7}$$

where the H_n operators are defined as normal ordered n-QP hoppings which can be expressed by

$$H_n = \sum_{\substack{\tilde{j}_1,\dots,\tilde{j}_n \\ j_1,\dots,j_n}} c_{j_1,\dots,j_n \to \tilde{j}_1,\dots,\tilde{j}_n} b^{\dagger}_{\tilde{j}_1} \cdots b^{\dagger}_{\tilde{j}_n} b_{j_1} \cdots b_{j_n} \,. \tag{3.2.8}$$

The summation goes over all possible lattice sites on the lattice and is similarly defined as the hopping Hamiltonian 3.1.10. This notation makes more clear that for extracting the actual impact of the n-QP subspace, we have to determine $\langle n, \tilde{j}_1, \dots, \tilde{j}_n \mid H_n \mid n, j_1, \dots, j_n \rangle$ or more concrete $H_n|_n$ where H_n is restricted to the n-QP subspace. By using $H_n|_m \equiv 0$ for $m < n$ we can iteratively calculate the $H_n|_n$ terms with

$$H_n|_n = H_{\text{eff}}|_n - \sum_{m=0}^{n-1} H_m|_n \,. \tag{3.2.9}$$

We can calculate $H_n|_n$ repetitively by starting with $H_0|_0 = H_{\text{eff}}|_0$. Then we use this result to obtain $H_1|_1 = H_{\text{eff}}|_1 - H_0|_1$. Following this scheme, we can calculate $H_n|_n$ up to arbitrary n. It is important to stress that the restricted effective Hamiltonian $H_{\text{eff}}|_n$ is not cluster additive, as can be shown [9, page 11]. This means on the computational side that we have to do the calculation of the terms on the right side of equation 3.2.9 on the same cluster. To make this more clear, we use the notation $\mathcal{O}^A$ when calculating a certain quantity $\mathcal{O}$ on a cluster A, as introduced before.

In the following we want to demonstrate the calculation of the coefficients $c_{j_1,\dots,j_n \to \tilde{j}_1,\dots,\tilde{j}_n}$ in equation 3.2.8 using the scheme of equation 3.2.9. We denote

$$\begin{aligned} E_0^A &:= \langle 0 \mid H_{\text{eff}}^A \mid 0 \rangle \\ a_{i \to j}^A &:= \langle 1, j \mid H_{\text{eff}}^A \mid 1, i \rangle \\ a^A_{j_1,\dots,j_n \to \tilde{j}_1,\dots,\tilde{j}_n} &:= \langle n, \tilde{j}_1, \dots, \tilde{j}_n \mid H_{\text{eff}}^A \mid n, j_1, \dots, j_n \rangle \,, \end{aligned} \tag{3.2.10}$$

with A being a finite and ‘large enough’ cluster, as described in more detail in appendix A. Using equation 3.2.9, we can calculate the coefficients in the thermodynamic limit as

$$\begin{aligned} c_{i \to j} &= a^A_{i \to j} - E_0^A \delta_{ij} \\ c_{j_1,\dots,j_n \to \tilde{j}_1,\dots,\tilde{j}_n} &= a^A_{j_1,\dots,j_n \to \tilde{j}_1,\dots,\tilde{j}_n} - \sum_{m=0}^{n-1} \sum_{\sigma,\tilde{\sigma} \in S_n} c^A_{j_{\sigma(1)},\dots,j_{\sigma(m)} \to \tilde{j}_{\tilde{\sigma}(1)},\dots,\tilde{j}_{\tilde{\sigma}(m)}} \\ &\quad \times \delta_{j_{\sigma(m+1)},\tilde{j}_{\tilde{\sigma}(m+1)}} \cdots \delta_{j_{\sigma(n)},\tilde{j}_{\tilde{\sigma}(n)}} \,. \end{aligned} \tag{3.2.11}$$

In words, the calculation is done by subtracting all processes from the calculated matrix element $a^A_{j_1,\dots,j_n \to \tilde{j}_1,\dots,\tilde{j}_n}$ which do not move all n particles. The outer sum of the last equation over m corresponds to the sum in equation 3.2.9. We again stress the fact, that the variables on the right side of the equations have to be calculated on the same cluster A. The cluster additivity assures that the computations done on these finite clusters result in coefficients in the thermodynamic limit, as indicated by the lack of an additional cluster superscript for the c coefficients.

With the calculations in equation 3.2.11 we are able to rewrite the Hamiltonian H_{eff} in terms of H_n in equation 3.2.7. In the following we want to outline how we can calculate the energy of single QP-channels, following Knetter's paper for the two-leg Heisenberg ladder [41].

We start with the ground state, in terms of second quantization denoted as the 0QP subspace. We have shown the equivalence of the two definitions in section 2.3.2 for small enough perturbations. As we are not calculating the energy of a single quasi-particle but the energy of the 'quasi-particle vacuum', we define the ground-state energy as an energy per site, reading

$$\epsilon_0 = \frac{\langle 0 \mid H_0^A \mid 0 \rangle}{N} = \frac{\langle 0 \mid H_{\text{eff}}^A \mid 0 \rangle}{N} = \frac{E_0^A}{N} \,,$$

with N being the number of sites in the cluster A. The energy per site is independent of the cluster A if it is chosen large enough as described at the end of section 3.2.2.

Next, we want to calculate the 1QP dispersion. In other words, we want to obtain the energy of one quasi-particle, meaning the energy change between the 0QP and 1QP subspaces. Using the decomposition of H_{eff} into normal ordered hoppings in equation 3.2.7, this quantity lies inside of H_1. This is the case as H_1 is the part which describes the pure one quasi-particle behavior. We use equation 3.2.11 to obtain the H_1 hopping coefficients as

$$c_{i\to j} = \langle 1, j \mid H_1 \mid 1, i \rangle = a^A_{i\to j} - E_0^A \delta_{ij} \,. \tag{3.2.12}$$

So, we have determined an Hamiltonian H_1 that is of the form of equation 3.1.10, which was used for the Fourier transformation in section 3.1. Now, we can use the momentum space representation of our 1QP states and reduce the problem to a 2×2 matrix. By diagonalizing this matrix, we obtain the 1QP dispersion (meaning the 1QP energy with respect to the momentum k) containing two bands. The results and discussion of them can be found in section 4.1.

Lastly, we want to investigate the 2QP dispersion calculation. To catch possible ambiguities, we define the 2QP dispersion as the energy of the two particle states with respect to the ground state. This means we not only have to look at H_2 but also H_1, as H_2 only includes the processes of two-particle interaction, while H_1 describes the behavior of two independent quasi-particles. We will dive deeper into this difference, when introducing the free particle approximation in section 3.3. So, to describe the 2QP dispersion, we have to investigate $H_{\text{eff}} - H_0 = H_1 + H_2$, subtracting only the energy of the vacuum. We can calculate the hoppings of the two H_i independently.

Starting with H_1, we can utilize the form of the operator as it only moves one of the two quasi-particles at maximum. This means for a general two quasi-particle state $|2,i,j\rangle$ we can write the action of H_1 as

$$\begin{aligned} H_1 \left|2,i,j\right\rangle &= \sum_{\substack{\tilde{j}_1 \\ j_1}} c_{j_1\to\tilde{j}_1} b^{\dagger}_{\tilde{j}_1} b_{j_1} \left|2,i,j\right\rangle \\ &= \sum_{\tilde{j}_1} c_{i\to\tilde{j}_1} \left|2,\tilde{j}_1,j\right\rangle + \sum_{\tilde{j}_1} c_{j\to\tilde{j}_1} \left|2,i,\tilde{j}_1\right\rangle \ , \end{aligned}$$

splitting the action of H_1 into two parts, moving only one of the two quasi-particles i, j. We see that we only have to use the $c_{i\to j}$ coefficients which we already have calculated for the 1QP dispersion in equation 3.2.12.

For the two-quasi-particle interaction terms in H_2, we have to calculate their coefficients first. We use the ansatz of equation 3.2.11 to calculate those as

$$\begin{aligned} c_{j_1,j_2\to\tilde{j}_1,\tilde{j}_2} &= \langle 2,\tilde{j}_1,\tilde{j}_2 \mid H_2 \mid 2,j_1,j_2\rangle = \langle 2,\tilde{j}_1,\tilde{j}_2 \mid H_{\text{eff}} - H_0 - H_1 \mid 2,j_1,j_2\rangle \\ &= a^A_{j_1,j_2\to\tilde{j}_1,\tilde{j}_2} - E^A_0 \delta_{j_1,\tilde{j}_1}\delta_{j_2,\tilde{j}_2} - a^A_{j_1\to\tilde{j}_1}\delta_{j_2,\tilde{j}_2} \\ &\quad - a^A_{j_2\to\tilde{j}_1}\delta_{j_1,\tilde{j}_2} - a^A_{j_1\to\tilde{j}_2}\delta_{j_2,\tilde{j}_1} - a^A_{j_2\to\tilde{j}_2}\delta_{j_1,\tilde{j}_1} \ . \end{aligned} \tag{3.2.13}$$

Again, we have to calculate all these processes on the same cluster A. So, in general we are not able to reuse the coefficients of H_0 and H_1 in the thermodynamic limit.

Moving to the states in momentum space $|2,k;\delta;r_1,r_2\rangle$, as defined in equation 3.1.7, we can combine the H_1, H_2 operators to an $H_{1+2} := H_1 + H_2$ operator which again matches the form of equation 3.1.10. As stated in section 3.1, we can decouple the different total momenta k from each other to reduce the dimensionality of the subspace of fixed k to the possible distances δ between the quasi-particles and the possible positions r_i in the primitive cell. So, we have matrix elements of the form

$$\langle 2,k;\tilde{\delta};\tilde{r}_1,\tilde{r}_2 \mid H_1 + H_2 \mid 2,k;\delta;r_1,r_2\rangle \ .$$

As distances can get arbitrary high, we restrict ourselves to a finite maximum distance δ_{max} to obtain a matrix of finite size. As the action of H_1 only moves one of the quasi-particles, the position of the other one is arbitrary (up to the same starting and ending position). We can use this independency to calculate the action of H_1 for all distances δ. For H_2, we are limited in distance because the processes involve both quasi-particles. We can schematically draw this resulting matrix, as done in figure 3.6. The basis in which the matrix is visualized starts with small distances and grows when going further down. So, the action of H_2 only takes place for small distances. For H_1 the situation corresponds to a 'band' on the diagonal. The 'bandwidth' is determined by the range of the 1QP hoppings, calculated in equation 3.2.12. By diagonalizing this matrix (which we further on denote as H_{dist}), we obtain the possible energies of the two quasi-particle excitations. Keep in mind that we are not in the thermodynamic limit anymore, as we have introduced δ_{max}. For $\delta_{\text{max}} \to \infty$, we expect to obtain a continuum of possible energies within certain boundaries. We will see in the discussion section 4.2 that these edges of the continuum are well approximated by our calculations with only finite distances. Again the free particle approximation in section 3.3 will shed some light into this continuum.

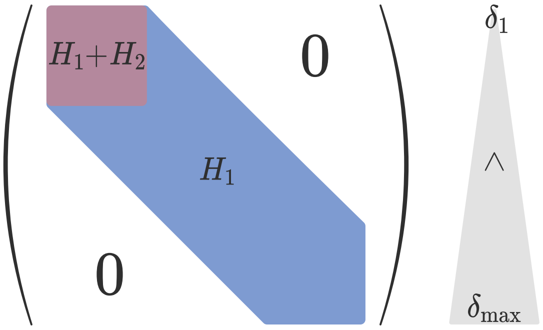

Figure 3.6: Visualization of the 'distance matrix' H_{dist} for the calculation of the 2QP dispersion. As outlined in the main text, we have to evaluate $H_1 + H_2$ on the two particle states. As shown in section 3.1, we can denote the two quasi-particle states with a distance δ between them. So, we have to solve a Hamiltonian matrix coupling states with different distances as sketched. The basis is chosen that the states with smaller distance are on the top and the distances get larger when moving downwards. The distances are cut for a maximum distance δ_{max}. The H_1 couples states with similar distance, independent of the absolute distance. The H_2 operator only couples states with small distances between the two quasi-particles. For more details regarding the form of the matrix, see the main text.

3.2.4 Spectral quantities

Up to this point we have concentrated on calculating the eigenvalues of the Hamilton-operator, namely the quasi-particle energies and the ground-state energy. Nonetheless, we also want to be able to perform calculations on other relevant observables O. As an example, we will be investigating the expectation value and other *spectral quantities* of the observable σ^z later on in section 4.1.2 and 4.2.3. To calculate observables in the same basis, we have to be able to apply the pCUT method on general observables O and not only on the Hamiltonian.

In the following section we will sketch the steps needed to apply the pCUT onto O and calculate spectral quantities with it. For a more detailed treatment see again [9]. The basic steps will be the same as done for the Hamilton-operator following the three last sections. It is important to have in mind that we will not apply a new transformation onto our observable, as we have already defined the transformation to maintain the number of quasi-particles when acting on the Hamilton-operator. So, in general the transformed operators will not be quasi-particle conserving, in contrast to the effective Hamiltonian H_{eff}.

Starting with an observable O, we first have to apply the rotation U as done in equation 2.1.3 to match with the basis where the magnetic field was rotated to be aligned along the z-axis. We denote the rotated observable

$$\mathcal{O} := U^\dagger O U\,,$$

as done for the Hamiltonian. Next, we will apply the unitary pCUT onto $\mathcal{O}$. For doing so we define the flow equation

$$\frac{\mathrm{d}\mathcal{O}(l)}{\mathrm{d}l} = [\eta(l), \mathcal{O}(l)]$$

for $\mathcal{O}(l)$ as done for the Hamiltonian using the same generator $\eta(l)$ from equation

3.2.5. In analogy to the ansatz for $H(l)$ in equation 3.2.3, we use the ansatz

$$\mathcal{O}(l) = \sum_{\sum_f^F k_f = k}^{\infty} \left[\prod_f^F \lambda_f^{k_f}\right] \sum_{i=1}^{k+1} \sum_{\substack{|\vec{m}|=k \\ \vec{f}}} G(l;\vec{m};i)\mathcal{O}(\vec{m},\vec{f};i)\,,$$

where $G(l;\vec{m};i)$ are the real-valued functions we have to determine, as we did for $F(l;\vec{m})$ in the Hamiltonian ansatz. In contrast to the latter, the outer sum starts at $k = 0$ and we have added another sum over i, that specifies the position of $\mathcal{O}$ in the product of operators $\mathcal{O}(\vec{m},\vec{f};i)$ which reads

$$\mathcal{O}(\vec{m},\vec{f};i) := T_{m_1}^{(f_1)} \cdots T_{m_{i-1}}^{(f_{i-1})} \mathcal{O} T_{m_i}^{(f_i)} \cdots T_{m_k}^{(f_k)} \tag{3.2.14}$$

analog to equation 3.2.4. As before, we obtain a set of differential equations for $G(l;\vec{m};i)$ when inserting our ansatz into the flow equation. In the limit of $l \to \infty$ we obtain our effective observable $\mathcal{O}_{\text{eff}}$ as

$$\mathcal{O}_{\text{eff}} = \sum_{\sum_f^F k_f = k}^{\infty} \left[\prod_f^F \lambda_f^{k_f}\right] \sum_{i=1}^{k+1} \sum_{\substack{|\vec{m}|=k \\ \vec{f}}} \tilde{C}(\vec{m};i)\mathcal{O}(\vec{m},\vec{f};i)\,, \tag{3.2.15}$$

with $\tilde{C}(\vec{m};i) := \lim_{l\to\infty} G(l;\vec{m};i)$. As for the coefficients of the effective Hamiltonian, the $\tilde{C}(\vec{m};i)$ do not depend on the model or the specific observable. As already mentioned above, the main difference to equation 3.2.6 is the lack of the condition $M(\vec{m}) = 0$. This means that $\mathcal{O}_{\text{eff}}$ is not particle-conserving in general.

When calculating physical quantities for different quasi-particle channels, it is again helpful to rewrite the effective observable as done for the effective Hamiltonian. As we have to take care of changing quasi-particle numbers the expression has to be more general. We can define

$$\begin{aligned} \mathcal{O}_{\text{eff}} &:= \sum_{n=0}^{\infty} \sum_{d=-n}^{\infty} \mathcal{O}_{d,n} \\ \text{with } \mathcal{O}_{d,n} &:= \sum_{\substack{\tilde{j}_1,\dots,\tilde{j}_{n+d} \\ j_1,\dots,j_n}} w_{j_1,\dots,j_n \to \tilde{j}_1,\dots\tilde{j}_{n+d}} b^\dagger_{\tilde{j}_1} \cdots b^\dagger_{\tilde{j}_{n+d}} b_{j_1} \cdots b_{j_n}\,. \end{aligned}$$

Variable d indicates the change of the particle number in the corresponding process, with d created or annihilated quasi-particles. Variable n serves for the same purpose as in equation 3.2.8, namely $\mathcal{O}_{d,n}|_m = 0$ for $m < n$ to denote the minimal number of quasi-particles in a state before the corresponding process does not vanish identically.

In the following, we want to restrict our physical quantities, which we will investigate, to dynamical correlations at *zero temperature* $T = 0$. This means that we apply the observables only on the ground state $|0\rangle$, as there are no thermal excitations [42]. As a result, we can restrict ourselves to $\mathcal{O}_{d,n=0}$ as all other processes with $n > 0$ vanish. We denote the zero-temperature effective observable as

$$\mathcal{O}_{\text{eff}}^{T=0} = \sum_{d=0}^{\infty} \mathcal{O}_{d,0}\,.$$

The computation of the coefficients $w_{0\to\tilde{j}_1,\dots\tilde{j}_d}$ can be done straightforward. By applying $\mathcal{O}_{\text{eff}}^{T=0}$ onto the ground state we obtain

$$\mathcal{O}_{\text{eff}}^{T=0}\left|0\right\rangle=\sum_{d=0}^{\infty}\mathcal{O}_{d,0}\left|0\right\rangle=\sum_{d=0}^{\infty}\sum_{\tilde{j}_1,\dots,\tilde{j}_d}w_{0\to\tilde{j}_1,\dots\tilde{j}_d}\left|d,\tilde{j}_1,\dots,\tilde{j}_d\right\rangle\ . \tag{3.2.16}$$

We can extract a single coefficient $w_{0\to\tilde{j}_1,\dots\tilde{j}_d}$ by multiplying a bra $\left\langle d,\tilde{j}_1,\dots,\tilde{j}_d\right|$ from the left. This is in contrast to the scheme for the effective Hamiltonian in equation 3.2.11, where we had to apply subtractions for the lower quasi-particle sectors. If we would introduce an operator on $T>0$, having excited states as ket states, we would have to apply analogous subtractions as done in [9, section 2.3.2].

As for the calculation of the Hamiltonian processes, we can perform the calculations for the thermodynamic limit on finite clusters. The main argument we have to make is restricting the observable $\mathcal{O}$ to be local. In our case we go even further and confine the operation of $\mathcal{O}$ on a single site p in the lattice, denoted as $\mathcal{O}(p)$. As we can argue that the rest of $\mathcal{O}_{\text{eff}}$ also stays local as we applied the same pCUT as for H_{eff}, we can confine the finite cluster to connect site p and the sites where quasi-particles were generated by $\mathcal{O}_{\text{eff}}$ and expand it to be 'large enough' to consider the possible linked virtual processes to an particular order. For more details see again appendix A.

We can further on define the *global observable* in momentum space representation as

$$\mathcal{O}_{\text{eff}}^{T=0}(k)\left|0\right\rangle=\frac{1}{\sqrt{N}}\sum_{r}e^{ikr}\mathcal{O}_{\text{eff}}^{T=0}(r)\left|0\right\rangle\ , \tag{3.2.17}$$

analog to the definition of the momentum state in equation 3.1.7, where N denotes the number of sites and the sum goes over all sites of the lattice. The notation $\mathcal{O}_{\text{eff}}^{T=0}(r)$ specifies the site r on which the observable acts. Note that in contrast to the momentum states the phase does not only depend on the position of the primitive cell but also on the place of the site in the primitive cell, as we can split the position r into the position of the primitive cell and the position of the site within. In contrast to the momentum states, the new global observable depends only on the momentum k and not on the place in the primitive cell r, as $\mathcal{O}_{\text{eff}}^{T=0}(k)\left|0\right\rangle$ acts on all sites of the lattice.

Having the effective observable $\mathcal{O}_{\text{eff}}^{T=0}$, we now can calculate spectral quantities of the original observable O [12, 41]. The first most general quantity is the *spectral weight* I_{tot} of the observable, given as

$$I_{\text{tot}}=\left\langle 0\mid\mathcal{O}^2\mid 0\right\rangle-\left\langle 0\mid\mathcal{O}\mid 0\right\rangle^2\ ,$$

where we used the initial observable [41, page 535]. We can now start to subclassify this quantity with respect to several variables. First, we divide I_{tot} into the different particle channels. To get the weight of the n quasi-particle channel, we can define

$$I_n=\left\langle 0\mid\mathcal{O}_{n,0}^{\dagger}\mathcal{O}_{n,0}\mid 0\right\rangle=\sum_{i_1,\dots,i_n}\left|\left\langle n,i_1,\dots,i_n\mid\mathcal{O}_{n,0}\mid 0\right\rangle\right|^2 . \tag{3.2.18}$$

By using the hermitian property of the observable, as done in the last equation, we can calculate I_n, by using the coefficients $w_{0\to i_1,\dots,i_n}$ obtained by equation 3.2.16. We define the relative weight I_n/I_{tot}, as the total spectral weight is given as

$$I_{\text{tot}} = \sum_{d=0}^{\infty} I_d \,. \tag{3.2.19}$$

So, when calculating the weights of the first QP channels, we obtain the 'missing weight' of the higher QP channels, by subtracting the sum of all calculated I_n from the total weight I_{tot}. We can further subdivide the weight into the spectral density of the given observable. These quantities give us insights into the dynamical correlations of this system. These correlations can be investigated on the experimental site with experiments like inelastic neutron scattering. Thus, the calculation of spectral densities let us establish a connection between theory and experiments, to check if the two match [12].

We can define the momentum k and energy ω resolved *dynamical structure factor* $S(k,\omega)$ for the observable $\mathcal{O}$ as

$$S(k,\omega) = -\frac{1}{\pi}\text{Im}\,\langle\psi_0 \mid \mathcal{O}^\dagger \frac{1}{\omega - [\mathcal{H} - E_0] + i0^+}\mathcal{O} \mid \psi_0\rangle \ , \tag{3.2.20}$$

where the braket is the retarded zero temperature Green's function, E_0 is the ground-state energy, and ψ_0 is the ground state of the Hamiltonian $\mathcal{H}$ given in equation 2.1.3. More general, we can denote $S(k,\omega)$ as a specific *spectral density*, depending on k,ω and the respective observable. Note that $\mathcal{O},\mathcal{H}$ depend on k, too [12, section 4.1]. Investigating this expression from right to left, we first act with the observable which creates quasi-particles with the given momentum k. These states are weighted with the denominator depending on the Hamilton-operator. Lastly, we apply $\mathcal{O}^\dagger$ before projecting back to the ground state. As done with the spectral weight, we can subdivide the spectral density into the different quasi-particle channels S_d. For doing so, we transform equation 3.2.20 into our effective basis, by adding the identity id $\equiv U^\dagger U$, where U is the unitary transformation done by pCUT. We obtain

$$S(k,\omega) =: \sum_{d=0} S_d(k,\omega) = \sum_{d=0}^{\infty} -\frac{1}{\pi}\text{Im}\,\langle 0 \mid \mathcal{O}^\dagger_{d,0}\frac{1}{\omega - [H_{\text{eff}} - E_0] + i0^+}\mathcal{O}_{d,0} \mid 0\rangle \ , \tag{3.2.21}$$

where $|0\rangle = U\,|\Psi_0\rangle$ is the transformed ground state, which is in our case the quasi-particle vacuum (0QP state). We can examine the single quasi-particle channels by calculating the S_d separately. For $d = 1$, we use *Dirac's identity*

$$\frac{1}{x - x_0 \pm i0^+} = \mathcal{P}\frac{1}{x - x_0} \mp i\pi\delta(x - x_0)\,,$$

where $\mathcal{P}$ is Chauchy's principle value (which we can ignore as we are only interested in the imaginary part) to simplify the previous expression to

$$S_1(k,\omega) = \langle 0 \mid \mathcal{O}^\dagger_{1,0}\delta(\omega - H_1)\mathcal{O}_{1,0} \mid 0\rangle \ . \tag{3.2.22}$$

We see that S_1 is non-zero when ω is chosen as one of the eigenenergies of H_1. So, we can calculate S_1 by expressing $\mathcal{O}_{1,0}\left|0\right\rangle$ in terms of the eigenbasis of H_1. For the eigenvalues $\omega_1, \ldots, \omega_p$ of H_1, we obtain the density as the squared of the coefficient of $\mathcal{O}_{1,0}\left|0\right\rangle$ for the eigenstate of the respective eigenvalue. Note that we have to transform our effective observable in equation 3.2.16 into the momentum basis as done in equation 3.2.17, as the spectral density is defined in momentum space.

If we are only interested in the momentum dependency of the spectral density, we can formally apply an integral to equation 3.2.21 over all energies ω, resulting in the momentum resolved

$$S(k) := \int \mathrm{d}\omega \, S(k,\omega) \,, \tag{3.2.23}$$

which is called *static structure factor*. This simplifies the calculations, as we do not have to compute the basis of H_1. Equation 3.2.22 shortens to

$$S_1(k) = \left\langle 0 \mid \mathcal{O}_{1,0}^{\dagger} \mathcal{O}_{1,0} \mid 0 \right\rangle \,.$$

Again, we have to use the global definition of the observables but can stay in the original momentum basis. For higher quasi-particle subspaces we can calculate the spectral densities analog to the presented equations but have to deal with more complicated Green functions. For more information about the higher QP channels and spectral densities in general, see [12, chapter 4].

In this section we have enlarged our field of applications for pCUT by applying it to local acting observables. In contrast to before, the quasi-particle number is not conserved as for H_{eff}. As final result, we have an effective observable $\mathcal{O}_{\text{eff}}^{T=0}$ in equation 3.2.16 which creates quasi-particles around the action of the original observable $\mathcal{O}$, as guaranteed by the linked cluster theorem. In principle we can investigate the creation of arbitrary many quasi-particles, as indicated by d going up to infinity in equation 3.2.16. Nonetheless, it often suffices to concentrate on low quasi-particle numbers, as long as the perturbation is ‘sufficiently small’ [42, figure 2], as also can be seen in the discussion, e.g., in figure 4.12. As for the dispersion, we will restrict ourselves in this work to processes with up to two quasi-particles.

3.3 Free particle approximation

As seen in the previous section, the complexity of calculating the quasi-particle energies or spectral quantities increases drastically when investigating higher quasi-particle numbers. For the dispersion this step is especially drastic, as we can calculate the 1QP dispersion in the thermodynamic limit (to a given perturbation order) but the 2QP one only in the limit of finite distances between the quasi-particles, as shown in section 3.2.3. In the following section we introduce the so-called *free particle approximation* as a tool to approximate the 2QP dispersion or even higher QP number dispersions by the already calculated 1QP energies. An introduction to the topic is also given by Feynman in his lecture series [43, chapter 15]. In this section we will first give a physical intuition for this approximation, followed by some calculations to justify what we did before.

The physical idea behind the approximation is quite intuitive. When introducing the quasi-particle language in section 2.3.2, we motivated that we can treat the excitations of the polarized phase as particles which are not 'physical particles' but 'quasi-particles'. Coming back to the simplest problems in quantum physics or even classical mechanics, we can easily describe several non-interacting particles by treating them separately. So for this approach, we will neglect all interactions between the single quasi-particles to get an approximation of the behavior of several particles without having to treat them explicitly. Using our decomposition of H_{eff} in equation 3.2.7, we can drop the interactions by defining

$$H_{\text{eff}}^{\text{FPA}} := H_0 + H_1 \tag{3.3.1}$$

as our approximate Hamiltonian.

We start with the definition of one quasi-particle $|1, k; r\rangle$—as defined in equation 3.1.7—with a momentum k. We know from section 3.1 that we have to diagonalize a 2×2 matrix—coming from the degree of freedom in the primitive cell—to obtain the eigenenergies $\epsilon_1(k), \epsilon_2(k)$ and the corresponding eigenstates $|\epsilon_1(k)\rangle, |\epsilon_2(k)\rangle$, reading

$$H_{\text{eff}} |\epsilon_i(k)\rangle = H_{\text{eff}}^{\text{FPA}} |\epsilon_i(k)\rangle = \epsilon_i(k) |\epsilon_i(k)\rangle \ .$$

Assuming a state holds two non-interacting quasi-particles with the 1QP states $|\epsilon_{i_1}(k_1)\rangle, |\epsilon_{i_2}(k_2)\rangle$, where the new index labels the corresponding quasi-particle. As we dropped all interactions between the two particles in $H_{\text{eff}}^{\text{FPA}}$, we define the 2QP state $|\epsilon_{i_1}(k_1)\rangle \otimes |\epsilon_{i_2}(k_2)\rangle$ with

$$H_{\text{eff}}^{\text{FPA}} \left(|\epsilon_{i_1}(k_1)\rangle \otimes |\epsilon_{i_2}(k_2)\rangle\right) = \left(\epsilon_{i_1}(k_1) + \epsilon_{i_2}(k_2)\right) \left(|\epsilon_{i_1}(k_1)\rangle \otimes |\epsilon_{i_2}(k_2)\rangle\right) ,$$

to match with our physical idea that the total energy ϵ_{tot} of the 2QP state should just be the sum of the two 1QP energies. Moreover, we define the 2QP state to have a total momentum $k_{\text{tot}} = k_1 + k_2$, as we expect for two independent particles in general. Being interested at a 2QP state with a specific total momentum, we can find a bunch of different options for k_1, k_2, as we have one degree of freedom. The possible 2QP energies for fixed k_{tot} can be written as

$$\epsilon_{\text{tot}}(k_{\text{tot}}) \in \left\{\epsilon_{i_1}(k_1) + \epsilon_{i_2}(k_2) \mid k_1 + k_2 = k_{\text{tot}},\ i_1, i_2 \in \{1, 2\}\right\} , \tag{3.3.2}$$

forming a continuum of 2QP states. To be precise, we have several continua as the momenta k_1, k_2 are continuous in the thermodynamic limit, but the i_1, i_2 are discrete. We can search for the maximum and minimum of these set to find the edges of the continua [40]. In the discussion chapter, we will use these edges to compare them to the explicit calculations done in the 2QP subspace.

As neat as the physical idea is for this approximation, we still have to find a formal connection between the one and two quasi-particle states. As for now, we have just written down the 2QP state in a sketchy way to give some physical intuition. For the rest of this section, we shall look at the free particle approximation from a mathematical more accurate perspective.

First, we take a look at the creation of general n-QP states. As introduced in section 2.3.2, we denote such a state as $|n, i_1, \ldots, i_n\rangle$ with $i_1, \ldots, i_n$ being the positions of the quasi-particles on the lattice. Starting from the ground state $|0\rangle$ we obtain such a state by applying creation operators introduced by the Matsubara-Matsuda transformation as

$$|n, i_1, \dots, i_n\rangle = b^\dagger_{i_1} \cdots b^\dagger_{i_n} |0\rangle \ . \tag{3.3.3}$$

Therefore, we can change the QP-sector of a state by adding creation or annihilation operators to it. In order to establish a connection between the different QP-sectors in momentum space, we define creation and annihilation operators $a^{(\dagger)}_{k,1}, a^{(\dagger)}_{k,2}$ for the eigenstates $|\epsilon_1(k)\rangle, |\epsilon_2(k)\rangle$ of $H^{\text{FPA}}_{\text{eff}}$. For doing so we can express $|\epsilon_1(k)\rangle, |\epsilon_2(k)\rangle$ in the real space basis as

$$|\epsilon_i(k)\rangle = \frac{1}{\sqrt{N}} \sum_{C_1,C_2} e^{ikR_{C_1,C_2}} (c_{k,i,1} |1, R_{C_1,C_2}; r_1\rangle + c_{k,i,2} |1, R_{C_1,C_2}; r_2\rangle) \, , \tag{3.3.4}$$

with $i \in \{1, 2\}$, using the definition of the momentum states in equation 3.1.7 and a general solution of the diagonalization process with $c_{k,i,1}, c_{k,i,2}$ being the obtained constants. As introduced in section 3.1, R_{C_1,C_2} determines the specific primitive cell and r_1, r_2 the positions of the sites within the primitive cell. Using equation 3.3.4, we can define the creation and annihilation operators for such particles, reading

$$a^\dagger_{k,i} := \frac{1}{\sqrt{N}} \sum_{C_1,C_2} e^{ikR_{C_1,C_2}} (c_{k,i,1} b^\dagger_{R_{C_1,C_2};r_1} + c_{k,i,2} b^\dagger_{R_{C_1,C_2};r_2}) \, , \tag{3.3.5}$$

with $b^\dagger_r := b^\dagger_{R_{C_1,C_2};r_\gamma}, \gamma \in \{1, 2\}$ being the creation operator for the respective position $r = R_{C_1,C_2} + r_\gamma$ in real space. Using the commutation relation $[b_i, b^\dagger_j] = \delta_{ij}(1 - 2n_i)$, we obtain

$$[a_{q,i}, a^\dagger_{k,j}] = \delta_{i,j}\delta_{q,k} - \frac{2}{N} \sum_{C_1,C_2} e^{i(k-q)R_{C_1,C_2}} \sum_{l=1}^{2} \tilde{c}_{k-q,i,j,l} \, n_{R_{C_1,C_2};r_l} \tag{3.3.6}$$

with q, k being different momenta, $i, j \in \{1, 2\}$ being the index of the chosen eigenstate of $H^{\text{FPA}}_{\text{eff}}$, and $n_{R_{C_1,C_2};r_l}$ the number operator at the position $R_{C_1,C_2} + r_l$ in real space. For the second term we have defined $\tilde{c}_{k-q,i,j,l}$ as the resulting coefficients of the calculation, which do not matter here. The second term vanishes identically if we act on the ground state, as all number operators vanish. As the second term is proportional to $1/N$, we can neglect the whole term when acting on states with a small number of quasi-particles and taking the thermodynamic limit $N \to \infty$ (see [43, chapter 15] or for a similar case [44, chapter 4]). So, we can approximate the commutator as

$$[a_{q,i}, a^\dagger_{k,j}] \approx \delta_{i,j}\delta_{q,k} \, , \tag{3.3.7}$$

resulting in a bosonic commutation relation. In contrast to the real space relations in equation 2.3.3, we have no hardcore constraints for 'momentum quasi-particles' with the same quantum numbers. To be precise, the hardcore constraint from real-space maps to certain momenta combinations k, q which are forbidden and therefore $a^\dagger_{q,i} a^\dagger_{k,i} \equiv 0$. We will not go into further detail about this, as we just want to sketch the mathematical foundation of the approximation.

Now, we can define n-QP states analogously to equation 3.3.3 as

$$|n; k_1, i_1; \ldots; k_n, i_n\rangle = a^\dagger_{k_1,i_1} \cdots a^\dagger_{k_n,i_n} |0\rangle \ , \tag{3.3.8}$$

with k_j, i_j denoting the momentum and the chosen solution in the 1QP diagonalization of a single particle $|\epsilon_{i_j}(k_j)\rangle$.

Last, we rewrite our Hamiltonian $H^{\mathrm{FPA}}_{\mathrm{eff}}$ in terms of the new creation and annihilation operators. By definition, $H^{\mathrm{FPA}}_{\mathrm{eff}}$ is diagonal with respect to the states $|\epsilon_i(k)\rangle$. This lets us write the Hamiltonian as

$$H^{\mathrm{FPA}}_{\mathrm{eff}} = \sum_{k,i} \epsilon_i(k) a^\dagger_{k,i} a_{k,i} \ ,$$

where the sum goes over all momenta k and the two solutions $i \in \{1, 2\}$ for fixed k. Using this representation and equation 3.3.8 and applying the approximate commutation relation from equation 3.3.7 iteratively, we obtain the energy of an n-quasi-particle state as

$$H^{\mathrm{FPA}}_{\mathrm{eff}} |n; k_1, i_1; \ldots; k_n, i_n\rangle = (\epsilon_{i_1}(k_1) + \cdots + \epsilon_{i_n}(k_n)) |n; k_1, i_1; \ldots; k_n, i_n\rangle \ . \tag{3.3.9}$$

This justifies our physical intuition that the energy of a state with n non-interacting quasi-particles is just the sum of all 1QP energies.

It is left to show that the total momentum of $|n; k_1, i_1; \ldots; k_n, i_n\rangle$ is the sum of the single momenta k_j. For doing so, we use the real space representation of $a^\dagger_{k,i}$ in equation 3.3.5 to rewrite a series of n creation operators to create quasi-particles in real space with fixed distances to each other. This follows the original idea of rewriting multi-particle states in terms of the distances between the quasi-particles, as done in equation 3.1.5. For keeping notation comparably simple, we restrict ourselves to $n = 2$. We obtain

$$\begin{aligned} a^\dagger_{k,i} a^\dagger_{q,j} &= \frac{1}{N} \sum_{\substack{C_1,C_2 \\ D_1,D_2}} e^{ikR_{C_1,C_2}} e^{iqR_{D_1,D_2}} O(R_{C_1,C_2}, k, i) O(R_{D_1,D_2}, q, j) \\ &= \frac{1}{N} \sum_{\substack{C_1,C_2 \\ \delta_1,\delta_2}} e^{iqR_{\delta_1,\delta_2}} e^{i(k+q)R_{C_1,C_2}} O(R_{C_1,C_2}, k, i) O(R_{C_1+\delta_1,C_2+\delta_2}, q, j) \end{aligned}$$

with defining $O(R_{C_1,C_2}, k, i) := c_{k,i,1} b^\dagger_{R_{C_1,C_2};r_1} + c_{k,i,2} b^\dagger_{R_{C_1,C_2};r_2}$ as a short-hand notation for the real-space operators. In the last step we have introduced the distance in primitive cells R_{δ_1,δ_2}. Keeping R_{δ_1,δ_2} constant, we indeed obtain a phase $e^{i(k+q)R_{C_1,C_2}}$, being proportional to the total momentum $k_{\mathrm{tot}} = k + q$. This form is equivalent to the one in equation 3.1.9, where we defined the two quasi-particle state in momentum space. As by definition the phase difference between primitive cells corresponds to the momentum, we can extract the momentum of the two quasi-particle state $a^\dagger_{k,i} a^\dagger_{q,j} |0\rangle$ as k_{tot}. In principle, we can extend this to n-quasi-particle states doing the same steps as done for 2QP. It is important to mention again that we are not using the complete Hamiltonian

H_{eff} but the restricted $H_{\text{eff}}^{\text{FPA}}$ defined in equation 3.3.1. So, we neglected all interactions between the quasi-particles. When looking at the complete effective Hamiltonian, the momenta of the single quasi-particle will not be a good quantum number anymore as we have scattering processes between the single quasi-particles. Nonetheless, the approximation gives a very good estimate of the energy continuum, as can be seen in section 4.2.

3.4 Extrapolations

As the last part of this methods section, we will introduce two extrapolation techniques to improve the quality of our results. These 'results'—our physical quantities—are given in the form of *series expansions*. This comes from the perturbative form of our effective Hamiltonian H_{eff} in equation 3.2.6 and analogously the effective observables $\mathcal{O}_{\text{eff}}^{T=0}$ in equation 3.2.16. For the actual calculations, we will compute these perturbation series up to a certain order and get the corresponding physical quantity as a series expansion.

Although the series have the advantage that they are calculated in the thermodynamic limit, they often are not the optimal type of function to describe physical quantities accurately. As an example we can take phase transitions, which we can investigate by calculating the eigenvalues of the effective Hamiltonian. Those are specified by a singularity in a certain derivative m in the energy, denoting them as a phase transition of m-th order. This behavior can not be modeled with polynomials as they are differentiable for all their derivatives. The idea to overcome this problem is the extrapolation to another type of function that can have singularities. Furthermore, as the convergence radius of a obtained series in finite, we would like to enlarge the radius by the extrapolations. One such option is the Padé extrapolation [45, 46].

Definition 3.4. Given a power series $p(x) = \sum_{k=0}^{r} c_k x^k$ up to order r, we define the so-called *Padé extrapolant* as a rational function

$$P[n,m]_p := \frac{P_n(x)}{Q_m(x)} = \frac{\sum_{k=0}^{n} p_k x^k}{\sum_{k=0}^{m} q_k x^k} \tag{3.4.1}$$

whose series expansion has to be equal to p up to order $r = n + m$. This means $P[n,m]_p$ has to fulfill

$$\frac{\mathrm{d}^k}{\mathrm{d}x^k} P[n,m]_p \bigg|_{x=0} = \frac{\mathrm{d}^k}{\mathrm{d}x^k} p(x) \bigg|_{x=0} \tag{3.4.2}$$

for $k \in \{0, 1, \ldots, n+m\}$.

The coefficients p_k, q_k of the Padé extrapolant are obtained by solving the linear equations given by the definition in equation 3.4.2. As n, m are only restricted by $r = n + m$, we have a number of Padé extrapolants describing our power series. Furthermore, we can choose $r > n + m$, having extrapolants of lower degree. The resulting poles of these rational functions can be of physical origin or not. In the end of this section we will present a method trying to classify the poles and deal with them appropriately.

In addition to the Padé extrapolation, we also use the dlog-Padé as another extrapolation method [36, 47]. As foreshadowed in the name, the dlog-Padé makes use of the previously defined Padé extrapolant but does not apply it directly to our starting polynomial.

Definition 3.5. Given a power series $p(x) = \sum_{k=0}^{r} c_k x^k$ up to order r, we define the so-called *dlog-Padé* extrapolant as the Padé extrapolant of the logarithmic derivative of p given by

$$P[n,m]_{\mathcal{T}\left(\frac{\mathrm{d}}{\mathrm{d}x}\ln(p(x))\right)} = \frac{P_n(x)}{Q_m(x)}\,, \tag{3.4.3}$$

where $\mathcal{T}(f)$ is the Taylor expansion of a differentiable function f. For the integer values n, m, we obtain $r - 1 = n + m$ as we apply a derivative onto p. Using the dlog-Padé extrapolant, we can define the extrapolant $\mathrm{d}P[n,m]_p$ of the original power series p as

$$\mathrm{d}P[n,m]_p := \exp\left(\int_0^x \frac{P_n(t)}{Q_m(t)}\right)\,. \tag{3.4.4}$$

Equation 3.4.4 is the approximation of the original polynomial p. This is shown by using the fact that the Padé extrapolant $P[n,m]_p$ is the approximation of a polynomial p. So, by making the ansatz

$$P[n,m]_{\mathcal{T}\left(\frac{\mathrm{d}}{\mathrm{d}x}\ln(p(x))\right)} \approx \frac{\mathrm{d}}{\mathrm{d}x}\ln\left(p(x)\right)\,, \tag{3.4.5}$$

we obtain equation 3.4.4 by applying an integration over x and an exponentiation on equation 3.4.5.

The benefit of using $\mathrm{d}P[n,m]_p$ instead of the straight Padé extrapolant $P[n,m]_p$ is the existence of poles if the 'real physical function' f has 'critical values'. We define a function f which models the behavior near a critical value x_c as

$$f(x) = (1 - \frac{x}{x_c})^{-\theta}\,,$$

where θ is the corresponding critical exponent [12]. Calculating the logarithmic derivative of f, we obtain

$$\frac{\mathrm{d}}{\mathrm{d}x}\ln f(x) = \frac{\beta}{x - x_c}\,, \tag{3.4.6}$$

featuring a pole at x_c. As defined in equation 3.4.3, the dlog-Padé extrapolant is defined as the Padé of equation 3.4.6. So, we can extract x_c by looking at zeros of $Q_m(x)$, as those coincide with the existence of poles in the dlog-Padé extrapolant.

As for the Padé extrapolations, the $\mathrm{d}P[n,m]_p$ can feature non-physical poles that have to be sorted out. Before we describe the procedure of treating possible (un)physical poles, we define so-called 'families' of dlog-Padés or Padés to structure our extrapolations.

Definition 3.6. Given a power series $p(x) = \sum_{k=0}^{r} c_k x^k$ up to order r, we define a *family* of Padés $P[n,m]_p$ or dlog-Padés $\mathrm{d}P[n,m]_p$ as a set of those with a constant $\Delta = n - m$ and $r \geq n + m$ or $r - 1 \geq n + m$, respectively. For smaller degrees of n, m, we cut the order r of the original power series p appropriately, to match with the definitions 3.4 and 3.5.

When extrapolating a given power series p, we calculate Padés and dlog-Padés using the following scheme, as defined by Adelhardt in his master's thesis [36]. As the approach for both methods is very similar, we will restrict ourselves to dlog-Padés.

1. We calculate the different families of dlog-Padés with $|\Delta| \leq \Delta_{\max}$ with normally having $\Delta_{\max} \in \{1, 2\}$, as the quality of the extrapolations decreases for larger Δ.

2. Going through all calculated dlog-Padés, we search for poles (by looking for roots in $Q(x)$) which we can identify as unphysical. A pole can be considered unphysical if the pole is in an interval I of x where the existence of poles can be excluded, e.g., if the bare series is far away from a critical value or the pole is isolated to all other poles in a certain range. All dlog-Padés with a unphysical pole are discarded.

3. All families that only consist of one element after step 2 are discarded, too.

4. We calculate the approximate x_c by taking the mean of positions of all remaining poles of the dlog-Padés with the highest $m + n$ in each family, eventually restricting the area if we expect several critical points in the investigated area. We do not take the extrapolants of lower $m + n$ into consideration, as the quality of the extrapolation gets better for increased orders m, n. The variance of the calculated x_c and the different $\mathrm{d}P[n, m]_p$ give a measure of quality of the performed extrapolation.

Chapter 4

Discussion

In this chapter we will present the results of the performed research within the master's thesis. For the discussion we use the techniques introduced in the methods chapter 3. We will investigate the Kitaev honeycomb model as described in chapter 2, while restricting ourselves onto the polarized phase with $\|h\| \ll \|J\|$. As outlined in section 2.3, we can rewrite the Hamiltonian in a way that we fulfill all conditions for applying pCUT. The main advantage of using the effective Hamiltonian H_{eff}, calculated by the pCUT method, is the separation of the different quasi-particle subspaces as illustrated in figure 3.4. We divide the following chapter into two main sections 4.1 and 4.2 investigating the one and two quasi-particle subspace, independently. For the most of this chapter, we will focus on a fixed uniform magnetic field $h := h_x = h_y = h_z = 1$ and a uniform antiferromagnetic Kitaev coupling $J := J_x = J_y = J_z < 0$ as perturbation, following several other papers and theses [14, 16, 17, 21, 22]. For the one quasi-particle sector we will also investigate the more general case of different h_α in section 4.1.1.2 and the case of one vanishing J_α coupling in section 4.1.1.3 obtaining the so-called *Compass model*. At the end of this chapter, we will compare our results to data calculated with the *density matrix renormalization group* (DMRG) technique [14]. This serves as a confirmation of our results and gives more insight into the DMRG data, as we can separate single processes and quasi-particle sectors from each other.

As outlined in section 3.1, the transition to momentum states simplifies the calculation and discussion. For defining the respective momentum k, we use the decomposition in the dual basis, as done in equation 3.1.8. We define

$$k = \sum_{i=1}^{2} \frac{k_i}{2\pi} b_i = \frac{k_1 b_1 + k_2 b_2}{2\pi}\,, \tag{4.0.1}$$

with $k_i := \frac{n_i}{C_i^{\max}} \cdot 2\pi$ and $n_i \in \mathbb{Z}$ for the 2D Kitaev lattice. In the thermodynamic limit we can choose k_i arbitrarily. A value $k_i = 0$ corresponds to no phase difference between two sites with distance a_i and $k_i = 2\pi$ to a phase shift of 2π between sites with the respective distance. With this definition we can scan through the entire *Brillouin zone* by varying k_1, k_2 between 0 and 2π.

For the calculation of H_{eff}, we use the C++ implementation named '*Solver*', implemented and used by the group of Schmidt [36, 47–51]. More information on the Solver itself is given in [40, section 2.3]. The Solver takes the bra- and ket-state, the finite cluster with all sites and bonds, and a maximum order $o_{\max}$ to which the hopping is calculated. The output is given as a series in the perturbation parameters J_x, J_y, J_z and can be used for extrapolations described in section 3.4. For the communication to the 'Solver' and the creation of clusters and calculation of dispersion, gaps, and spectral quantities I implemented several modules and classes written in python. Those are preparing the Solver to calculate single hopping elements, read out the result again and combine all hoppings to calculate the wanted physical quantities. To minimize the size of the clusters for calculating the effective hoppings, we used clusters which are optimized to the different combinations of perturbation couplings J_x, J_y, J_z and their respective processes. By taking those into account we were able to reduce the size of the clusters for calculation by simultaneously increasing the total number of calculations with the Solver. The creation of minimal clusters for the calculation of H_{eff} are described in detail in appendix A.

4.1 One-particle sector

First, we will investigate the one quasi-particle subspace. Using the decomposition of H_{eff} in equation 3.2.7 into the n quasi-particle operators H_n, we have to calculate H_1 to obtain the dispersion and gap of the 1QP states. The effective hopping amplitudes are presented in appendix B. Using the Solver program, we were able to calculate the dispersion in the case of arbitrary J_x, J_y, J_z up to order 8 using a machine with 30 cores for around 2 days.

For the calculation of spectral quantities, we have to calculate $\mathcal{O}_{1,0}$, as defined in equation 3.2.16. This is done by calculating hopping elements of the form $\langle i \mid \mathcal{O}_{\text{eff}}^{T=0} \mid 0\rangle$. As the calculation of $\mathcal{O}_{\text{eff}}^{T=0}$ has an additional operator $\mathcal{O}$ in equation 3.2.14 for the same order in perturbation, the maximum order is reduced to 7 on the same scale of time as before.

4.1.1 Dispersion and gap

We start with the dispersion and gap of the one quasi-particle states. Using the translational invariance of our model, we can reduce the 1QP Hamiltonian to a 2×2 matrix, which has to be diagonalized for obtaining the dispersion (for more information see section 3.1). Because of the two-site primitive cell, we obtain two eigenstates with respective eigenenergies. These two eigenenergies form the dispersion, as those depend on the chosen momentum. The dispersion gives us the energy of one 'stable' quasi-particle with a certain momentum. A positive energy implies an energy gain of the system when transition from the ground state to the 1QP state. For this case the energetically favored state is the ground state. If the energy becomes negative, the system gains energy by adding one quasi-particle. In general, we assume that the addition of more quasi-particles reduces the energy further. Because of that, we expect a phase transition for an energy difference equal to zero. For measuring this energy loss or gain, we investigate the gap corresponding to the minimum of the 1QP dispersion. The gap is calculated by taking the minimum in energy for all eigenenergies and momenta. For positive 1QP energies the band gap is the minimal energy that has to be put into the system to create one quasi-particle.

This section is divided into different choices of our parameter J_α, h_α. First, we will look at the most common case of a uniform magnetic field $h_x = h_y = h_z$. Afterwards, we will vary the direction of the magnetic field. Last, one special case is investigated by setting one of the J_α to zero.

4.1.1.1 Uniform magnetic field

We start the discussion with a uniform magnetic field $h := h_x = h_y = h_z = 1$. As we normalized our Hamiltonian in section 2.3.2, the quasi-particle energy in the case of vanishing Kitaev couplings J_α is set to 1. In figure 4.1 a first plot of the dispersion of the two 1QP bands is shown for the case of an antiferromagnetic Kitaev coupling $J := J_x = J_y = J_z = -0.1$. We choose $J \ll h$, as demanded by the perturbative ansatz in pCUT. The two different plots show the two solutions of the diagonalization of the 2×2 Hamiltonian matrix for different momenta k, sorted by total energy. The two axes of the plots are the two coefficients k_1, k_2 for the dual basis as defined at the beginning of this chapter in equation 4.0.1. As we have chosen k_1, k_2 over two 2π periods we obtain a recursive pattern in both plots. This recursion originates in the definition of the momentum as a phase between different primitive cells. So, for multiples of 2π in k_1, k_2 we obtain the same wave function as we have gained a phase of 2π in the exponential in the momentum state (see equation 3.1.7). So, for the energies it will suffice in the following to only investigate $k_1, k_2 \in [0, 2\pi]$.

The two bands touch each other for the momenta $k_1 = 4/3\pi, k_2 = 2/3\pi$ and $k_1 = 2/3\pi, k_2 = 4/3\pi$ in the first Brillouin zone. When increasing the interaction parameter J, this touching point vanishes, as the two bands become more separated. In the plots, we have split the bands strictly due to their energy. The band splitting is maximal for vanishing momenta. We can observe a 6 fold rotation symmetry for the dispersion, coming from the honeycomb structure and the choice of parameters. As the dual lattice of a honeycomb lattice is a rotated honeycomb lattice (as can be seen by the dual basis b_1, b_2 in section 3.1), we can understand the overall structure of the Brillouin zone from the basic lattice structure in real space. Nonetheless, we break the lattice-symmetry by choosing different values for the h_α or J_α, as we will investigate later.

The next interesting observation is that the 1QP energy is lowered for all momenta and for both bands, as the unperturbed energy starts at an energy of 1. This means that the Kitaev coupling strictly reduces the energy of the quasi-particle, regardless of its momentum. In the following we try to give an explanation for this behavior.

As mentioned at the beginning of this section, after Fourier transformation our Hamiltonian is of size 2×2, as we have separated the different momenta from each other. The only degree of freedom is the place r in the primitive cell, as

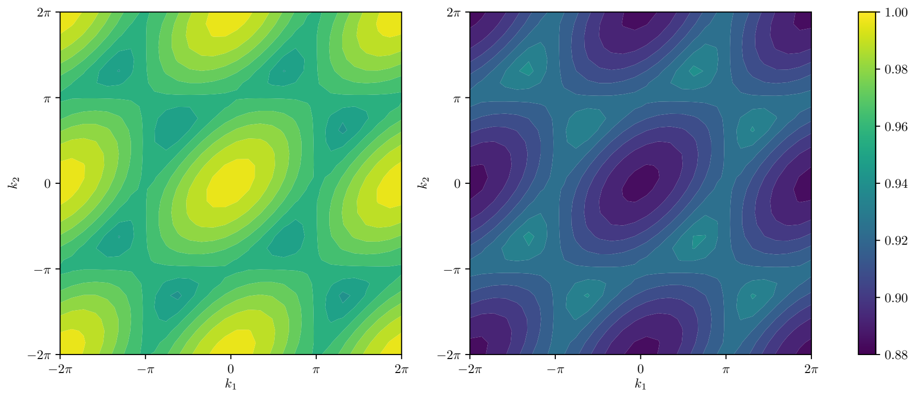

Figure 4.1: Dispersion of both 1QP bands for $J_x = J_y = J_z = -0.1$ and $h_x = h_y = h_z = 1$. The band with the larger energies (upper band) is plotted on the left, the band with the smaller energies (lower band) is plotted on the right. The pattern of the plots is recursive with a periodicity of 2π for k_1, k_2. The total minimum and maximum lies at a vanishing momentum $k_1 = k_2 = 0$. All 1QP energies are lowered by the perturbative Kitaev interaction, as the unperturbed states have an energy of 1 for all momenta. The two bands intersect with each other for momenta $k_1 = 4/3\pi, k_2 = 2/3\pi$ and $k_1 = 2/3\pi, k_2 = 4/3\pi$ modulo 2π.

given in the states $|1, k; r\rangle$. So, most general we can write our Hamiltonian as

$$H_{\text{eff}} = \begin{pmatrix} a & c \\ \bar{c} & b \end{pmatrix} ,$$

with $a, b \in \mathbb{R}[x]$, $c \in \mathbb{C}[x]$, and the perturbation parameter x. This matrix can easily be diagonalized (when not solving the occurring root). The two eigenvalues $\lambda_\pm$ are given as

$$\lambda_\pm = \frac{1}{2}\left(a + b \pm \sqrt{(a-b)^2 + 4|c|^2}\right) =: \mathcal{S} \pm \Delta .$$

We divided the eigenvalues into the 'common terms' $\mathcal{S} = 1/2(a + b)$ and the 'splitting terms' $\Delta = 1/2\sqrt{(a-b)^2 + 4|c|^2}$. As stated, both eigenvalues drop for rising absolute values of J. So, the common terms $\mathcal{S}$ have to be the driving force behind this effect, as Δ instead increases the difference in energy of the two eigenvalues. $\mathcal{S}$ is proportional to the terms a, b which are given as

$$a = \langle 1, k; r_1 \mid H_{\text{eff}} \mid 1, k; r_1 \rangle , \quad b = \langle 1, k; r_2 \mid H_{\text{eff}} \mid 1, k; r_2 \rangle ,$$

meaning all hoppings which do not change the site in the primitive cell. When looking at first order in the perturbation series given by pCUT, we qualitatively obtain the following hoppings

$$H_1 |n, R; r_1\rangle \propto J(3|n, R; r_1\rangle - |n, R + a_1; r_2\rangle - |n, R + a_2; r_2\rangle - |n, R; r_2\rangle) . \tag{4.1.1}$$

The last three states correspond to a 'nearest-neighbor' hopping to one of the neighboring sites. The first term is a *local hopping term* (meaning the position of the quasi-particle does not change), therefore being the only one not changing the place in the primitive cell. For lower values of J, the lower powers in the

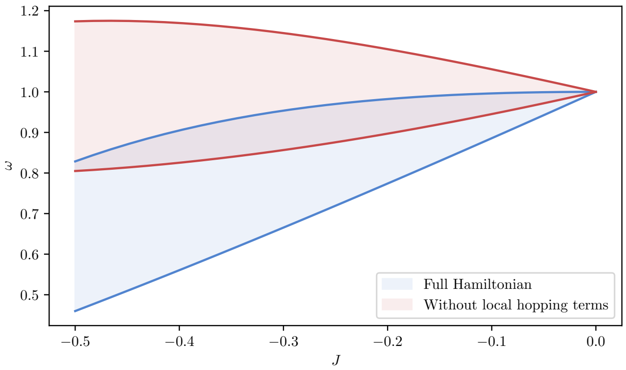

Figure 4.2: Maximum and minimum of the 1QP dispersion for uniform J, h. The blue band is for the full Hamiltonian as printed in figure 4.1, the red band for neglecting local hopping terms. In contrast to the full dispersion, the overall trend of the energies for neglected local terms has shifted upwards. This implies that the local hopping terms decrease the overall energy. For more information see the main text.

perturbation series should have the largest effect. Thus, we can assume that the local hopping term, as sketched in equation 4.1.1, is the main contribution for the common terms $\mathcal{S}$. The reason why the local hopping term decreases the energy is the antiferromagnetic interaction ($J < 0$) between neighboring spins. As the quasi-particle is defined as a spin flip, the flipped spin couples to the neighboring spins in an attractive way, thus lowering the energy of the system.

To check our guess, we compare the maximum and minimum of the dispersion for the full Hamiltonian and a Hamiltonian where the local hopping terms were dropped in figure 4.2. We see that the overall trend $\mathcal{S}$ changes when neglecting the local terms, while the splitting Δ stays the same. Now, the upper band of the restricted Hamiltonian increases in energy if we increase the perturbation. This confirms our assumption that the main attractive effect is given by the local hopping terms for small perturbations. We will use this observation later on for the discussion of two quasi-particles and their anti-bonding effect which originates from the same local hopping terms.

To complete the first rough overview of the dispersion, we investigate the dispersion for ferromagnetic Kitaev interactions $J > 0$ in figure 4.3. From the previous discussion, we can understand the overall trend to larger energies for increasing couplings again by means of the local hopping. Taking equation 4.1.1 into account, the spin flip increases the energy of the system as the coupling prefers neighboring spins to point in the same direction. Despite this difference, the overall structure is the same as for antiferromagnetic interactions.

From our previous observations we found out that the minimum of the dispersion lies at a vanishing momentum $k = 0$, as long as we restrict the total perturbation $|J|$ to comparably small values. For investigating the band gap Δ of one quasi-particle, we can use the dispersion of the lower band at $k = 0$. As we calculate the 1QP dispersion with pCUT, the result is given in form of a series expansion.

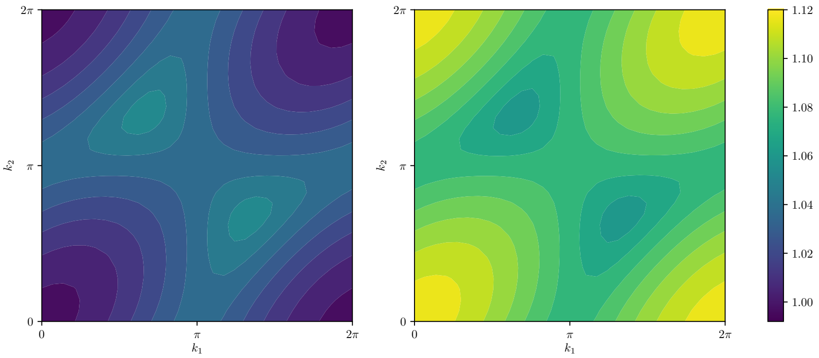

Figure 4.3: Dispersion of both 1QP bands for $J = 0.1$ and $h = 1$. The pattern of the plots is recursive with a periodicity of 2π for k_1, k_2. The total minimum and maximum lies at a vanishing momentum $k_1 = k_2 = 0$. The two bands intersect with each other for momenta $k_1 = 4/3\pi, k_2 = 2/3\pi$ and $k_1 = 2/3\pi, k_2 = 4/3\pi$ modulo 2π. In contrast to antiferromagnetic Kitaev interactions, $J > 0$ trends to increase the energy of the system, as the system prefers neighboring spins being aligned in the same direction.

For the two eigenvalues we obtain the series

$$\begin{aligned} \omega_1(k=0) =& 1.0 - 0.33333J^2 + 0.47043J^3 - 0.40329J^4 + 0.12999J^5 \\ &+ 0.28969J^6 - 0.68312J^7 + 0.77046J^8 \\ \omega_2(k=0) =& 1.0 + 1.1547J + 0.11111J^2 - 0.06415J^3 + 0.01783J^4 \\ &- 0.00761J^5 + 0.00451J^6 - 0.0053J^7 + 0.00544J^8 \,, \end{aligned} \tag{4.1.2}$$

where for readability we dropped the higher digits. These results are in agreement to [47, pages 57 and 67] for the thermodynamic limit. Depending on the sign of J, the eigenvalue series form the upper or lower band. Both series do not converge very well up to the computed order. This means the coefficients of higher orders in J do not get smaller or even vanish. Because of that we have to take higher orders into account as they play a major role when increasing the perturbation parameter. Another interesting feature is the vanishing first order for $\omega_1(k = 0)$. As ω_1 forms the upper band for $J < 0$, we see the result of our previous discussion, as we have no positive contribution in first order which would increase the energy of the 1QP state. This vanishing first order comes from symmetries in the chosen parameters. As we will see later on, we get first order contributions when breaking the symmetry of the uniformly chosen parameters.

The two series are plotted in figure 4.4. To get an idea of the quality of the calculated series, we not only plot the values using the total series but also restrict the series to lower orders. If these different maximum orders lie approximately on top of each other, we can assume the series to converge well. As we see in the right figure, the lower orders already describe the behavior of $\omega_2(0)$ quite good. So, we can assume that higher orders in ω_2 will not change the overall trend drastically. In contrast, the dispersion ω_1 scatters more widely for the different maximum orders. Thus, we have to suppose that our given series up to order 8 does not describe the real dispersion (meaning the full series) very well.

As already mentioned, the classification of upper and lower band depends on

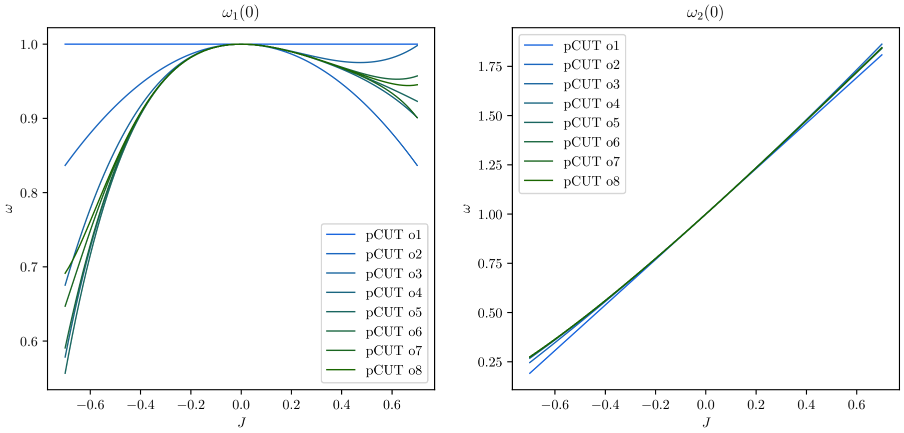

Figure 4.4: One quasi-particle dispersion for vanishing momentum $k = 0$. The two figures visualize the two eigenvalues of the effective Hamiltonian, as given in equation 4.1.2. The series is plotted for different maximum orders going up to order 8. The categorization of the upper and lower band depends on the sign of J. While the ω_2 series converges well in the given area of J, the ω_1 series spread more widely for rising $|J|$. When investigating the minimum of both solutions for different J, we obtain smaller values for antiferromagnetic J. So, the gap depends heavily on the sign of J.

the sign of J. For $J > 0$, clearly ω_1 describes the lower band (and with that also the 1QP band gap) as the energies of ω_2 rise for larger J values. For $J < 0$, both eigenvalues trending downwards. For the given values of $J < 0$, the eigenvalue ω_2 is smaller than ω_1. When comparing the gap for antiferromagnetic and ferromagnetic couplings, we notice a different speed of gap closing for rising $|J|$. This coincides to our previous discussion that the spin-flip prefers a system with antiferromagnetic bonds.

To increase the quality of our series, we can use the extrapolation techniques, which were introduced in section 3.4. The goal is to get better estimates of ω_1, ω_2 for larger absolute couplings $|J|$. In the following, we will restrict ourselves to the band gap Δ for $J > 0$ and $J < 0$, separately. The results of the extrapolations are plotted in figure 4.5. In addition, the bare series up to different maximum orders is plotted in blue to green as done in figure 4.4. The left figure shows the band gap Δ for antiferromagnetic J and the right one for ferromagnetic J. For $J < 0$, the good quality of the bare series pursues in the similar results of the different Padés and dlog-Padés. The gap closes in the area of good convergence as the extrapolations are very similar. As introduced in section 3.4, we can extract the closing of the gap by the zeros of the denominator in the dlog-Padés. By taking the mean of all zeros around $J \approx -1.1$, we obtain an average J_c for the closing of the band gap of

$$J_c = -1.14721 \pm 0.00536\,.$$

This is in agreement to [47, page 68]. The small deviation comes from the slightly different declaration and treatment of defective approximants as described at the end of section 3.4. As we see from our calculations, the gap seems to close in a comparably flat manner, meaning the gradient in the area of the gap closing is very small. This results in an instable calculation of the critical coupling, as

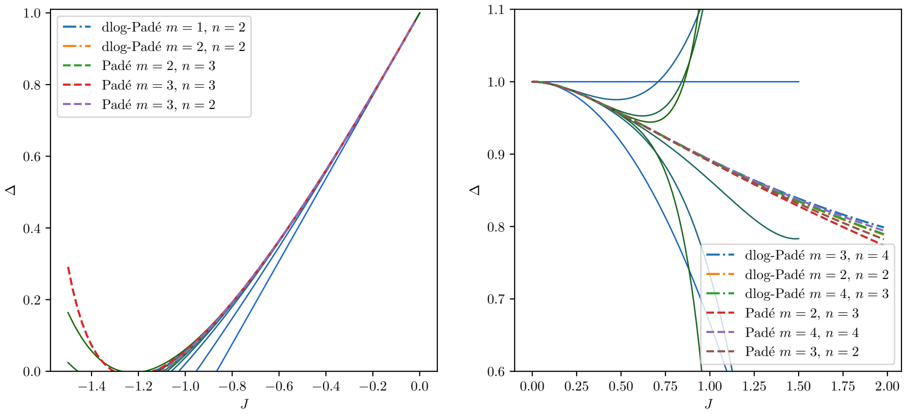

Figure 4.5: One quasi-particle gap for antiferromagnetic couplings in the left figure and ferromagnetic couplings in the right figure. The bare series are plotted blue (low maximum order) to green (high maximum order). The Padé and dlog-Padé extrapolants are plotted in various colors with m, n being the degree of the denominator and numerator, respectively. The extrapolants are chosen according to the scheme described at the end of section 3.4. For $J < 0$, we are able to estimate the point where the band gap vanishes with good quality. For $J > 0$ the band gap closes not fast enough to get a reasonable estimate of the gap-closing within the convergence radius.

small errors in the gap lead to large deviations in J_c. In comparison to Gohlke et al. and Zhu et al. [14, 16] who calculated a phase transition at $J_c \approx 1.39$ using DMRG, our result underestimates this transition point a bit, which can be explained by the large coupling and the flat closing. Nonetheless, our method is able to detect the phase transition in the correct coupling region.

Going to the gap extrapolation for ferromagnetic J, we observe a highly increased quality of convergence in a larger area, when comparing the dlog-Padé and Padé extrapolants with the bare series. Nonetheless, in the plotted area the band gap has no trend towards closing. As the quality decreases for large J, it is not feasible to estimate the closing parameter J_c, as done for antiferromagnetic J. Transferring the transition point in [16] to our used units, we obtain a Kitaev coupling of around $J_c \approx 25$. This is far away from our perturbative limit $J \ll h$, so it is comprehensible that we are not able to estimate this phase transition.

The overall behavior of the gap is in qualitative agreement of the findings of other groups, as described in section 2.2. For ferromagnetic couplings, the polarized phase extends significantly longer than for antiferromagnetic couplings. This explains why it is easier for us to estimate the phase transition point for antiferromagnetic couplings when starting out of the polarized phase.

4.1.1.2 Varying the magnetic field

After discussing the properties of the most common cases of magnetic field and Kitaev coupling, we will now start to change these parameters. In this section we will vary the direction of the magnetic field. As a short side note: It is not interesting to vary the absolute strength $|h|$ of the magnetic field, as a change in $|h|$ can be compensated by an adjusted coupling strength $|J|$.

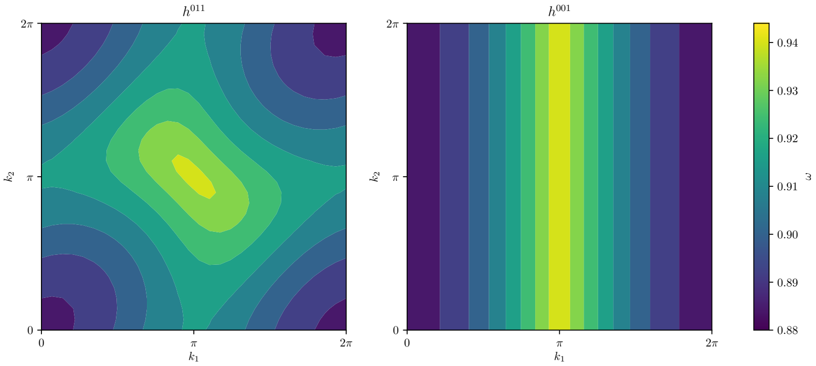

Figure 4.6: Dispersion of the lower 1QP band for $J_x = J_y = J_z = -0.1$ and varying h directions. The upper band is symmetric to the respective upper band, as seen in figure 4.1. On the left-hand side, the dispersion is given for $h^{011} = (0,1,1)^T \cdot (\sqrt{3}/\sqrt{2})$ and on the right-hand side for $h^{001} = (0,0,1) \cdot \sqrt{3}$. As for the uniform magnetic field, the minimum lies at $k = 0$, thus the gap is located at vanishing momentum. In contrast to h^{111}, the 6-fold symmetry from the lattice is broken. For h^{001}, the dispersion does not depend on k_2, as the quasi-particles can not move in direction of k_2. See the main text for more information.

In general, three different limiting cases seem to be interesting: First, our already described case of a uniform field $h^{111} = (1,1,1)^T$. Next, we can 'eliminate one of the directions', obtaining directions $(0,1,1)^T, (1,0,1)^T, (1,1,0)^T$. As those three can be transformed into each other by rotations of the system, we will just investigate one of the three directions, namely $h^{011} = (0,1,1)^T \cdot (\sqrt{3}/\sqrt{2})$. The normalization factor $\sqrt{3}/\sqrt{2}$ is added to ensure $\|h^{(1)}\| = \|h^{(2)}\|$, making the comparison easier. Last, we can eliminate another direction. Using the same argument as for $h^{(2)}$, we can restrict ourselves onto the direction $h^{001} = (0,0,1)^T \cdot \sqrt{3}$.

Again, we look at the 1QP band structure for the three cases. As we have already intensively discussed h^{111}, we will stick to the other two cases and refer to the previous section for comparison. The dispersion for h^{011}, h^{001} is given in figure 4.6. Because upper and lower band are symmetric to each other for small perturbations, we only plot the lower band. As for the h^{111} case, the minimum of the lower band—and thus also the gap—is located at $k_1 = k_2 = 0$. Analogously, the maximum of the upper band also lies at vanishing momentum k. The *bandwidth*—meaning the range between maximum and minimum of both bands—is roughly the same as for the h^{111} case. As already hinted in the previous discussion, the 6-fold symmetry coming from the lattice structure is broken for both varied magnetic fields. It stands out that the dispersion for h^{001} does not depend on the momentum in k_2 direction. To justify this behavior, we calculate the Hamiltonian $\mathcal{H}$ in equation 2.3.5 for the magnetic

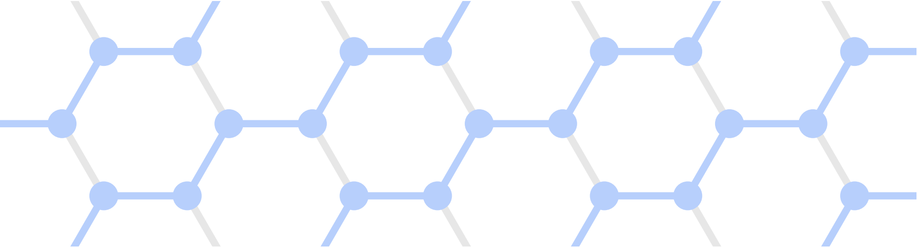

Figure 4.7: Visualization of the dynamics for the Kitaev honeycomb model in a magnetic field pointing in z-direction. As argued in the main text, the only possible movement for a quasi-particle is along the x, y-bonds, marked with blue. So, a quasi-particle stays within its one-dimensional chain. The z-bonds, indicated in light gray, couple the neighboring sites with a density-density interaction. Thus, the different chains do not interchange quasi-particle but do interact if quasi-particles are next to each other.

field in z-direction. We obtain the t-operators

$$\begin{aligned} t_0^\alpha(i,j) &= J_\alpha C(b_i^\dagger b_j + b_i b_j^\dagger) \\ t_0^z(i,j) &= J_z C(1 - 2n_j - 2n_i + 4n_i n_j) \\ t_{-1}^\alpha(i,j) &= 0 \\ t_{-2}^x(i,j) &= J_x C b_i b_j \\ t_{-2}^y(i,j) &= -J_y C b_i b_j \\ t_{-2}^z(i,j) &= 0\,, \end{aligned} \tag{4.1.3}$$

analog to equation 2.3.6. Focussing on the operators acting on the z-bonds, we see that all hopping terms have vanished. The only coupling along the z-bonds is given as a density-density interaction between the neighboring sites. As a result of this, a quasi-particle can only hop along the x- and y-bonds. Effectively, we can reduce our general honeycomb structure into single chains consisting of x, y-bonds which are coupled to each other via the z-bonds, as visualized in figure 4.7. The restriction of movement along these chains explains the independency of the dispersion along k_2. As k_2 is the momentum along the lattice vector a_2 (see figure 3.1), a change in this variable has no impact on the system as the quasi-particles can not move along the a_2 direction. So, k_1 describes the complete dynamics by defining the momentum of a quasi-particle in the separated chains. We will see that this limiting case is very similar to the Compass model, which will be discussed in the following section.

As done for the uniform magnetic field in figure 4.5, we move on investigating

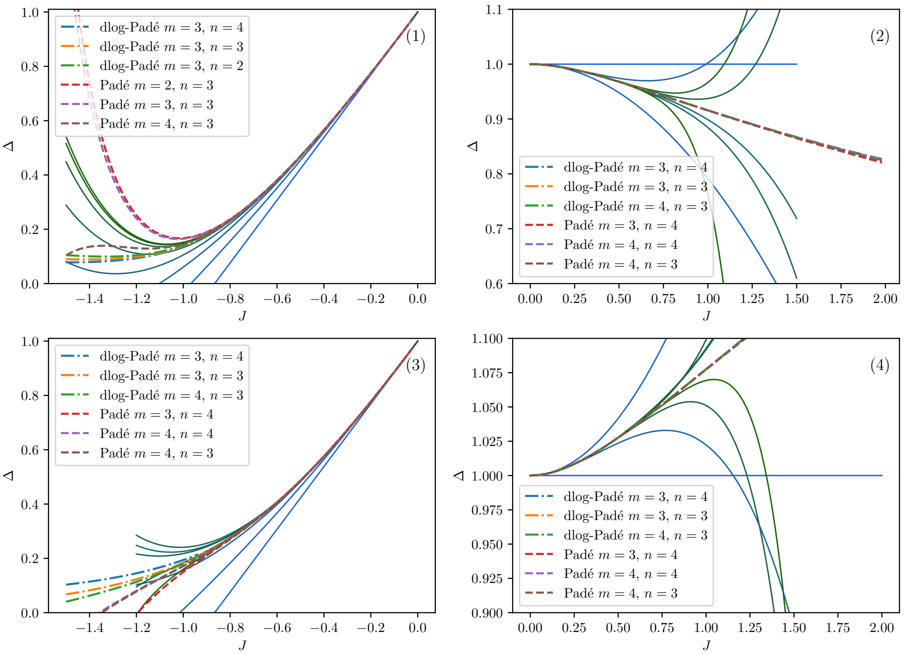

Figure 4.8: One quasi-particle gap for different magnetic fields. For figures (1) and (2) the magnetic field h^{011} and for (3) and (4) the magnetic field h^{001} is chosen. On the left-hand side, the gap is plotted for antiferromagnetic couplings, on the right-hand side for ferromagnetic couplings. The bare series are plotted blue (low maximum order) to green (high maximum order). The Padé and dlog-Padé extrapolants are plotted in various colors with m, n being the degree of the denominator and numerator, respectively. The extrapolants are chosen according to the scheme described at the end of section 3.4. For $J > 0$ the band gap closes not fast enough to get a reasonable estimate of the gap-closing within the convergence radius. Moreover, for h^{001} the gap gets even larger for rising coupling in the investigated coupling area.

the gap of the two new cases. By applying pCUT, we obtain the series

$$\begin{aligned}
\omega_1^{011}(k=0) =& 1.0 - 0.20833J^2 + 0.21049J^3 - 0.1033J^4 + -0.01434J^5 \\
&+ 0.05282J^6 + 0.02915J^7 - 0.20309J^8 \\
\omega_2^{011}(k=0) =& 1.0 + 1.1547J + 0.125J^2 - 0.09021J^3 + 0.04485J^4 \\
&- 0.02736J^5 + 0.01403J^6 - 0.00546J^7 - 0.00102J^8 \\
\omega_1^{001}(k=0) =& 1.0 + 0.16667J^2 - 0.14434J^3 + 0.06944J^4 + 0.001J^5 \\
&- 0.04167J^6 + 0.04795J^7 - 0.02972J^8 \\
\omega_2^{011}(k=0) =& 1.0 + 1.1547J + 0.16667J^2 - 0.14434J^3 + 0.06944J^4 \\
&- 0.01504J^5 - 0.02315J^6 + 0.03375J^7 - 0.02384J^8 \,,
\end{aligned}$$

where ω_i^{011} are the two eigenvalue-series for the magnetic field h^{011} and ω_i^{001} for h^{001}. The results are plotted in figure 4.8. Subfigures (1) and (2) are the gaps for $J < 0$ and $J > 0$ for the magnetic field h^{011}, respectively. Subfigures (3) and (4) show the gap for the magnetic field h^{001}. Especially for the antiferromagnetic coupling we obtain a very similar qualitative structure to that of the uniform magnetic field. Nonetheless, in both cases the gap closes not for the same but for larger couplings. As the quality of the extrapolation decreases, the estimate of the critical coupling is way rougher. By calculating the average of all denominator zeros positions, we obtain

$$J_c^{011} = -1.53, \quad J_c^{001} = J_c = -1.79144 \pm 0.09807\,,$$

where J_c^{011} is the approximate critical coupling strength for the case of the magnetic field h^{011}. The critical coupling J_c^{001} is defined analogously. As only one dlog-Padé features a pole in the investigated coupling region for h^{011}, we can not quantify the uncertainty. But the fact of only having one vanishing dlog-Padé supports the impression of poor quality of the extrapolation. Comparing the estimation for h^{001} with literature [19, 52], the value obtained by DMRG is around $J_c^{001} \approx -1.72$. As for the uniform magnetic field, the series expansion and their extrapolations give a qualitative correct result but are not very accurate, as we are far away from the perturbative limit $J \ll h$.

For ferromagnetic couplings the gap closes even slower than for the uniform magnetic field. For h^{011}, the qualitativ behavior of the gap is similar to the one in the case of the uniform field. For h^{001}, the gap even gets larger, when increasing the ferromagnetic coupling. A possible explanation is again the strong local hopping that prefers in the ferromagnetic case the same direction of spins. The reason for even larger energies could be the restricted movement of the quasi-particles. Because the movement of the quasi-particle decreases the energy, as can be seen in the hopping terms in equation 4.1.3 or in the schematic description in equation 4.1.1, a restriction to the 1D chains could be a further contribution for higher energies of the 1QP states. We will see in the following section that the coupling between the chains breaks the symmetry of ferromagnetic and antiferromagnetic couplings.

4.1.1.3 Special case: Compass model

After varying the magnetic field direction in the last section, we will now vary the Kitaev couplings J_α to the limiting case $J_z = 0$. This model is known as the Compass model and is a one-dimensional model. When neglecting the interactions along the z-bonds, we obtain independent one-dimensional chains similar to the case of a magnetic z-field investigated in the last section. In contrast to the z-field case, the different chains are not coupled, so we can restrict ourselves to one of the chains. We obtain the new general Hamiltonian by setting all $t_i^z = 0$ in equation 2.3.6.

Before investigating the model for different magnetic field directions, we will stick to the transversal magnetic field $h^{001} = \sqrt{3}(0,0,1)^T$. This has the advantage that the model is analytically solvable. This gives us the opportunity to not only describe the system exactly for all couplings and magnetic field strengths but also compare the analytical solution with the perturbation series, which we obtain with pCUT. Restricting the Hamiltonian to the z-field, we obtain

$$\begin{aligned}\mathcal{H}_{\mathrm{CM}} = -\frac{N}{2} + \sum_i n_i - \frac{1}{2\sqrt{3}}\Big[& J_x \sum_{x-\text{links } i,j} (b_i^\dagger b_j^\dagger + b_i^\dagger b_j + \text{h.c.}) \\ & + J_y \sum_{y-\text{links } i,j} (-b_i^\dagger b_j^\dagger + b_i^\dagger b_j + \text{h.c.})\Big]\,,\end{aligned}$$

where h.c. stands for the 'hermitian conjugate' of the previous terms. The Hamiltonian consists out of pair creation and annihilation terms $b_i^{(\dagger)} b_j^{(\dagger)}$ and hopping terms $b_i^\dagger b_j$ along the x, y-bonds. In the following, we will derive the diagonalization of the Hamiltonian, as done by [53]. The diagonalization is done in three steps: We will first apply the Jordan Wigner transformation to map our hardcore bosons to *fermions*. Next, we apply a Fourier transformation to exploit translational symmetry. Last, we apply a Bogoliubov transformation (fondly called 'Bogo' in our group) to get rid of processes changing the number of quasi-particles.

Jordan Wigner transformation We begin with the *Jordan Wigner transformation*. Our hardcore bosons fulfill the commutation relations

$$b_i b_i = b_i^\dagger b_i^\dagger = 0 \quad [b_i, b_j^\dagger] = \delta_{ij}(1 - 2n_i) \,.$$

as defined in equation 2.3.3. We now define new operators a_j depending on b_j, given as

$$a_j = e^{i\phi_j} b_j \,, \quad \text{with } \phi_j = \pi \sum_{k<j} b_k^\dagger b_k \,.$$

The relation $k < j$ in the last sum orders the single sites with respect to their position. As we are in a one-dimensional system, this can be done by imposing the relation 'k left from j'. These new operators $a_j^\dagger, a_j$ fulfill the anticommutation relations

$$\{a_j, a_l^\dagger\} = \delta_{lj} \,, \quad \{a_j, a_l\} = \{a_j^\dagger, a_l^\dagger\} = 0 \,,$$

as can be calculated by using the hardcore boson commutation relations. Another important identity is the equivalence of pairs of fermion and hardcore boson operators, reading

$$a_j^{(\dagger)} a_{j+1} = b_j^{(\dagger)} b_{j+1} \,.$$

Because of the last relations, we can rewrite our Hamiltonian $\mathcal{H}_{\mathrm{CM}}$ directly in terms of the new fermionic operators $a^\dagger, a$, by simply replacing the operators.

Fourier transformation As the Compass model is a limiting case of our full model, we can exploit the translational invariance, as we did in section 3.1. For the one-dimensional chain we introduce the operators in k-space as

$$a_{k,r} = \frac{1}{\sqrt{N}} \sum_C e^{ikR_C} a_{C,r} \,, \quad a_{C,r} = \frac{1}{\sqrt{N}} \sum_k e^{-ikR_C} a_{k,r} \tag{4.1.4}$$

where N is the number of sites, R_C is the position of the depicted primitive cell, and $r \in \{r_1, r_2\}$ is the primitive cell vector. For a finite lattice, the k values are again restricted as in equation 3.1.8 due to the periodic boundary condition. We use the notation $a_{C,r} \equiv a_j$ for the operators in real space, to divide the position j into the primitive cell at position R_C and the relative position r within the primitive cell. For consistency, we use the same notation as in equation 3.1.9.

As a short note: When introducing the Fourier transformation, we applied the transformation directly on the states. We could have also acted directly on the operators, as we do it here or in the free particle approximation in section 3.3. When using equation 4.1.4, we obtain the Hamiltonian $\mathcal{H}_{\text{CM}}$ depending on the momentum operators as

$$\begin{aligned}\mathcal{H}_{\text{CM}} = -\frac{N}{2} &+ \sum_k a^\dagger_{k,r_1} a_{k,r_1} + a^\dagger_{k,r_2} a_{k,r_2} \\ &- \frac{1}{2\sqrt{3}} \Big[J_x \sum_k (a^\dagger_{k,r_1} a^\dagger_{-k,r_2} + a^\dagger_{k,r_1} a_{k,r_2} + \text{h.c.}) \\ &\qquad + J_y \sum_k e^{ika_1} (-a^\dagger_{k,r_2} a^\dagger_{-k,r_1} + a^\dagger_{k,r_2} a_{k,r_1} + \text{h.c.}) \Big] .\end{aligned}$$

As before, we have 2QP creation and annihilation terms, where two particles of opposite momentum are created to fulfill momentum conservation and 'hopping terms' with particles which keep their momentum, when hopping between the places in the primitive cell. The a_1 in the phase-factor of the last terms is the distance between neighbored primitive cells, as defined in section 3.1.

Bogoliubov transformation The last problem we have to solve for diagonalizing $\mathcal{H}_{\text{CM}}$ is the existence of the pair creation and annihilation operators. Having those terms induces the difficulty that the quasi-particle number is not conserved. Thus, up to this point, we can not restrict the Hilbert space to a finite subspace as in principle we have to take all quasi-particle numbers into account. One solution for this problem is the *Bogoliubov transformation*. The basic idea is another transformation to new fermionic operators such that the non-diagonal terms vanish. For doing so, we can write our Hamiltonian in a quadratic form using the fermionic anticommutation relation:

$$\mathcal{H}_{\text{CM}} = \sum_{k>0} \begin{pmatrix} a^\dagger_{k,r_1} & a_{-k,r_1} & a^\dagger_{k,r_2} & a_{-k,r_2} \end{pmatrix} \mathcal{H}_k \begin{pmatrix} a_{k,r_1} \\ a^\dagger_{-k,r_1} \\ a_{k,r_2} \\ a^\dagger_{-k,r_2} \end{pmatrix} , \tag{4.1.5}$$

with the matrix $\mathcal{H}_k$ given by

$$\mathcal{H}_k = \frac{-1}{2\sqrt{3}} \begin{pmatrix} 2\sqrt{3} & 0 & -J_x - J_y\bar{\phi} & -J_x - J_y\bar{\phi} \\ 0 & -2\sqrt{3} & J_x + J_y\bar{\phi} & J_x + J_y\bar{\phi} \\ -J_x - J_y\phi & J_x + J_y\phi & 2\sqrt{3} & 0 \\ -J_x - J_y\phi & J_x + J_y\phi & 0 & -2\sqrt{3} \end{pmatrix} ,$$

where $\phi = e^{ika_1}$ is the phase factor coming from the spatial distance between different primitive cells. We can diagonalize $\mathcal{H}_k$ by performing a unitary transformation U onto the fermionic operators. The main benefit of working with fermionic operators comes now into play, as the new basis of operators is again fermionic as can be shown by using the definition of unitary matrices. We obtain a diagonal matrix D of the form $D = U^\dagger \mathcal{H}_k U$, where the eigenvalues of the Hamiltonian are on the diagonal of D. The eigenstates can be determined by applying $U^{(\dagger)}$ on the left or right vector of operators in equation 4.1.5.

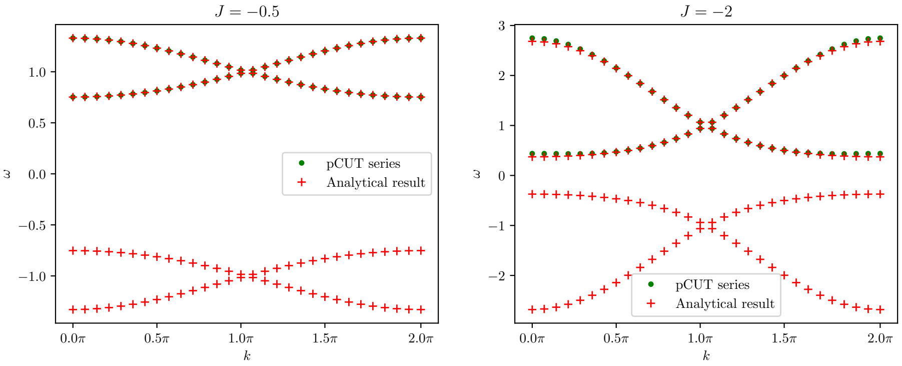

Figure 4.9: Dispersion of the one quasi-particle sector for the Compass model with $J_z = 0$ and a magnetic field h^{001}. The dispersion is plotted for two different values of $J := J_x = J_y$. As we are able to calculate the analytical eigenvalues of the Compass model by diagonalizing $\mathcal{H}_k$, we can compare the analytical results with those calculated with pCUT. For the (physical) bands with $\omega > 0$, the two solutions fit exactly. For the case of very large coupling $J = 2$, we obtain small deviations between the two solutions. For both plots the bare series were used. The minimum of the dispersion is located at vanishing momentum. So, we can again stick to $k = 0$ for the discussion of the band gap.

Discussion Moving on to the discussion of the results, we first take a short look at the dispersion. As we diagonalized a 4×4 matrix, we obtain 4 different eigenvalues, as can be seen in figure 4.9. As we are restricted to one-dimensional chains, the consideration of one direction in momentum space suffices. First, we note that two of the 1QP energies are positive and two are negative. In the fermionic picture the two negative energies correspond to filled bands [53, page 5]. As there is no equivalent to our 'real' physical application with the hardcore bosons, we will stick to the two positive bands. As we can see, the results obtained from the analytical diagonalization and the pCUT calculations match almost perfectly. Only for large coupling values J, we obtain small deviations. This can be expected as J is the perturbative parameter for pCUT and should be small in relation to the magnetic field. The similarity of the Compass model to our previous case with a uniform coupling and a magnetic z-field can be seen in the overall structure of the dispersion in figure 4.9 and the right plot in figure 4.6. In both cases the two (physical) bands start with maximal distance for vanishing k and intersect at $k = \pi$. The minimum of dispersion lies again at $k = 0$. So, for the further discussion of the band gap, we can stick to the $k = 0$ point.

The gap for one quasi-particle is plotted for antiferromagnetic and ferromagnetic couplings in figure 4.10. As for the dispersion, we plotted the bare series (this time with the extrapolations) and the analytical solution. The two results match comparably good, even for very large couplings $|J|$. Again, the extrapolations give a larger range of convergence, as for the given range there are no notable differences to the analytical solution. In contrast to previous investigated gaps, the gap of the Compass model is symmetric with respect to $J = 0$. For the general Kitaev honeycomb model, we argued that the ferromagnetic or antiferromagnetic J_z coupling in z-direction gives a different energy gain or loss, when starting from a fully polarized state and flipping one spin along the z-axis.

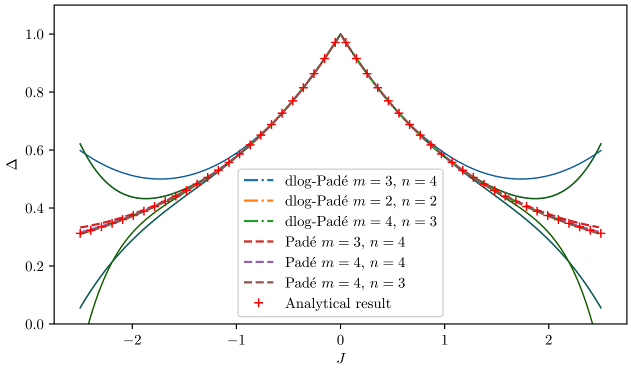

Figure 4.10: One quasi-particle gap for the Compass model with $J_z = 0$, $J := J_x = J_y$, and $h = h^{001}$. The gap is located at vanishing momentum $k = 0$. In contrast to the previous plots, the gap for this Compass model is symmetric with respect to $J = 0$. In addition to the bare series (blue for low order, green for high order) and the Padés and dlog-Padés, the analytical solution is plotted with red crosses. In contrast to all other lines, the analytical solution is no perturbative solution around $J = 0$. The quality of the bare series and the extrapolants is quite good as the absolute coupling $|J|$ ranges to comparably high values. For the investigated couplings we find no evidence of a closing of the gap. It can be shown with the analytical results that the gap does not close for finite J, h.

For the Compass model in a transverse magnetic field, the couplings between the spins only couple in the directions x, y, which are orthogonal to the magnetic field in z-direction. So, the energy change of a spin flip along the z-direction is independent of the sign of J_x, J_y, as can be justified when e.g., investigating the Pauli-matrices. For our general model we learn that we can adjust the ‘tilting’ of the gap with respect to $J = 0$, by changing the J_z contribution in the overall coupling.

In the given parameter range we see no evidence for the closing of the gap. As we have the advantage of an analytical solution, we do not have to rely on the perturbative results. When setting $k = 0$, we can write the four eigenvalues as

$$\begin{aligned} \epsilon_{1,2} &= \frac{1}{2\sqrt{3}}\left[\pm(J_x + J_y) + \sqrt{(J_x + J_y)^2 + 4(2\sqrt{3})^2}\right] \\ \epsilon_{3,4} &= \frac{1}{2\sqrt{3}}\left[\pm(J_x + J_y) - \sqrt{(J_x + J_y)^2 + 4(2\sqrt{3})^2}\right] . \end{aligned} \tag{4.1.6}$$

As we can estimate the root with $\sqrt{(J_x + J_y)^2 + 4} > \sqrt{(J_x + J_y)^2} = J_x + J_y$, we obtain $\epsilon_{1,2} > 0$ and $\epsilon_{3,4} < 0$ for all couplings J_x, J_y. This means that $\epsilon_{3,4}$ correspond to the filled bands and one of $\epsilon_{1,2}$ is the band gap depending on the sign of $J_x + J_y$. As we have strict inequalities, we can state that the band gap does not close for finite couplings J and non-vanishing magnetic fields [53]. So, it occurs a phase transition to the polarized phase for infinitesimal magnetic fields.

Moreover, the eigenenergies in equation 4.1.6 only depend on the sum $J_x + J_y$ of the two couplings. So, when choosing $J_x = -J_y$ we can cancel the effects of the two different bond types to get a constant gap independent of the overall coupling strength $|J_x| + |J_y|$.

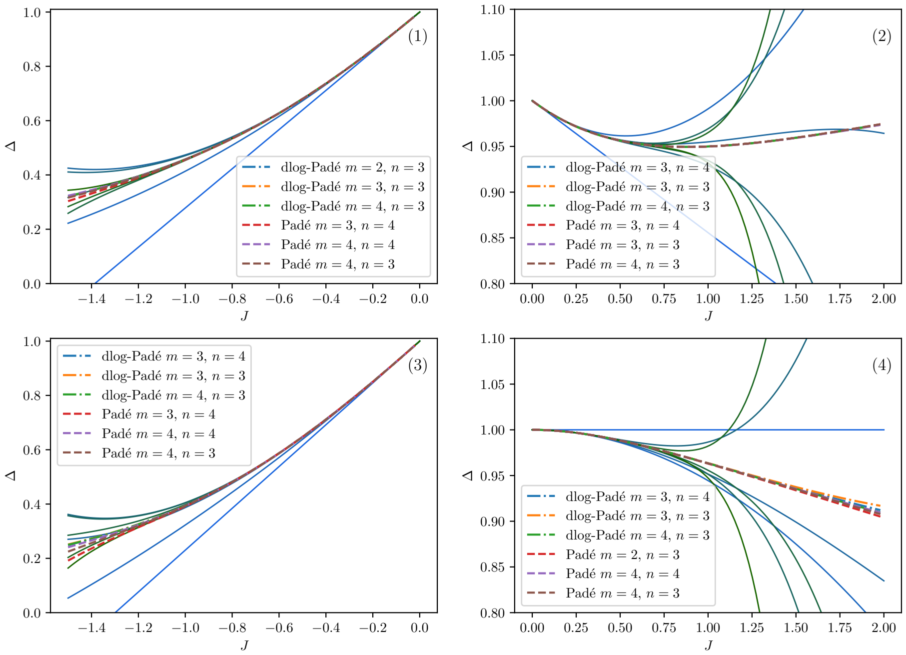

Figure 4.11: One quasi-particle gap for different magnetic fields in the Compass model $J_z = 0, J := J_x = J_y$. For figures 1 and 2 the magnetic field h^{011} and for 3 and 4 the uniform magnetic field h^{111} is chosen. On the left-hand side, the gap is plotted for antiferromagnetic couplings, on the right-hand side for ferromagnetic couplings. The bare series are plotted blue (low maximum order) to green (high maximum order). The Padé and dlog-Padé extrapolants are plotted in various colors with m, n being the degree of the denominator and numerator, respectively. As the magnetic fields are not orthogonal to the couplings between the sites, the symmetry of the gap with respect to $J = 0$ is broken. As for the previous cases, the gap of the antiferromagnetic cases shrinks faster than the ferromagnetic ones. Nonetheless, for all four extrapolations the band gap closes not fast enough to get a reasonable estimate of the gap-closing within the convergence radius.

As we know that the gap does not close for the Compass model with a transversal magnetic field, we will move on to different magnetic fields. For discussion, we will restrict ourselves to the two cases of h^{011} and h^{111} and the one quasi-particle gap. The results are plotted in figure 4.11. In figures 1 and 2 we have plotted the gap for h^{011} and in 3 and 4 the uniform h^{111}. As expected from the above discussion the symmetry of ferromagnetic and antiferromagnetic J is broken as the two magnetic fields are not orthogonal to the interactions anymore. Again, the antiferromagnetic interaction is preferred, as a spin flip lowers the energy of such a state. For the uniform magnetic field in figure 3 the gap seems to shrink faster than for h^{011}. The reason could be the larger portion of the magnetic field pointing in direction x, y of the couplings, as we supposed that this should enlarge the asymmetry of the band gap. This asymmetry trend is only fulfilled partially as for ferromagnetic couplings the qualitative difference between figures 2 and 4 is not very clear. For both antiferromagnetic cases we are not able to calculate a reliable gap closing point as we have only one root for figure 1 and three roots spread over a very large coupling range in figure 3. Nonetheless, the results seem to indicate a phase transition for large couplings.

It would be interesting to investigate these cases with the non-transversal component of the magnetic field as perturbation to the transversal Compass model we solved analytically in this section. As we are only interested in the Compass model as a limiting case of our general model, we will leave the discussion of the Compass model for general magnetic fields at this point.

4.1.2 Spectral quantities

After investigating the dispersion of our system for various parameter configurations, the following section will take a look at the spectral properties of our system. For this section (and also for the one in the two quasi-particle sector), we will focus on the discussion of a single observable operator. We choose our observable to only act on the z-component of a single spin i:

$$O(i) := \sigma_i^z \, . \tag{4.1.7}$$

As discussed in section 3.2.4, we first have to transform O to match with our rotated system, where the magnetic field points along the z-axis. We obtain

$$\begin{aligned} \mathcal{O}(i) = U^\dagger O(i) U &= \frac{1}{h}\left(h_z\sigma_i^z - \sqrt{h_x^2 + h_y^2}\sigma_i^x\right) & (4.1.8)\\ &= \frac{1}{h}\left(h_z(1 - 2b_i^\dagger b_i) - \sqrt{h_x^2 + h_y^2}(b_i^\dagger + b_i)\right) \, , & (4.1.9)\end{aligned}$$

with $h = \sqrt{h_x^2 + h_y^2 + h_z^2}$ and the application of the Matsubara-Matsuda transformation. For a magnetic field pointing in z-direction, the observable only 'measures' the orientation of spin i, but does not flip spins. If the magnetic field is rotated, $\mathcal{O}$ also features spin flips, so quasi-particles are created or annihilated at position i. To investigate the observable in the same basis as the particle conserving Hamiltonian H_{eff}, we have to apply the same pCUT to $\mathcal{O}$. Following section 3.2.4, we obtain the effective observable $\mathcal{O}_{\text{eff}}$.

Furthermore, we restrict the discussion to the limit of zero temperature $T = 0$. Physically this means that our system has no thermal excitations. So, it suffices to investigate excitations added by the observable only acting on the ground state $|0\rangle$. This simplifies the treatment of the effective observable as we only have to take care of the resulting states, as the 'start state' is always the ground state. For more information on the basic concept see section 3.2.4.

4.1.2.1 Spectral weight

Before starting with the spectral quantities specific for 1QP, we first investigate the overall spectral weight I_{tot} of the observable O. We can subdivide I_{tot} into the different quasi-particle channels, as defined in equation 3.2.19. Using this decomposition, we can measure with which relative probability we obtain a state with a certain number of quasi-particles, when applying the observable onto the ground state, as given in equation 3.2.18 with

$$I_n = \langle 0 \mid \mathcal{O}_{n,0}^\dagger \mathcal{O}_{n,0} \mid 0\rangle = \sum_{i_1,\ldots,i_n} \mid \langle n, i_1, \ldots, i_n \mid \mathcal{O}_{N,0} \mid 0\rangle \mid^2 \, .$$

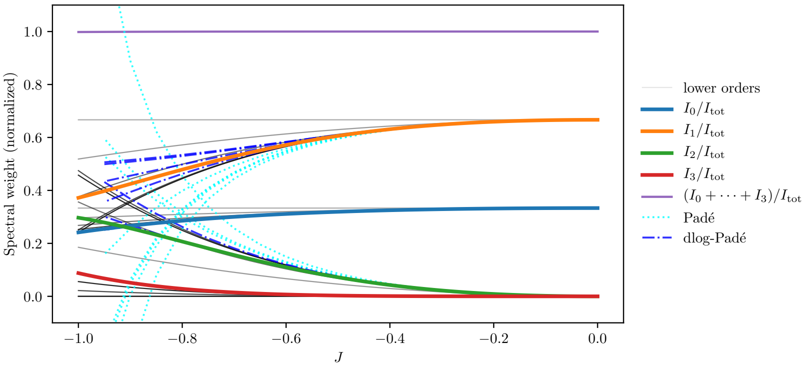

Figure 4.12: Spectral weights for varying antiferromagnetic couplings $J = J_x = J_y = J_z < 0$ up to order 6. The weights are decomposed into the different quasi-particle channels and are normalized with the total weight I_{tot}. In purple the sum of all relative weights is plotted, being close to the constant 1. So, the quasi-particle channels up to three, are the only noteworthy contributions to the overall weight. For the bare series, the Padés and dlog-Padés are plotted in dashed lines. As a further indicator of quality, the lower orders of the different series are plotted in light grey.

The results are shown in figure 4.12. The weights are plotted with respect to varying antiferromagnetic couplings J. The maximum order series of the different weights is plotted in colors, while the lower orders are plotted for a guide of quality in light grey. Furthermore, the Padé and dlog-Padé approximants are plotted in dashed lines. The quality of the different series seems to be good up to a coupling of $J \approx -0.55$, when the different orders and extrapolants begin to diverge. Later in section 4.2.2, we will dive into the explanation of this loss in quality. As a further quality check, the sum of all QP intensities I_n is plotted in purple. As we use normalized weights, the sum over all QP-channels should give exactly the constant function 1. Adding up the intensities I_0 to I_3, we obtain

$$\sum_{i=0}^{3} \frac{I_i}{I_{\text{tot}}} = 1.0 - 0.00185 J^6 \,,$$

where we calculated all weights up to order 6. This means that there is no further relevant distribution in higher QP-channels to the overall spectral weight up to order 6. This makes sense as the first possible 4QP contribution starts in sixth order. Looking closer at the single QP-weights, we have the relative weights

$$\begin{aligned}
I_0/I_{\text{tot}} &= 0.33333 - 0.03704J^2 + 0.02851J^3 - 0.01509J^4 \\
&\quad + 0.00698J^5 - 0.00419J^6 \\
I_1/I_{\text{tot}} &= 0.66667 - 0.14815J^2 + 0.14256J^3 - 0.12529J^4 \\
&\quad + 0.00967J^5 + 0.13106J^6 \\
I_2/I_{\text{tot}} &= 0.18519J^2 - 0.17107J^3 + 0.11843J^4 + 0.01713J^5 - 0.16071J^6 \\
I_3/I_{\text{tot}} &= 0.02195J^4 - 0.03378J^5 + 0.03199J^6 \,.
\end{aligned}$$

The weights for zero and one quasi-particles have a non-vanishing constant contribution. This matches with equation 4.1.9, as in zeroth order in the series

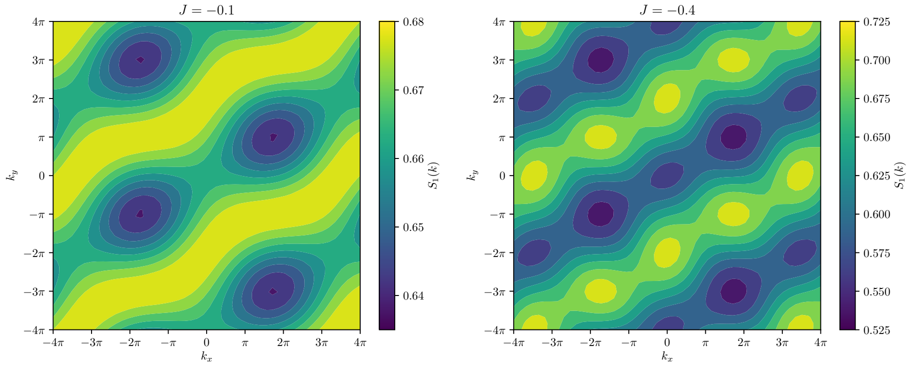

Figure 4.13: Static structure factor of $\mathcal{O}$ as given in equation 4.1.9 for a uniform magnetic field $h = 1$ and two different antiferromagnetic uniform couplings $J \in \{-0.1, -0.4\}$. Note that we do not use the b_1, b_2 basis for describing the momentum but decompose the momentum in the x- and y-component in real space. The spectral density is given in the same units as the spectral weights.

of pCUT only the original observable $\mathcal{O}$ contributes. For $h = 1$, we can calculate the action of $\mathcal{O}$ on the ground state as

$$\mathcal{O}(i)\,|0\rangle = \frac{1}{\sqrt{3}}\left(|0\rangle - \sqrt{2}\,|1, i\rangle\right), \tag{4.1.10}$$

which results in the intensities $I_0 = 1/3$ and $I_1 = 2/3$ for order zero matching with the calculated series. For higher order, we also obtain higher QP-channels. As the weight is a 'squared quantity', only every second order a new higher QP-channel starts, as can be seen for 2QP starting at order 2 and 3QP starting at order 4. Thus, the statement only investigating spectral quantities in low quasi-particle channels or even only 1QP, is proven to be valid, as long as the perturbation is small. Nonetheless, as we see in the figure, it does not suffice to only investigate 1QP in the given parameter range, as I_2 is of the same magnitude as I_0 for large perturbations. This finding is important for justifying the investigation of the two quasi-particle channel later on, as the spectral weight indicates the fraction of physical processes which lie within the different QP-channels.

4.1.2.2 Static structure factor

After discussing the spectral weight of the observable $\mathcal{O}$, for the rest of this section we will stick to the one quasi-particle channel. As we have gained information of the overall contribution of 1QP to the action of $\mathcal{O}$ to the ground state—which is the dominant channel, as can be seen in figure 4.12—we now want to investigate the properties of $\mathcal{O}$ in 1QP more closely. First, we can look at the static structure factor, which gives us the spectral density resolved in momentum k. As the spectral weight gives us information about the distribution of the number of quasi-particles in the states generated by $\mathcal{O}$, the static structure factor adds information about the momentum of the generated quasi-particles.

Again we will concentrate on the most common case of a uniform magnetic field

$h = 1$ and a uniform coupling J. In figure 4.13 the static structure factor of $\mathcal{O}$ is given for the two couplings $J = -0.1$ and $J = -0.4$. First, we can investigate $S_1(k)$ for vanishing couplings. We obtain

$$S_1(k)|_{J=0} = \frac{2}{3}$$

which matches perfectly with the spectral weight I_1, we obtained in figure 4.12 and in the corresponding discussion. For a vanishing coupling the spectral density does not depend on the momentum, as the hopping of quasi-particles is only induced by the Kitaev couplings. Having the trend of decreasing I_1 for larger J in mind, the overall results seem to fit into that picture, as the starting mean of the static structure factor decreases for the figure of the larger coupling. As a new information we obtain that the range of intensities grows for larger couplings. Again, the reason is found in the larger contribution of processes which move quasi-particles over the lattice.

Next, even as the details of the two figures differ, we can observe an overall trend of a constant density along lines of a characteristic tilt. To have a more concrete imagination in real space, we have changed the basis of the overall momentum from the dual basis to the x- and y-component of the momentum in real space. As an (arbitrary) normalization we have chosen the momentum vector $\vec{k}$ as

$$\vec{k} = \frac{1}{\sqrt{12}} \begin{pmatrix} k_x \\ k_y \end{pmatrix} = \frac{1}{\sqrt{12}} (k_x e_x + k_y e_y) \,, \tag{4.1.11}$$

where e_x, e_y are the unit vectors in x- and y-direction in real space. The normalization constant is chosen in such a way that $a_i \cdot a_i / \sqrt{12} = 1$ for $i \in \{1, 2\}$, where the a_i are the lattice vectors as chosen at the beginning of section 3.1. When analyzing the directions of the constant density lines, we find the direction to be parallel to a_1. This specific direction is induced by the choice of the original observable $O = \sigma^z$. As the action of O is parallel to the Kitaev couplings at the z-bonds, this seems to mark this direction in contrast to the two other orthogonal spin couplings. When looking closer at the differences of the two figures, more structure along these lines appears when increasing the coupling. For different values of J, this 'microscopic' structure keeps changing, but the overall trend of lines along a_1 stays the same. It would be interesting to investigate additional observables, to check how these 'lines of constant intensity' change in orientation for different directions of spin-observables.

To show the diversity of the k-resolved structure for different parameters, we have plotted the static structure factor for ferromagnetic couplings $J > 0$, keeping all other variables as they were, in figure 4.14. In comparison to the antiferromagnetic case, the overall weights seem to be shifted slightly to higher intensities and the range of intensities is a bit narrower. Both can be explained by the slower change of the overall weight for increasing ferromagnetic couplings. As before, we obtain a 'macroscopic' structure of lines pointing in a_1 direction. In contrast to the antiferromagnetic case, the lines of higher intensities first start to get a defined structure, while the other lines have a very narrow band of intensities. This fits to the swapping of band intensities, meaning the lines of low intensity for $J < 0$ are the lines of high intensity for $J > 0$ and vice versa.

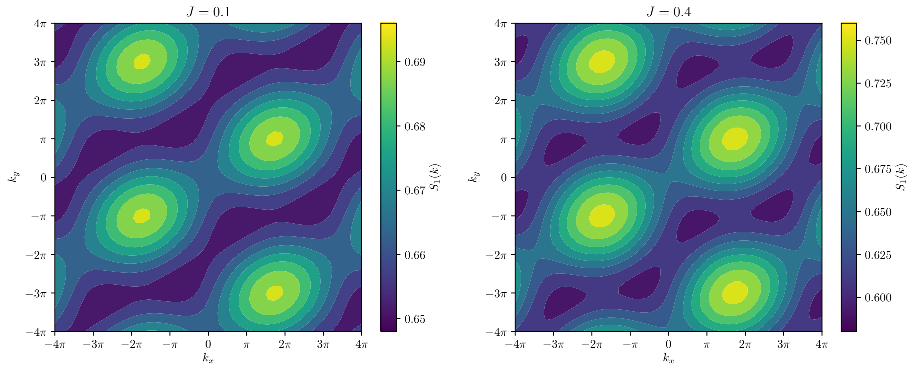

Figure 4.14: Static structure factor of $\mathcal{O}$ as given in equation 4.1.9 for a uniform magnetic field $h = 1$ and two different ferromagnetic uniform couplings $J \in \{0.1, 0.4\}$. Note that we do not use the b_1, b_2 basis for describing the momentum but decompose the momentum in the x- and y-component in real space. The spectral density is given in the same units as the spectral weights.

Investigating the 'microscopic structure', the structure seems to be similar but inverted in relative intensities when comparing the two plots with $|J| = 0.1$. When going to the higher intensities the structures start to have larger differences. Again, the lines of low intensity for $J = 0.4$, can be related to the lines of high intensity for $J = -0.4$. But the lines of high intensity stay roughly the same for increased couplings, while for the antiferromagnetic case, the structure gets an additional local minimum at $k = 0$ and the periodic continuations.

Summarizing, we can understand or at least motivate most of the features we obtain for the two discussed parameter values. Nonetheless, a more concrete understanding of the dependency of the observable O and the resulting lines and structure, would be interesting. When swapping the sign of the Kitaev interaction, we mostly get an inversion of the relative intensities, which fits for most of the structure. But also for this aspect it would be interesting to have a closer look at the different processes for the two cases.

4.1.2.3 Dynamical structure factor

As last part of the 1QP discussion, we investigate the dynamical structure factor as defined at the end of section 3.2.4. The dynamical structure factor goes one step further as the static structure factor, as it splits the overall intensity for a given momentum into the energy spectrum. For the case of the 1QP channel, we have shown at the beginning of this section that we have two eigenstates for given momentum, as can be seen e.g., in figure 4.1. Effectively, we combine the already gained information about the energy spectrum and the spectral density at fixed momenta to calculate the dynamical structure factor. For calculation we use equation 3.2.22, given as

$$S_1(k, \omega) = \langle 0 \mid \mathcal{O}^\dagger_{1,0} \delta(\omega - H_1) \mathcal{O}_{1,0} \mid 0 \rangle \ ,$$

and first determine the eigenenergies ϵ_1, ϵ_2 and corresponding eigenstates v_1, v_2 of the effective Hamiltonian H_{eff} in the 1QP sector. Keep in mind that all quan-

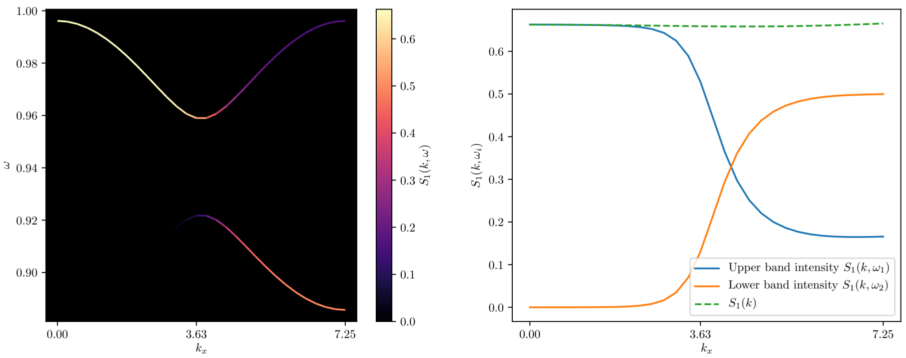

Figure 4.15: Dynamical structure factor for a uniform magnetic field $h = 1$ and a uniform coupling $J = -0.1$. The spectral density is plotted for a path along the x-direction of momenta, setting $k_y = 0$ and varying k_x. The units correspond to the one introduced in section 4.1.2.2. On the left side the dispersion of the energy is plotted along the given k-path. The spectral density for the corresponding band is given in color code. For a more accurate visualization of the spectral density, it is plotted on the right side. Additionally, the sum of both densities for fixed momentum is plotted as a dotted line, being the static structure factor $S_1(k)$.

tities ϵ_i, v_i are given in form of series expansions as the effective Hamiltonian is given as a series. So, when calculating the eigenstates, the series v_1, v_2 have to fulfill

$$H_{\text{eff}} v_i - \epsilon_i v_i = 0\,, \quad \bar{v}_i v_j = \delta_{ij}$$

for $i, j \in \{1, 2\}$, where 0 and δ_{ij} are constant series, with vanishing higher orders. The eigenenergies and eigenstates are calculated order by order, solving the above equations for each order separately. We obtain $S_1(k, \epsilon_i)$ of band i by calculating the squared scalar product

$$S_1(k, \epsilon_i) = |\,\langle v_i \mid \mathcal{O}_{1,0} \mid 0 \rangle\,|^2$$

between the corresponding eigenstate and the resulting state after application of the observable $\mathcal{O}_{1,0}$.

The result of such a calculation is shown in figure 4.15, where we have chosen a small uniform antiferromagnetic coupling $J = -0.1$ and a uniform magnetic field $h = 1$. On the left the 1QP dispersion is plotted along the y-axis and the spectral density for the corresponding band is plotted in color code. On the right side the spectral density for the two bands is plotted along the y-axis to give a more detailed insight of the concrete density values. For the path in momentum space we only vary the x-component of the momentum and fix $k_y = 0$. When performing a basis change in momentum space to the dual basis b_1, b_2, we obtain $k = k_x e_x \approx 7.25 e_x$ corresponding to $k_1 = k_2 = 2\pi$. So, when comparing it to the dispersion in figure 4.1, we cut diagonally through the 2D plane, starting at $k = 0$ and ending at $k_1 = k_2 = 2\pi$. This corresponds to one period in the dispersion. For the spectral density, we can compare the result to figure 4.13, starting at $k = 0$ and going horizontally to $k_x \approx 7.25$.

First, taking a short look at the energy bands, the two bands are well separated with a maximum distance for vanishing momentum. For a small coupling J, the two bands are symmetric to each other. Next, comparing the results to the static structure factor, we obtain an almost constant total spectral density for the chosen path in k-space, as plotted with the dashed line in the right figure. The small increase in the overall spectral density corresponds to the starting transition into the neighbored 'high intensity line', as plotted and discussed in figure 4.13. The value of total intensity of around $S_1(k) \approx 2/3$ also matches with the previous discussion of the spectral weight.

Getting to the distribution of the spectral density of the two bands, we most prominently find a vanishing density for the lower band at small momenta. The entire intensity is concentrated on the upper band. Only when moving to higher momenta (around the edge of the first Brillouin zone at $k_1 = k_2 = \pi$) we obtain a switch of intensity to the lower band, but a portion of around 1/3 remains in the upper band. As the lower band vanishes identically for all calculated orders, we will investigate the distribution for $k = 0$ in more depth. For that we will restrict ourselves to order 1, to keep the calculations simple.

To show the vanishing contribution in zeroth order, it suffices to look at the 1QP channel of the effective observable in zeroth order given as

$$\mathcal{O}_{1,0} \left|0\right\rangle = -\frac{1}{\sqrt{6}}(\left|1,k;r_1\right\rangle + \left|1,k;r_2\right\rangle)\,, \tag{4.1.12}$$

where we used equation 4.1.10 and applied the global observable instead of the local one. When we look at the effective Hamiltonian of zeroth and first order, we can use equation 4.1.1 of the hoppings in first order to get a Hamiltonian of the form

$$H_{\text{eff}} \begin{pmatrix} \left|1,k;r_1\right\rangle \\ \left|1,k;r_2\right\rangle \end{pmatrix} = \left(\begin{pmatrix} 1 & 0 \\ 0 & 1 \end{pmatrix} + \frac{1}{\sqrt{3}} \begin{pmatrix} 1 & -1 \\ -1 & 1 \end{pmatrix} J + \mathcal{O}(2) \right) \begin{pmatrix} \left|1,k;r_1\right\rangle \\ \left|1,k;r_2\right\rangle \end{pmatrix}\,,$$

where the first matrix describes the zeroth order magnetic field contribution and the second matrix is the first perturbative contribution with the on-site hopping on the diagonal and the hopping to the neighbored sites on the off-diagonal. Do not confuse the higher orders $\mathcal{O}(2)$ with the observable, as they both share the same character. The eigenvalues ϵ_i and eigenstates v_i are given as

$$\epsilon_1 = 1,\; v_1 = \left|1,k;r_1\right\rangle + \left|1,k;r_2\right\rangle\,, \quad \epsilon_2 = 1 + \frac{2}{\sqrt{3}}J,\; v_2 = \left|1,k;r_1\right\rangle - \left|1,k;r_2\right\rangle\,, \tag{4.1.13}$$

what matches with the two series in equation 4.1.2. By comparing the state of equation 4.1.12 to the two eigenstates v_1, v_2, we see that the scalar product between the observable state and v_2 vanishes, which corresponds to the state of lower energy for $J < 0$. So, we can identify the effect of the vanishing intensity mainly with the different signs between the local hopping and the other neighboring hoppings, as those define the two eigenvectors in a symmetric and antisymmetric form, respectively. For the explanation of the vanishing in the higher orders, the uniform character of the magnetic field and coupling is the key as the hoppings in the different directions are symmetric also in higher orders, as can be seen in appendix B. When applying a finite momentum, this symmetry breaks, as the phases of the hoppings start to depend on the direction. Nonetheless, it would be interesting to understand the strong protection also for rising momenta.

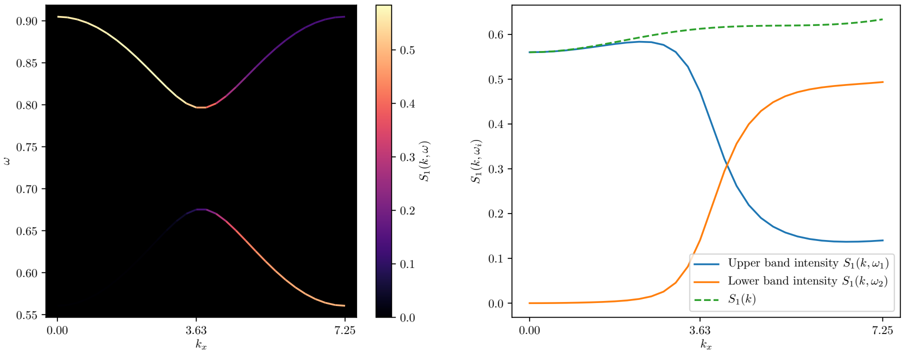

Figure 4.16: Dynamical structure factor for a uniform magnetic field $h = 1$ and a uniform coupling $J = -0.4$. The spectral density is plotted for a path along the x-direction of momenta, setting $k_y = 0$ and varying k_x. The units correspond to the one introduced in section 4.1.2.2. On the left side the dispersion of the energy is plotted along the given k-path. The spectral density for the corresponding band is given in color code. For a more accurate visualization of the spectral density, it is plotted on the right side. Additionally, the sum of both densities for fixed momentum is plotted as a dotted line, being the static structure factor $S_1(k)$.

When increasing the coupling J, the dynamical structure factor does not change qualitatively, as can be seen in figure 4.16. The symmetry of the two bands remains conserved with the maximum width at vanishing momentum. Simultaneously, the overall band structure moves to smaller energies, as we already saw in the discussion of the band gap. The overall intensity $S_1(k)$ shrinks slightly, as can be seen in the decreased 1QP weight I_1 and the static structure factor in figure 4.13. The distribution of $S_1(k)$ on the two bands stays roughly the same. Again, for small k values, the spectral density vanishes for the lower band, as discussed above. A qualitative change is the moving of the maximum in intensity for the upper band to finite momenta. This effect gets even stronger when increasing the coupling J further. Later on we will also look at larger couplings to compare the results to DMRG data in section 4.3, but we will have to deal with a loss of accuracy as we already have seen in the extrapolations of several gaps in the previous sections.

Summarizing the discussion of the one quasi-particle subspace, we analyzed the energy-spectrum for different magnetic fields and Kitaev couplings, including the limiting case of the one-dimensional Compass model. In the second half, we analyzed the spectral quantities of an observable $O = \sigma_i^z$, going step by step into more details, resolving first the QP number, followed by the momentum and the energy. For all parts we mainly concentrated on a uniform magnetic field and antiferromagnetic couplings, as this parameter choice is common for the discussion of this model. With exception of the Compass model, we have no full analytical results available and have to rely on the perturbative calculations done with pCUT. By comparing the two approaches in the Compass model, we obtained quite good agreements, of the analytical and the perturbative results. Also the quality of the bare series and the extrapolations give a good indicator of the quality of the series expansion for the respective coupling strength. Even as the quality was quite good for small couplings, the convergence radius was not large enough to investigate the phase transitions out of the polarized phase for most of the chosen parameters with high enough precision.

4.2 Two-particle sector

After we have examined the one quasi-particle subspace, in the following section we will concentrate on the two quasi-particle subspace. As already mentioned, the sole consideration of only the 1QP channel often suffices to describe the gap of the energy spectrum and track the potential phase transition point in parameter space. We will see during the following discussion that indeed the two quasi-particle sector does not give crucial new information to these topics, as the 2QP energy normally lies above the 1QP states and does not vanish earlier than the 1QP gap. Nonetheless, investigating two quasi-particles gives additional information about the corresponding phase (in our case the polarized phase) as we can track the interaction between the two quasi-particles. As for the classical case, we can examine whether the particles attract or repel each other by examining the energy of the 2QP states. Furthermore, we get additional information about spectral properties, as we can analyse the spectral density of the 2QP states. These insights are directly relevant for spectroscopic experiments, thus being a link between the theoretical investigation and experiments with potential realizations of the model.

For the calculation of the 2QP quantities, we have to calculate H_1 and H_2 from the decomposition of the effective Hamiltonian in equation 3.2.7. As we have already calculated H_1 for the 1QP discussion, we are left with the calculation of H_2, which includes all correlated two quasi-particle processes. We combine the obtained results into the distance matrix M_{dist} as visualized in figure 3.6 and diagonalize M_{dist} to obtain the 2QP spectrum. We calculate H_2 following equation 3.2.13. As the number of coefficients for H_2 is roughly the quadratic from H_1, as we have to vary the position of two quasi-particles instead of one, we only were able to calculate H_2 up to order 7 for arbitrary J_x, J_y, J_z in reasonable time. For the spectral quantities we have to calculate $\mathcal{O}_{2,0}$, following equation 3.2.16, which we calculated up to order 6.

4.2.1 Dispersion and gap

When evaluating the eigenvalues in the 2QP subspace, we can not calculate them in the thermodynamic limit, as done in the 1QP case. The reason, as outlined in section 3.1, lies in the additional relative distance coordinate d of the 2QP states in momentum space $|2, k, d\rangle$. As for the one quasi-particle case, we can utilize the total momentum conservation, resulting in no interaction terms between states of different total momentum. However, as the relative distance is not conserved, we only can calculate the dispersion for distances up to a certain threshold, as visualized in figure 3.6. For more information about the concrete calculations see section 3.2.3.

We will discuss the 2QP dispersion and gap in two main steps. First, we will ignore the interactions between the two quasi-particles, effectively setting $H_2 = 0$. For this case we can use the free particle approximation, which was introduced in section 3.3, to calculate the 2QP dispersion without new pCUT calculations. Nonetheless, we will also calculate the dispersion by diagonalizing the ‘distance matrix’ in figure 3.6 to compare the two results with each other. Next, we will add the H_2 component containing the interactions between the quasi-particles which results in bound or anti-bound states (depending on the sign of J) for strong enough Kitaev-couplings. Comparing the two cases, we can identify the effects of the interactions in the dispersion and the resulting gap.

4.2.1.1 Without quasi-particle interaction

As outlined, we will start the 2QP discussion neglecting the interaction between the quasi-particles. Therefore, we set $H_2 = 0$. We are left with the one quasi-particle terms H_1, we already used for the 1QP dispersion. Effectively, we have to compute matrix elements of the form

$$\langle 2, k; \tilde{\delta}; \tilde{r}_1, \tilde{r}_2 \mid H_1 \mid 2, k; \delta; r_1, r_2 \rangle \ ,$$

where k is the total momentum of the two quasi-particles, $\delta, \tilde{\delta}$ are the distances between the two particles, and $r_i, \tilde{r}_i$ are the positions of the respective particles within the primitive cell. For more information, see the definition of the states in momentum space in section 3.1. As we ignore the interactions for the moment, we are left with the task of diagonalizing the 'distance matrix' M_{dist} visualized in figure 3.6, defining a maximum distance $\delta_{\max}$ between the two quasi-particles to keep the dimensionality finite. Being more precise, $\delta_{\max}$ denotes the number of bonds needed for the shortest path between the two quasi-particles for a 2QP state to be taken into consideration for the distance matrix. For computation, we set $\delta_{\max}$ in the range of 20 to 30. In the further discussion, we will denote the eigenvalues of M_{dist} as $\epsilon_i^{2\text{QP}}$, where i is the index of the corresponding eigenvalue.

Additionally, when neglecting the interaction, we can use the free particle approximation, as introduced in section 3.3. Due to the definition of the Hamiltonian in equation 3.3.1, the two results should be the same. Concretely, we will use the free particle approximation to determine the edges of the 2QP continuum. Therefore, we calculate the extrema of the set in equation 3.3.2 as

$$\begin{aligned} \omega_{\text{l}}^{ij}(k) &= \min_q \left(\epsilon_i(k/2+q) + \epsilon_j(k/2-q)\right) \\ \omega_{\text{u}}^{ij}(k) &= \max_q \left(\epsilon_i(k/2+q) + \epsilon_j(k/2-q)\right) \ , \end{aligned} \tag{4.2.1}$$

where ϵ_1, ϵ_2 are the energies of the two bands in 1QP, and k is the total momentum. As we have two bands in the 1QP sector, we will obtain three continua in 2QP, as we have three combinations of i, j to choose from.

We start with our standard set of parameters, having a uniform magnetic field $h = 1$ and uniform antiferromagnetic couplings $J < 0$. As the 2QP spectrum consists of a continuum of energies, it is not feasible to plot the dispersion for the complete Brillouin zone in 2D. Instead, we choose a path in momentum space by only varying the x-component of the momentum. This is equivalent to setting $k_1 = k_2$. We choose the range of momenta to catch one period of the dispersion. The results are plotted in figure 4.17 on the left hand side, choosing the parameters $J = -0.1, h = 1$. The eigenvalues of the distance matrix M_{dist} are plotted in light blue lines. The number of lines corresponds to the size of M_{dist}. So, when going to the thermodynamic limit $\delta_{\max} \to \infty$, we will obtain a

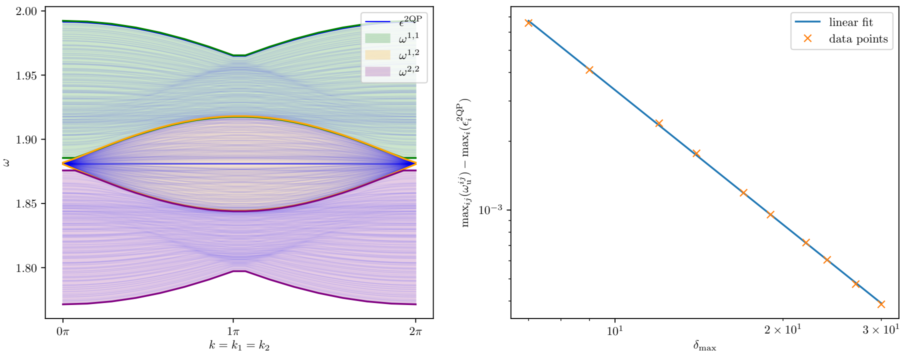

Figure 4.17: On the left side the dispersion of 2QP for $J = -0.1$, $h = 1$ and $H_2 = 0$ is plotted. The momentum is varied in the x-component in the range of one period, by setting $k_1 = k_2$. The 2QP continuum is calculated by using the free particle approximation and diagonalizing the distance matrix M_{dist}. The maxima and minima of the different combinations i, j in equation 4.2.1 are plotted in different colors. The eigenvalues of M_{dist} are plotted in light blue lines. On the right figure the difference between the two methods is plotted by comparing the maximum value for vanishing momentum, while the maximum distance $\delta_{\max}$ for M_{dist} is varied.

continuous spectrum. The different extrema of the free particle approximation in equation 4.2.1, are plotted in different colors. In this case, $\omega^{1,1}$ corresponds to the 2QP continuum formed by two quasi-particles from the upper 1QP band, thus having the highest total energies. Analogously, $\omega^{2,2}$ is formed out of two quasi-particles of the lower 1QP band, and $\omega^{1,2}$ takes one quasi-particle of both bands. In theory, these different continua could have gaps between them which is not the case for the chosen parameter set.

When comparing the results of the two approaches, they seem to fit to quite good accuracy. To check this quantitatively, we investigate the upper edge of the highest continuum in the free particle approximation and the largest eigenvalue of M_{dist} for vanishing momentum $k = 0$. For a perfect matching these two values should be the same. On the right-hand side we have plotted the difference between the two values, while we vary the size of M_{dist} by adjusting the maximum distance $\delta_{\max}$. As expected, the difference decreases when going to higher $\delta_{\max}$ because we go towards the thermodynamic limit while the free particle approximation uses the 1QP solutions, which have been already calculated in the thermodynamic limit. Note that the figure is plotted in a logarithmic scale, so the difference vanishes exponentially. As the difference behaves quite predictable, as can be seen by the performed fit, we can choose $\delta_{\max}$ according to the desired quality of the dispersion. We could also extrapolate the energy of the highest and lowest state for varying $\delta_{\max}$, to estimate the energy in the thermodynamic limit. In the following, we will use $\delta_{\max} \approx 20$ as it suffices for the further discussion. As already seen in the one quasi-particle discussion, when increasing the Kitaev coupling the errors of the bare series and the extrapolations can be of orders higher than the error we get for finite $\delta_{\max}$.

Getting to the result for itself, we obtain a 2QP continuum starting right below an energy of 2, being the energy of a two-particle state with respect to the unperturbed Hamiltonian. As discussed in detail for 1QP in section 4.1, for

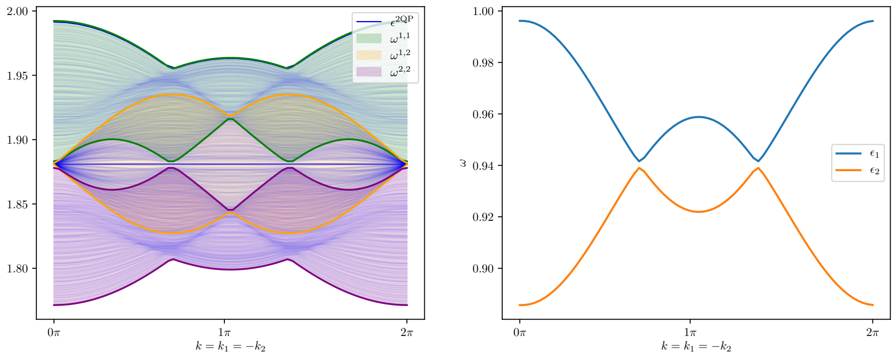

Figure 4.18: On the left side the dispersion of 2QP for $J = -0.1$, $h = 1$ and $H_2 = 0$ is plotted. The momentum is varied in the y-component in the range of one period, by setting $k_1 = -k_2$. The 2QP continuum is calculated by using the free particle approximation and diagonalizing the distance matrix M_{dist}. The maxima and minima of the different combinations i, j in equation 4.2.1 are plotted in different colors. The eigenvalues of M_{dist} are plotted in light blue lines. On the right figure the 1QP spectrum is shown. The two bands touch each other along the chosen path of varying k_y at $k \in \{2\pi/3, 4\pi/3\}$. The bands ϵ_1, ϵ_2 were chosen to have the higher/lower energy for the given momentum, respectively.

antiferromagnetic J the couplings decrease the energy of the 2QP states. The extrema of energy lie at $k = 0$ as for the 1QP subspace. This can be understood with equation 3.3.2, as the two quasi-particle states with vanishing momentum can choose $q = 0$ to get the state of maximum (or minimum) 1QP energy $\epsilon_i(0)$. For the chosen small coupling, the 1QP and 2QP energies lie far away from each other. In section 4.2.2, we will look at larger couplings, which shrink the gap between the 2QP continuum and the upper 1QP band. When establishing an overlap of the two, we will run into problems, as we assumed in the prerequisites of pCUT that the different quasi-particle channels are well separated.

To additionally investigate another path in k-space, we choose the orthogonal path to the first one, only varying the y-component of the momentum. This can be expressed in the dual basis as $k := k_1 = -k_2$. Again, we choose $k \in [0, 2\pi]$ to obtain one period of the spectrum along this direction. All other parameters are chosen as for figure 4.17. The result is shown in figure 4.18. Comparing the two solutions ϵ^{2QP} and $\omega^{i,j}$, we again see a nearly perfect matching of the upper and lower edges, as expected. As we have already investigated the difference between the two solutions, we plotted the 1QP dispersion along the chosen path in k-space on the right-hand side. The 1QP dispersion features an intersection of the two bands, as shortly noted in the 1QP discussion, too. As we obtained the eigenvalues by diagonalization, we chose to order the results due to their magnitude, having one band always above the other. These intersections lead to a more complex structure in the two quasi-particle continuum, as can be seen in the left figure. From the resulting continua $\omega^{i,j}$, we can conclude that also for this direction the different 2QP continua overlap.

Summarizing, we obtain a good agreement of our two approaches to calculate the two quasi-particle continua. The quality of the eigenvalues obtained by the distance matrix M_{dist} get better for larger included distances, thus increasing the size of M_{dist} and time needed for diagonalization. For both investigated cases the three continua in 2QP have no gap to each other, forming one large continuum. Nonetheless, as we can rely fully on the results of the one quasi-particle case, the previous investigation of the 2QP spectrum does not offer new insights in the properties of our model.

4.2.1.2 Full model

After investigating the limiting case of non-interacting quasi-particles by setting the interaction term $H_2 = 0$, we will now add the H_2 term. As discussed in section 3.3, for interacting quasi-particles the free particle approximation does no longer hold. Nonetheless, we will plot the approximation to keep track of the changes in the continuum.

As for the non-interacting case, we fill the distance matrix M_{dist} with the one quasi-particle processes H_1 but add also the H_2 terms, as visualized in figure 3.6. As the H_2 terms potentially move both quasi-particles, we can only include H_2 for those distances where the two quasi-particles can interact virtually. As we have only nearest neighbor interactions in equation 2.3.6, the maximum distance is given by the highest calculated order of H_{eff} in equation 3.2.6. Thus, we can track the coupling of quasi-particles with up to seven bonds distance in the following discussion. Keep in mind that the couplings over such large distances δ will be quite marginal for small Kitaev couplings J, as the two-particle coupling is proportional to $J^{|\delta|}$.

Before we investigate the results, we will shortly think about the expected effects of the two quasi-particle interactions. As we have no long-range interactions in our Hamiltonian, we can stick to couplings in $\mathcal{H}$ which are all next neighbor processes. As we have defined $\mathcal{H}$ in equations 2.3.5 and 2.3.6, we have to take a look at the processes acting on two neighbored sites. Examining t_0^α for a uniform magnetic field we have

$$t_0^\alpha(i,j) = J_\alpha C \left[(1 - 2n_j - 2n_i + 4n_i n_j) + 2(b_i^\dagger b_j + b_i b_j^\dagger)\right] =: t_\text{l} + t_\text{h}$$

with $C := -\frac{1}{6\sqrt{3}}$. Ignoring the hopping-term t_h, which induces the quasi-particles in a state to hop to adjacent sites, we are left with counting operators t_l. When comparing the action of these operators on the states $|1,i\rangle, |2,i,j\rangle$ we obtain

$$t_\text{l}\,|1,i\rangle = -J_\alpha C\,|1,i\rangle\ , \quad t_\text{l}\,|2,i,j\rangle = J_\alpha C\,|2,i,j\rangle\ .$$

The two resulting coefficients differ by a minus sign. So, if the energy was lowered by the local term for a one quasi-particle state $|1,i\rangle$, it will be raised when having a two quasi-particle state $|2,i,j\rangle$ with the particles being nearest neighbors. As we discussed in section 4.1 that the local hopping leads to a lowering in energy for antiferromagnetic Kitaev couplings, we assume a shift upwards, when two quasi-particles are next to each other. This can also be explained directly by the Kitaev couplings, as done for the 1QP case. As the quasi-particles correspond to a flip of the spin opposite to the direction of the magnetic field, for antiferromagnetic couplings the quasi-particle lowers the energy. When now adding a second quasi-particle as a neighbor, the coupling between the two corresponding spins is not favored, thus rising the energy of this state. If the energy

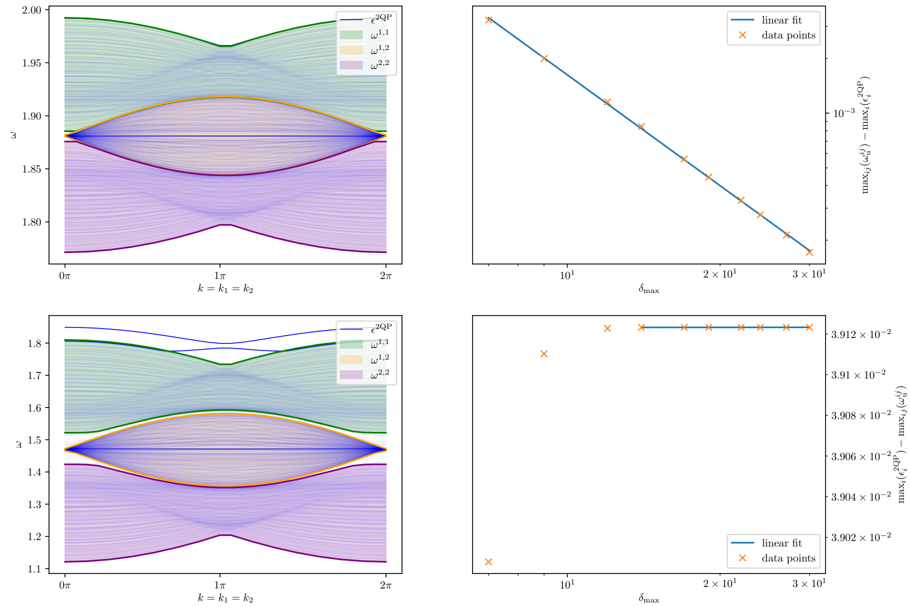

Figure 4.19: On the left side the dispersions of 2QP for $J < 0$, $h = 1$ including quasi-particle interactions is plotted. The momentum is varied in the x-component in the range of one period, by setting $k_1 = k_2$. The 2QP continuum is calculated by using the free particle approximation and diagonalizing the distance matrix M_{dist}. The maxima and minima of the different combinations i, j in equation 4.2.1 are plotted in different colors. The eigenvalues of M_{dist} are plotted in light blue lines. The upper left figure is plotted for $J = -0.1$, the lower left figure for $J = -0.4$. On the right figures the difference between the largest ϵ^{2QP} and the upper edge of $\omega^{1,1}$ of the corresponding left figure at $k = 0$ is plotted for varying $\delta_{\max}$.

of some states in the continuum is decreased or increased by the H_2 terms, we assume these states to step out of the continua which we obtained in the last section. We call these states *bound* or *anti-bound states*, respectively. In contrast to the dense continua, these states form individual bands above or below the continua. For completeness, we have to take all terms in the Hamiltonian into account to get a definitive trend of decreasing or increasing of energy. We will do this later in this section by turning on and off particular terms in H_2.

Starting the discussion, we use the same parameter set as in the previous section, setting $h = 1$, $J < 0$, and varying k_x. We have plotted the dispersion for the values $J = -0.1$ (upper left) and $J = -0.4$ (lower left) in figure 4.19. When comparing the plot for $J = -0.1$ with figure 4.17, where we use the same parameters but set $H_2 = 0$, we obtain no significant difference. The continuum formed by the eigenvalues of the distance matrix, which now also contains the interaction terms H_2, again matches with the free particle approximation. Apart from pure sight, we again can check the difference between the free particle solution and the eigenvalues, by checking the difference in the maximum at $k = 0$. We see that the difference evolves equivalent to figure 4.17, as ϵ^{2QP} approaches the upper edge of $\omega^{1,1}$ from below. When comparing the results more precisely, we obtain a slightly smaller difference for the same maximum distance $\delta_{\max}$. This gives a small hint that the upper eigenvalue moves upwards in energy. Nonetheless, for $J = -0.1$ we obtain no anti-bound state being

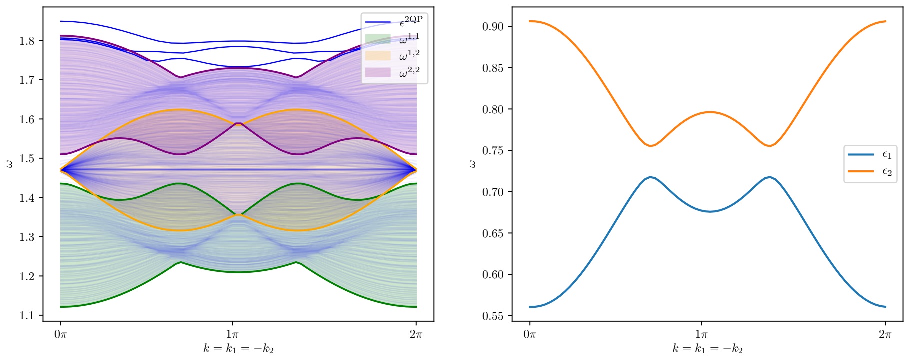

Figure 4.20: On the left side the dispersions of 2QP for $J = -0.4$, $h = 1$ including quasi-particle interactions is plotted. The momentum is varied in the y-component in the range of one period, by setting $k = k_1 = -k_2$. The 2QP continuum is calculated by using the free particle approximation and diagonalizing the distance matrix M_{dist}. The maxima and minima of the different combinations i, j in equation 4.2.1 are plotted in different colors. The eigenvalues of M_{dist} are plotted in light blue lines. On the right figure the 1QP spectrum is shown. In contrast to lower $|J|$, the two bands do not touch each other in the given momentum parameter range.

outside of the continuum. Note, that we have quantitatively only checked the difference for $k = 0$, investigating the momentum $k = \pi$ could already yield a larger effect of the added couplings.

When increasing the Kitaev coupling to $J = -0.4$, we obtain two anti-bound states at the upper edge of the $\omega^{1,1}$ continuum. The upper state lies fully outside of the continuum for the given momenta, while the lower state only leaves the continuum around $k = \pi$. When decreasing J to larger negative couplings, both anti-bound states emerge fully out of the continuum, accompanied by a third anti-bound state, which lies still fully in the continuum for the investigated Kitaev coupling. When taking a look at the three continua $\omega^{i,j}$, these are slightly separated from each other with a maximum spacing for vanishing momentum. Keep in mind, this is not an effect of the H_2 terms but only of the larger coupling J which increases the distance between the two 1QP bands, as can be seen in figure 4.2. It is also interesting to see that the overall structure of the continua stays the same, as the ϵ^{2QP} and $\omega^{i,j}$ values match. So, almost all states are only affected infinitesimally by the interaction between the quasi-particles for the investigated couplings, as only a very small distance between the particles leads to an apparent effect. Additionally, all energies (including those of the anti-bound states) are shifted downwards in comparison to $J = -0.1$. This is grounded in the discussed fact that the bands in 1QP and so also the continua in 2QP are narrow in comparison to the overall slope to lower energies.

To quantify the binding energy of the anti-bound state, we plotted the difference of the anti-bound state and the upper edge of the free particle approximation for varying $\delta_{\max}$. As can be seen the distance first increases as the anti-bound state rises in energy but stays at a finite energy difference of around 0.039 at $k = 0$. We could extrapolate the energy of the anti-bound states as described in the last section to improve the results, but we will stick to the original values for $\delta_{\max} \approx 20$, as the quality is sufficient for our discussion.

For completeness, we plot the dispersion along the y-axis in momentum space in figure 4.20, as done without interaction in figure 4.18. As the formation of the anti-bound states needs a larger coupling than $J = -0.1$, we use the coupling $J = -0.4$, as done in the lower line of figure 4.19. First, we obtain—in contrast to the lower coupling—that the two 1QP bands are fully separated from each other when varying k_y. Nonetheless, the 2QP continua built up of the 1QP bands are still overlapping. Only for the momenta around $k = 0$ the continua split up, as seen for the dispersion along the x-axis, too. For the given interaction, we obtain all three anti-bound states above the top continuum. While the first anti-bound state is well separated from the continuum, the other two states only step out of the continuum for momenta around $k = \pi$, as for the x-direction.

After investigating the dispersion with interactions, we now want to take a closer look at the anti-bound states. Up to now, we have found up to three anti-bound states emerging from the top-most continuum for sufficient large Kitaev couplings. Nonetheless, we can state that the anti-bound states occur at couplings lying within the convergence radius of our calculated series. In the following we will stick to the antiferromagnetic Kitaev couplings $J < 0$, to concentrate on the anti-bound states. For $J > 0$, we can also investigate the building of bound states analogously to the following discussion for $J < 0$.

First, we want to find the driving mechanism which leads to the formation of the anti-bound or bound states. As a first classification, we divide the H_2 processes in three subgroups:

1. *Density-density interaction*. These are all processes where the position of the two quasi-particles does not change. So, we are only considering all processes $\langle 2, i, j \mid H_2 \mid 2, i, j\rangle$ where the starting and resulting state are the same. This case we already discussed analytically in first order at the beginning of this section as a candidate for the formation of anti-bound states for $J < 0$.
2. *One quasi-particle correlated hopping*. In this case one of the particles' positions remains unchanged while the other is moved during the process, reading $\langle 2, \tilde{i}, j \mid H_2 \mid 2, i, j\rangle$ with $\tilde{i} \neq i$.
3. *Two quasi-particle correlated hopping.* In this last case, both particles have to move during the process, reading $\langle 2, \tilde{i}, \tilde{j} \mid H_2 \mid 2, i, j\rangle$ with $\tilde{i} \neq i, \tilde{j} \neq j$.

In figure 4.21 the results of the three above defined subgroups are visualized. On the left figure the dispersion is plotted at $k = 0$ with the eigenstates $\epsilon^{2\mathrm{QP}}$ within the three continua in light blue color. Additionally, the (maximum) three anti-bound states are plotted for the above defined subgroups. This is done by creating M_{dist} by only inserting those H_2 terms which match the conditions of the respective classification. For comparison, the energy of the three anti-bound states for the full effective Hamiltonian are plotted in blue. For a better visualization of the gap between the continuum and the anti-bound states, the difference between the two is plotted in the right figure. For the upper edge of the continuum, the free particle approximation was used as plotted in a dashed line in the left figure.

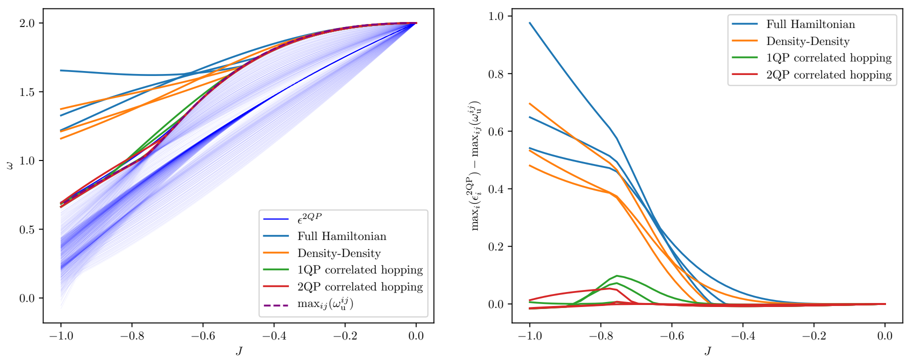

Figure 4.21: Dispersion at $k = 0$ for different antiferromagnetic Kitaev couplings $J < 0$. On the left figure, the full dispersion is plotted with the eigenvalues $\epsilon^{2\mathrm{QP}}$ from the three continua in light blue and the upper edge of the free particle approximation in purple color. Additionally, in different colors the three highest eigenvalues of the diagonalization are plotted for different models which are presented in the main text. On the right figure the distance between the upper edge of the continuum and the highest respective eigenvalues is plotted.

Three anti-bound states are observed for the full Hamiltonian with all correlated processes involved. The first anti-bound state forms at around $J \approx -0.3$ and starts 'growing' exponentially in binding energy. Later on, the distance to the continuum increases roughly linear. The other two anti-bound states feature a similar behavior. Especially the first sector seems to come mainly from the density-density interactions marked in orange. The anti-bound states for the density-density interaction build around the same coupling as the one of the full Hamiltonian and increase parallel in binding energy. The anti-bound states originating from the correlated hoppings emerge for larger couplings at around $J \approx -0.5$ and $J \approx -0.6$ for 1QP and 2QP hoppings, respectively. For both correlated hoppings we do not observe three anti-bound states but only two and one for the 1QP and 2QP hoppings. All anti-bound states are of way smaller binding energy than the one of the density-density interaction. For couplings of around $J \approx -0.9$ the anti-bound state of the one particle hopping vanishes back into the continuum, while the binding energy of the anti-bound state of the two particle hopping decreases slowly. The two particle hopping seems to play a minor role in the anti-bound state of the full interaction Hamiltonian, as the slope with respect to the density-density state starts to differ slightly.

We have to keep in mind that we are discussing effects at very large values of J, which is outside of the 'save' convergence radius. In the following section 4.2.2 we will discuss the area of large Kitaev couplings in more detail to get more insight why we have to be cautious when discussing the physics at these large couplings. As the density-density interaction is the dominant process for the formation of the anti-bound states, we will further on focus on this type of interaction. The other correlated hoppings may play a non-negligible role for large couplings, but as the quality of the calculated series is rather low in this area, we will not go into further details about this specific region.

For the density-density interaction we can further classify it by resolving the impact of the distance of the two quasi-particles. In figure 4.22 we have separated the density-density processes which act on neighbored quasi-particles

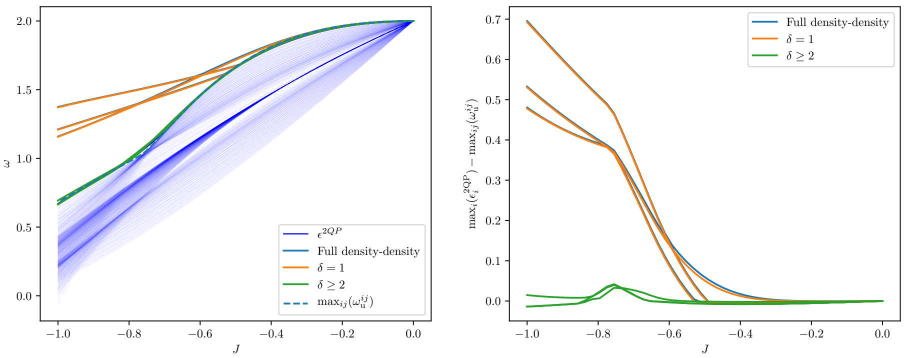

Figure 4.22: Dispersion at $k = 0$ for different antiferromagnetic Kitaev couplings $J < 0$. On the left figure, the full dispersion is plotted with the eigenvalues $\epsilon^{2\text{QP}}$ from the three continua in light blue and the upper edge of the free particle approximation in purple color. Additionally, in different colors the three highest eigenvalues of the diagonalization are plotted for the full density-density interaction and split into different distances of the quasi-particles. On the right figure the distance between the upper edge of the continuum and the highest respective eigenvalues is plotted.

($\delta = 1$) and those processes which act on quasi-particles which are not neighbored (having a distance $\delta \geq 2$). In other words, for the latter case all states whose quasi-particles are neighbored to each other are not coupled to each other and so can not build up an anti-bound state. If an anti-bound state forms, we know that it consists only of states with a distance larger than one.

The result is pretty clear, as there is no state emerging out of the continuum for distances $\delta > 1$. On the other side the states obtained by the full density-density interaction have nearly the same energy as the ones being restricted to neighbored quasi-particles. For couplings around $J \approx -0.7$ we see small anti-bound states for higher distances. In this region the maximum of the one quasi-particle dispersion changes from being at $k = 0$ to $k_1 = 2/3\pi, k_2 = 4/3\pi$. As this takes place at a large perturbation we can not make a clear statement if this maximum movement and also the building of the anti-bound states is physical or an effect of divergence of the perturbation series.

These two figures specify the effect leading to the anti-bound states very precisely. Using the obtained results, we can identify the driving mechanism as a density-density interaction of neighbored quasi-particles. To get further evidence for this finding, we investigate the eigenvectors of the anti-bound states obtained by diagonalizing the distance matrix M_{dist}. As the basis is built up of the two quasi-particle states with different distances between the particles, we obtain an amplitude of these different distances, when investigating the eigenvectors. In the following we will use the full matrix M_{dist} without restricting the couplings as done before. Nonetheless, we expect the density-density interaction being the driving force for the anti-bound states.

The result is plotted in figure 4.23 using the standard set of uniform parameters with $\delta_{\max} = 20$ and vanishing momentum. For the discussion, we have chosen the two couplings $J = -0.4$ and $J = -0.6$, with the first coupling only applying on the upper left plot and the latter on the upper right and the image below.

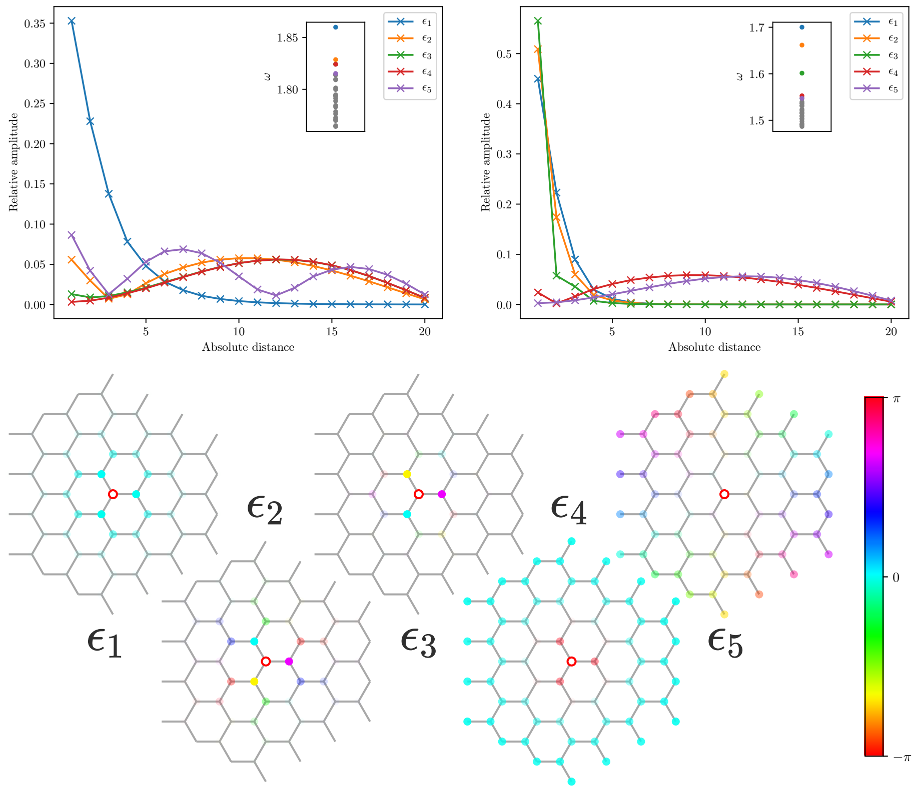

Figure 4.23: Visualization of the eigenvectors of the highest eigenvalues obtained by diagonalizing the distance matrix M_{dist} at $k = 0$. The upper two figures show the absolute amplitude of the eigenvectors decomposed into the distances between the quasi-particles, with the left figure at a coupling $J = -0.4$ and the right figure at $J = -0.6$. The index i in ϵ_i corresponds to the energy level in descending order, with 1 being the highest eigenvalue. The highest eigenvalues are plotted in the inlay, the gray eigenvalues are the following ones whose eigenvectors are not plotted in the main figure. The connecting lines for the eigenvectors are a guide to the eye, as non-integer distances are not possible. The lower figure shows the eigenvectors for the five highest eigenvalues for $J = -0.6$. The distance is defined between the red circled site and the corresponding colored site. The opacity shows the magnitude and the color the phase of the coefficient of the respective distance. The magnitude in opacity is normalized for each eigenvector individually.

For the upper two figures, the eigenvectors of the five highest eigenvalues ϵ_i in descending order are visualized, while the eigenvalues are plotted in the inlay. The eigenvectors are decomposed into the absolute distance of the basis states. The connection lines between the crosses serve only as a guide to the eye, as the absolute distance lies in $\mathbb{N}$. In both upper plots the eigenvector decomposition can be divided into two categories. The eigenvectors of the highest eigenvalues (ϵ_1 for $J = -0.4$ and $\epsilon_1, \epsilon_2, \epsilon_3$ for $J = -0.6$) fall exponentially in intensity for rising absolute distance. The following eigenvalues have eigenvectors whose amplitudes are spread over all distances with (normally) no peak at low distances. Note that the intensities are spread over all distances up to the maximum distance $\delta_{\max}$. As the thermodynamic limit lies at $\delta_{\max} \to \infty$, the behavior around $\delta_{\max}$ does not match with the one in the thermodynamic limit. As we can see in the two eigenvalue-insets, these categories correspond to whether the state is an anti-bound state or in the continuum. This matches with our previous findings that the driving force of the anti-bound states is given by the density-density interaction between nearest-neighbored quasi-particles. So, when increasing the weight of the basis states with $|\delta| = 1$ between the particles, the energy of these states is increased. Thus, the anti-bound states are mainly formed out of states with small distances between the two quasi-particles. For the left figure, we see—apart from the one anti-bound state at ϵ_1—two states at energies ϵ_2, ϵ_5 which have a small peak at $\delta = 1$. This could be the start of the formation of the two remaining anti-bound states, emerging at larger couplings.

When comparing the distribution of the amplitudes of the anti-bound states in the two plots, we obtain a faster decrease in amplitude for the larger coupling. Interestingly, the state with energy ϵ_3 for $J = -0.6$, falls fastest with respect to the other two anti-bound states. In the lower plot we take a closer look at the eigenvectors of the highest eigenvalues in descending order from left to right for $J = -0.6$. In contrast to the above plots, the eigenvectors are decomposed into their 'real' distances, being the distance between the red circled 'origin site' and the corresponding colored site. The absolute value of the coefficient of the respective distance is given by the opacity of the circle and the phase in the complex plane is given by the color. First, we again see the two categories of amplitudes being restricted to small distances for the anti-bound states and being spread over all distances for the states in the continuum. The absolute values for a given total distance are distributed evenly onto the different directions. This can be explained by the choice of the uniform magnetic field and Kitaev coupling and the vanishing momentum not favoring any direction on the lattice.

Investigating the phase distribution of the different eigenvectors, we obtain real-valued coefficients for the energies ϵ_1, ϵ_4 being the upmost anti-bound state and the upper edge of the continuum. This relation also maintains for different couplings (not shown), as for $J = -0.4$ the eigenvectors for ϵ_1, ϵ_2 are real-valued. Because an eigenvector can be multiplied with a complex number without changing the corresponding eigenvalue, we can only argue with the relative phase between the single distances, while the absolute phase is arbitrary. The other shown eigenvectors have a phase depending on the 'angle' of distance, meaning the angle having the red circled site as origin. When going around the origin, we gain a phase of $\pm 4\pi$, as can be seen best for ϵ_5. The phase-change is opposite for ϵ_2 and ϵ_3 as well as for ϵ_5 and ϵ_6 (not shown). According to the corresponding energies, having no phase difference seems to increase the energy, as both the highest anti-bound state and the upper edge of the continuum share this feature. It would be interesting to investigate the impact of the obtained phase differences in more detail, as they seem to be an elementary structure of the first eigenvalues. Even with these open questions, we have strengthened the finding that the anti-bound states are built by the density-density interaction of the neighbored quasi-particles.

Having identified this next neighbor interaction as the driving force for the anti-bound state, we can also use this fact to argue for the number of three anti-bound states. When neglecting all other kinds of interactions and hoppings in the effective Hamiltonian, we are left with the local terms including the density-density interaction. For our given lattice structure, we have three different distances for

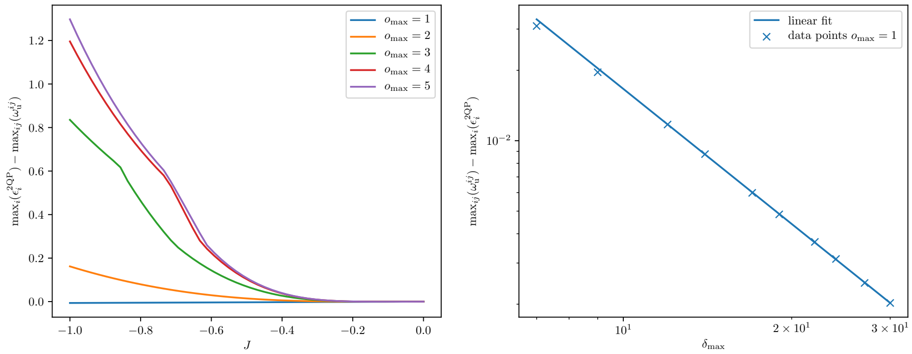

Figure 4.24: Difference of the highest eigenvalue of the distance matrix and the upper edge of the 2QP-continuum determined by the free particle approximation for varying Kitaev couplings J. The calculations are restricted to a varying maximum order $o_{\max}$ up to order five. On the right figure the difference in first order is plotted separately for fixed $J = -0.7$ and varying maximum distance $\delta_{\max}$ for M_{dist} in a log-log plot.

two quasi-particles to be next to each other, as each lattice site is connected to three sites. It is important that all three configurations are not connected by a translation with respect of the lattice vectors a_1, a_2. For these three distances we have found a strong increment of energy, leading to anti-bound states. The corresponding states of these three distances form superpositions—as can be seen in figure 4.23—with different phase factors between the three 'distance-states'.

As a final step for exploring the nature of the anti-bound states at $k = 0$, we want to find out which is the minimum order where the anti-bound states appear. As we have found out the driving mechanism for the anti-bound states is mainly given for states with small distances between the particles, theoretically there is no minimum order as the interaction between the quasi-particles contributes already in first order. For analyzing the different orders, we built up M_{dist} only adding terms up to a maximum order $o_{\max}$ and also calculating the free particle approximation up to order $o_{\max}$. We again choose our standard parameter set and calculate the eigenvalues at vanishing momentum. As a criterion for an anti-bound state we use (as before) the distance of the largest eigenvalue to the upper edge of the free particle approximation. The result up to order five is plotted in figure 4.24. On the left side the binding energy is plotted for varying antiferromagnetic couplings J for the different orders. We can see clearly that a gap between continuum and the maximum energy state opens, starting at order two. The gap opens roughly at the same coupling for $o_{\max} \geq 2$, though it opens at way slower speed for order two. The higher orders have a binding energy of similar strength, especially for the two highest orders plotted. Keep in mind that we only plotted the largest eigenvalue, ignoring the other two emerging anti-bound states at larger couplings.

An interesting finding is the vanishing gap for the first order although the density-density interaction is already contributing at order one. In the right figure the difference is plotted for order one with fixed coupling $J = -0.7$ with varying maximum distance $\delta_{\max}$, as done previously. Using this data, we can conclude that no anti-bound state has built for this relatively large coupling, as the gap converges to zero for $\delta_{\max} \to \infty$. We can deduce that the higher

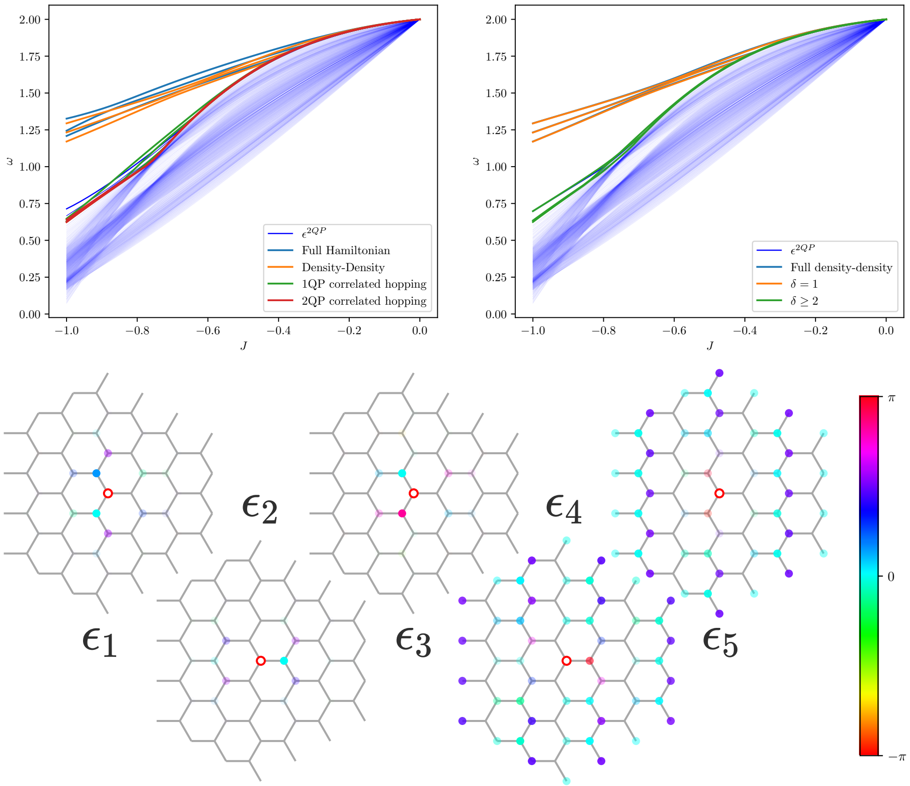

Figure 4.25: Overview of the anti-bound states for uniform $J < 0$, $h = 1$, and a non vanishing momentum $k_1 = k_2 = \pi$. This corresponds to a momentum in x-direction. In the upper left figure the 2QP interactions are split up into the density-density and correlated hopping actions. For all cases the largest eigenvalues are plotted for varying interaction J. Additionally, the continuum is plotted in blue. As the density-density interaction is the driving force for the anti-bound states, on the upper right figure the interaction is further classified into distances of interaction. Last, for the case of $J = -0.6$ the eigenstates of the five largest eigenvalues of the full distance matrix are visualized. The distance is defined between the red circled site and the corresponding colored one. The opacity of the sites shows the magnitude and the color the phase of the coefficient for the respective distance state. The magnitude in opacity is normalized for each eigenvector individually.

orders of perturbation (especially orders two and three) add a higher weight to the density-density interactions, which is needed for the states to emerge out of the 2QP-continuum.

Up to now, we fully concentrated, on the standard parameter set and also a vanishing momentum for the analysis of the anti-bound states. While we will keep the uniform parameter set and restrict the following discussion in length, we take a short look at the anti-bound states at another total momentum, to check for similarities and deviations to the case of $k = 0$. As one example we investigate the anti-bound states for $k_1 = k_2 = \pi$ in figure 4.25. Earlier in this section we have already analyzed the dispersion along this momentum path in figure 4.19, including the specific momentum. First, in the upper left plot, we classify the two quasi-particle interactions, as defined earlier in this section. Therefore, we plotted the four highest eigenvalues of the distance matrix, for the different classes of interaction in different colors. The results are very similar to the case of vanishing momentum. Again, the driving mechanism is the density-density interaction, inducing no movement of the quasi-particles. The correlated hoppings do not lead to clearly separated anti-bound states. One small derivation to $k = 0$ can be found, as for large couplings a fourth anti-bound state seems to built up, as can be seen in blue and orange right above the dark-blue continuum. Also this potential fourth anti-bound state is built out of the density-density interaction. As before, we have to be cautious as this effect only occurs at very large Kitaev couplings and is a small effect. So, only by these plots we can not be sure whether this anti-bound state is physical or not. Next, we have subclassified the density-density interaction depending on the distance of the interacting quasi-particles on the upper right plot. As for $k = 0$ the interaction of next neighbored particles is the crucial force driving the anti-bound states. The potential fourth anti-bound state builds out of an interaction between particles of larger distance, as all possible distances with $|\delta| = 1$ are contained in the first three anti-bound states. Last, we have visualized the eigenstates of the five highest eigenvalues of the full distance matrix for $J = -0.6$ below the two plots. Again, the three first states have their main weight on the three smallest distances, leading to the three known anti-bound states. In contrast to $k = 0$ the intensities and phases are oriented along the vertical axis. This is more visible for ϵ_4, ϵ_5, where we have a constant phase for the distances along the vertical axis. This can be explained by the momentum which is pointing in the horizontal direction. Despite this new structure of the phases, the eigenstates of the smaller eigenvalues focus again on the larger distances, as analyzed in more detail for the vanishing momentum case.

Summarizing this short analysis of a non-vanishing momentum, we have found again three clearly anti-bound states, coming out of the same next-neighbor density-density interactions. The structure of the eigenstates is analogue to the previous case in principle, but has a different phase distribution being oriented by the momentum in x-direction. As a small deviation, we have found a potential fourth anti-bound state at large couplings, which builds up by a density-density interaction of not next-neighbored quasi-particles. Because the new-found anti-bound state is not well separated from the continuum and the couplings a very large, we can not confirm if the state is physical.

4.2.2 Breakdown of the separated quasi-particles assumption

During the previous discussion we sometimes were cautious when examining effects at large Kitaev couplings, as for example the forth anti-bound state or the correlated hopping effects in the last section. One side of the explanation is mathematical: As we calculate our physical quantities based on perturbative series coming out of the pCUT method, we have to deal with the finite convergence radius and an error as we only calculate the series up to a finite order. Depending on the behavior of the coefficients of the higher orders the error is differently large. If the coefficients would decrease in absolute values 'fast enough' for increasing order, the error from only considering finite order would be comparably small. But as we saw in the discussion of the 1QP dispersion series in equation 4.1.2, the coefficients of the higher orders do not decrease in magnitude. So, it is likely that this behavior is exemplary for the obtained series in this model in general. We can increase the quality by rising the maximum order of calculation. As the increment of one order roughly corresponds to the extension of computation time of a factor of around 10-20, the achieved orders are quite general for the computation power nowadays. The more doable approach of increasing the convergence radius is the usage of extrapolations as introduced in section 3.4 and used in the discussion of 1QP in section 4.1. As we used a 'more physical' ansatz for the extrapolations by allowing discontinuities, the quality increased for the discussed cases.

Apart from this general problem of finite order calculations of an infinite series, we can also approach the question of errors in the obtained series expansions in a more physical way. The main idea of the pCUT method is a block-diagonalization of the Hamiltonian, by transforming the basis in a way that the interactions between the different quasi-particle channels vanish, as visualized in figure 3.4. The result of this transformation is the formation of bands and continua (only in 2QP and higher QP channels) which do not interact with those of other QP channels. Physically, this seems to be a valid approach, as for small perturbations the eigenvalues of the different QP channels are far away from each other. So, for zero temperature it is logical to assume no interaction between the individual quasi-particle channels as the energy differences between those is too large. Thinking about the limits of this separated particle channels, an obvious one can be found when different particle channels begin to overlap in energy. Concretely, if two states of different QP channels have similar or even the same energy, this makes a coupling between these states non-negligible. Due to this coupling, quasi-particles can e.g., decay when having a process from a 2QP to a 1QP state. But these types of interactions are not considered when discussing the QP channels separately. So, when we discuss physical quantities within the regime of overlapping QP channels we do not fetch the physical behavior anymore, as the formation of coupled states between the channels is neglected. This is an error which is independent of the above described one of finite perturbation order and can only be solved when including interactions between the overlapping channels somehow.

In the following we want to investigate the overlap of the 1QP and 2QP sector. First and most importantly, we determine the critical perturbation strength J_{crit} where the two channels begin to overlap. As before, we will concentrate on the case of uniform antiferromagnetic Kitaev couplings and a uniform magnetic field for the discussion. By varying the Kitaev coupling J and comparing the upper 1QP band and the lower edge of the 2QP continuum (using the free particle approximation), we obtain a critical coupling of

$$J_{\text{crit}} \approx -0.568\,,$$

where we used dlog-Padé extrapolations for a more accurate result. The result is visualized in figure 4.26. On the left side the dispersion along the momentum path $k = k_1 = k_2$ is plotted for the coupling J_{crit}. For the two bands in 1QP we have used dlog-Padé extrapolations to increase the quality, as we operate on comparably large perturbations. The corresponding 2QP continua were calculated by taking the mean values of the 1QP extrapolations. As the quality of the extrapolations is very high in this regime, the standard deviation is of order

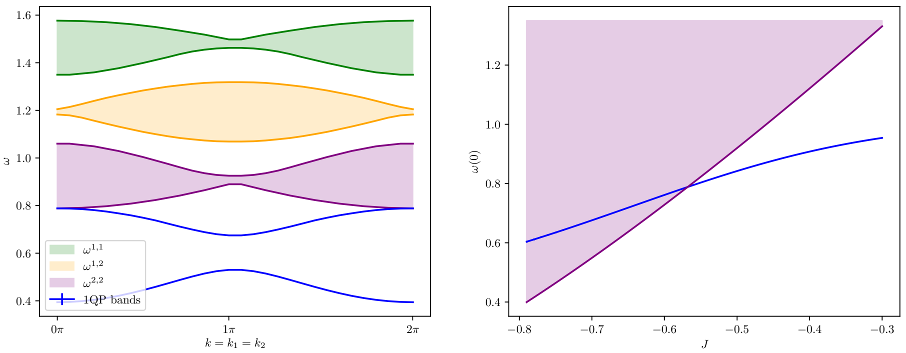

Figure 4.26: Dispersion of the one and two quasi-particle channel at the coupling J_{crit} where the 1QP and 2QP sectors begin to overlap. The dispersion on the left side is chosen along the momentum path $k = k_1 = k_2$ for one period. The dispersion was already discussed for smaller couplings separately for the 1QP and 2QP case. The upper 1QP band and the lowest continuum touch each other at vanishing momentum. On the right side the upper 1QP band and $\omega^{2,2}$ are plotted for $k = 0$ for varying J. We determine J_{crit} by calculating the intersecting point between the two plotted curves. For better results, all lines were calculated using the dlog-Padé extrapolants.

10^{-3} to 10^{-4}. The plot shows the familiar dispersion as investigated in figures 4.15 and 4.19. As claimed for J_{crit} the upper 1QP band and the lower end of the purple continuum touch each other at vanishing momentum. For finite momenta the two particle sectors are still quite well separated. Nonetheless, starting at the latest for this coupling, we ignore processes between states of different particle sectors which can have an impact on the overall dispersion. This effect will increase when going to even larger couplings.

Additionally, the gap between the quasi-particle sectors is plotted on the right side of the figure. As the gap between the sector is smallest for $k = 0$, we fix the momentum to this point and vary the coupling J. We see the upper 1QP band moving into the 2QP lower continuum for $J \geq J_{\text{crit}}$. We determined the critical coupling by searching for the point of the closing gap.

After finding the critical coupling were the 1QP and 2QP sectors begin to overlap, we can search for further evidence of the starting interaction between the two sectors. For that we investigate the dlog-Padés of physical quantities around J_{crit}. As described in section 3.4, we have defined the dlog-Padé extrapolants in a way that roots in the denominator can relate to physical critical values. So, when finding poles for the extrapolants around J_{crit}, we obtain further clues for a changed behavior of the physical quantity because of the starting overlap.

We first investigate the dispersion for vanishing momentum. To have more data points, we choose a larger set of five families ($\Delta_{\max} = 2$), which we analyze for poles. As the position of the poles z_{pole} lies in the complex plane, we plot the positions on a 2D scatter plot in figure 4.27. In order to distinguish the poles of the upper and lower 1QP band, these are plotted in different colors. First, we obtain several poles on the real axis which can not be physical (or at least we can not explain it) as they happen for very small couplings. For larger couplings around $J = -1.1$ we obtain the poles of the lower band indicating the phase transition as discussed in the 1QP section. Last, we focus on the poles around

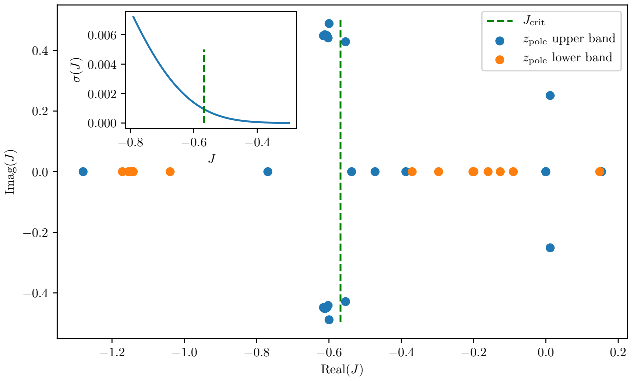

Figure 4.27: Position of the poles z_{pole} for the dlog-Padé extrapolants with $\Delta_{\mathrm{max}} = 2$ for the 1QP bands at $k = 0$. As the position can be complex, on the x-axis the real part and on the y-axis the imaginary part is plotted. The poles of the upper band are plotted in blue, the poles of the lower band are plotted in orange. The critical coupling J_{crit} is indicated with a green dashed line. For quantifying the quality of the dlog-Padé extrapolations of the upper band, the standard deviation σ is plotted in the inset for varying couplings.

J_{crit}. First, we obtain several poles around the critical value. For the upper band this is the biggest collection of poles forming around J_{crit}. Furthermore, we find only poles of the upper 1QP band, which fits to the proposed physics as only the upper band of the 1QP dispersion intersects with the 2QP continuum. As a short comment: the poles are symmetric with respect to the x-axis, as they describe the energy, which is a real valued function. Nonetheless, the convergence of the upper band is quite good even for couplings larger than J_{crit}. In the inset plot the standard deviation $\sigma(J)$ of the dlog-Padés is plotted showing a exponentially rising amplitude which is comparably small for the plotted couplings.

As a second example we come back to the spectral weight of section 4.1.2, which we plotted in figure 4.12. This time we concentrate on the dlog-Padé extrapolants for the spectral weights of the different QP channels. In figure 4.28 we have plotted the highest order of the spectral weights divided up into the weight of the different quasi-particle channels and normalized by the total weight I_{tot}. Additionally, the dlog-Padé extrapolations are plotted in dashed colored lines. As done for the dispersion before, we searched for poles in the plotted coupling region. The real part of the position z_{pole} of the poles is plotted as crosses in the color of the respective extrapolation. We see that for the 1QP weight I_1 there are several poles just before the intersection of the 1QP and 2QP sector. We would expect poles for the 2QP weight, too, being the counterpart of the intersection. We do not find poles directly in the region of J_{crit} but only at way smaller couplings. As we have only two valid extrapolations for I_2, the study of these is not very solid. Probably, we would find more poles when going to higher orders in the perturbation series. An promising explanation for the pole at $J = -0.333$ in I_2 is the starting intersection between the 2QP and 3QP channels starting at around $J_{\mathrm{crit}}^{\mathrm{2QP}\rightarrow\mathrm{3QP}} \approx -0.337$. We do not find any poles for the extrapolation of I_0 as the ground state is well separated in energy from the 1QP channel, because the band gap does not close in the investigated region. To check the quality of the extrapolations of I_1—which has the highest quality,

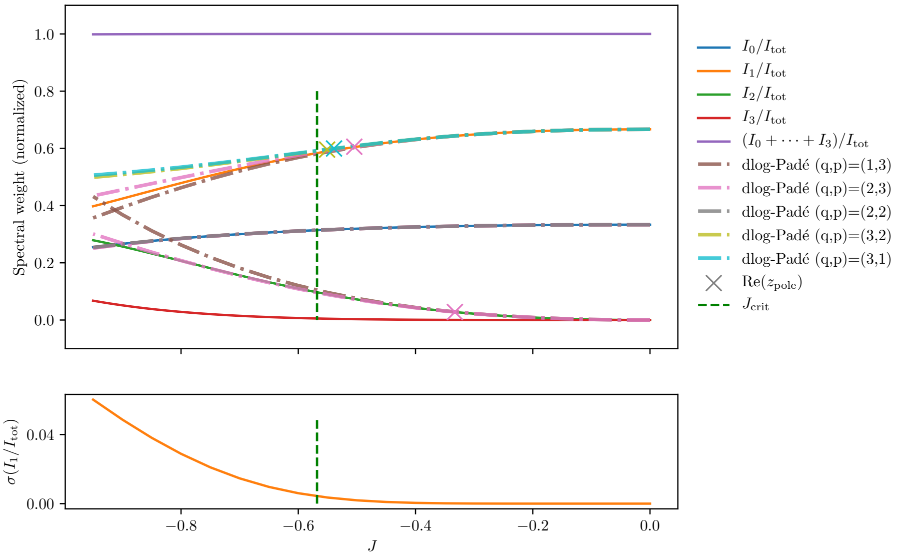

Figure 4.28: Spectral weights for varying antiferromagnetic couplings as done in figure 4.12. The highest order of the series expansion of the spectral weights I_i is plotted in lines of different color and is normalized by the total weight I_{tot}. In dashed lines the corresponding dlog-Padé extrapolations are plotted. The real part of the poles in the investigated coupling regime are visualized with crosses of the color of the corresponding extrapolant. In the lower smaller plot the standard deviation σ of the dlog Padés of I_1 is plotted. As a guide to the eye the critical coupling I_{crit} is plotted as a dashed green line.

as we have the highest number of valid extrapolations—we plotted the standard deviation of the extrapolations for varying couplings in the smaller plot at the bottom. As we can see in both plots, the inaccuracy starts to increase drastically around the critical coupling. So, we can assume the inaccuracy not only being grounded in the errors made by cutting the infinite perturbation series but also in the neglected interactions between the different quasi-particle channels.

Summarizing, we have found strong evidence that we can track the point of starting intersections between QP channels by investigating the poles of the calculated dlog-Padés. For the discussion, we are restricted by the maximum order of the calculated series. It would be interesting if more poles around the intersection points would occur if we would have series of higher order at hand. Furthermore, we found—at least for the spectral weights—a strong decrease in quality for the area of intersecting QP channels, measured by the standard deviation of the extrapolations. Again, a higher order of the bare series would give a larger set of valid extrapolations for estimating the quality of them. For most of this thesis we stay within the parameter range of clearly separated quasi-particle channels, to use pCUT without a loss of accuracy. But as we want to compare our results with those of the DMRG paper from Gohlke et al. [14] later on in section 4.3, we will have to go into the area of overlapping quasi-particle sectors. For this case we have to bear in mind the breakdown of the separated particle channels and due the loss of certain physical processes that can have a big impact on the real physical model.

4.2.3 Spectral density

After investigating the 2QP dispersion with a special focus on the properties of the anti-bound states (with its limits), we move on to the spectral properties of the 2QP sector. We will again concentrate on the observable $O(i) = \sigma_i^z$, as defined in equation 4.1.7. After the rotation of the system to orientate the magnetic field along the z-axis, the observable has the form

$$\begin{aligned} \mathcal{O}(i) = U^\dagger O(i) U &= \frac{1}{h}\left(h_z\sigma_i^z - \sqrt{h_x^2 + h_y^2}\sigma_i^x\right) \\ &= \frac{1}{h}\left(h_z(1 - 2b_i^\dagger b_i) - \sqrt{h_x^2 + h_y^2}(b_i^\dagger + b_i)\right) \end{aligned}$$

as given in equation 4.1.9. As we have already discussed the spectral weight of the observable for the different quasi-particle channels in section 4.1.2.1, we will only shortly discuss the spectral weight I_2 of the 2QP channel. In contrast to the 1QP sector, I_2 has no contribution in zeroth and first order. This comes from the structure of the observable having a term creating and annihilating one quasi-particle. So, in zeroth order when only $\mathcal{O}(i)$ is applied onto the ground state, we will only have a contribution for the ground state and the one quasi-particle channel. As we have seen in this section, the 2QP weight starts to contribute in order two. This results in a comparably low weight for small perturbation, as can be seen in figure 4.12. Nonetheless, for large enough couplings we obtain a non-negligible weight I_2 which makes it reasonable to investigate the 2QP spectral quantities in more detail.

4.2.3.1 Static structure factor

We will start—as for the 1QP case—with the static structure factor, which gives us information about the momentum resolved effective observable. For more theoretical information about the static structure factor, see section 3.2.4 in the methods chapter. We again focus on the case of the uniform magnetic field $h = 1$ and uniform Kitaev couplings J. In figure 4.29 the static structure factor of $\mathcal{O}$ for 2QP S_2 is plotted for two different couplings $J = -0.1$ and $J = -0.4$ in the figures 1 and 2. Keep in mind that on $\mathcal{O}$ the pCUT method is applied to be in the same basis as the effective Hamiltonian H_{eff}, conserving the number of quasi-particles for the effective Hamiltonian.

When comparing the result to the one of the 1QP case in figure 4.13, we first observe a very different absolute intensity and structure in k-space. This matches with our findings of the spectral weight, as I_2 is much smaller than I_1 for the investigated couplings. Nonetheless, the spectral density increases drastically for larger couplings as already can be seen in the second plot. When comparing the mean of S_2 with the 2QP weight I_2, the two match quite well—as expected because I_2 corresponds to the integral of S_2 over all momenta. The overall shape of S_2 is roughly comparable to a distorted chessboard as we have approximate rectangular maxima and minima areas, which are alternating. In contrast to the 1QP case, the maximum of S_2 lies at vanishing momentum for antiferromagnetic couplings. When reminding ourselves of the characteristic tilt of the structure of S_1, induced by the lines of constant density, we observe the same tilting angle for the S_2 structure. Indeed, the characteristic direction in momentum space

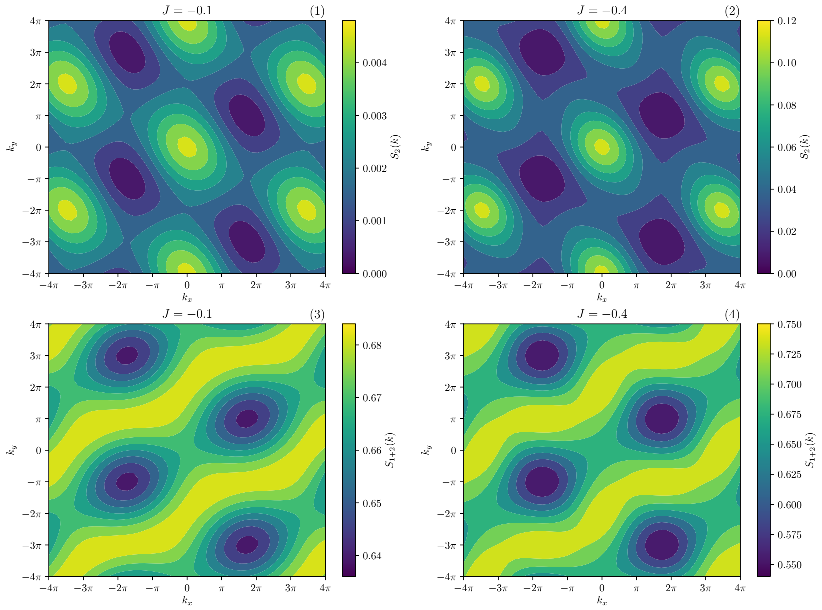

Figure 4.29: Static structure factor of $\mathcal{O}$ as given in equation 4.1.9 for a uniform magnetic field $h = 1$ and two different antiferromagnetic uniform couplings $J < 0$. Note that we do not use the b_1, b_2 basis for describing the momentum but decompose the momentum in the x- and y-component in real space. The spectral density is given in the same units as the spectral weights. In plots 1 and 2 the static structure factor S_2 of the two quasi-particle channel is plotted. In the plots 3 and 4 the static structure factors of the 1QP and 2QP channels are summed up and plotted as $S_{1+2}(k) := S_1(k) + S_2(k)$.

is again parallel to the lattice vector a_1. This corresponds most likely to the chosen original observable σ^z being parallel to the z-bonds. For a more detailed discussion, see section 4.1.2.2 for the one quasi-particle case.

We can analyze the period length along the a_1 direction, starting from vanishing momentum $k = 0$ and going along the a_1 vector until one period finished. We find the period to be of length 4π. More concrete we use the definition in equation 4.1.11 and define 2π along the a_1 direction as the momentum

$$\vec{k} = \frac{2\pi}{\sqrt{12}} a_1 \,. \tag{4.2.2}$$

As we defined a_i as $a_i \cdot a_i = 1/\sqrt{12}$, the chosen momentum $\vec{k}$ corresponds to no phase difference between sites with a distance of a_1 between them. So, the periodicity of 4π matches with the momentum $2\vec{k}$, as chosen above. The same period length can be found in the 1QP static structure factor along the analyzed lines. When going to larger couplings the period length stays constant and also the chess-like grid only changes slightly. This period of 4π is grounded in the geometry of the honeycomb model. To cycle through one period along the a_1 direction, we demand no phase difference between all sites along the a_1 direction. As motivated, for sites with a distance of a_1, this is fulfilled by $n \cdot \vec{k}$, with $\vec{k}$ from equation 4.2.2 and $n \in \mathbb{Z}$. But as we have two-site primitive cells, the same has to be fulfilled for distances of $r_2 - r_1$ between the two sites in the primitive cell. Calculating the phase of $(r_2 - r_1) \cdot n\vec{k}$, we obtain no phase difference for $n \in 2\mathbb{Z}$, resulting in an overall period of 4π.

Another interesting finding is the summation of the two quasi-particle channels S_1 and S_2. We define the static structure factor of 1QP and 2QP as

$$S_{1+2}(k) := S_1(k) + S_2(k)\,.$$

Physically, we obtain the spectral density of one and two quasi-particles at a given total momentum k. We have plotted S_{1+2} in the plots 3 and 4 of figure 4.29. As S_2 is of negligible intensity for $J = -0.1$, the plot of S_{1+2} is roughly the same as the one of S_1. Because the intensity of S_2 is increased by a factor of around 20-30 for the higher coupling, the plot of S_{1+2} differs more from the one of S_1. Interestingly, the structure of plot 4 looks very similar to that of plot 3, despite the larger width of different intensities. We can conclude from this finding that the overall structure of the static structure factor stays roughly the same for the investigated range of couplings. We can make this statement for the complete static structure factor as the higher quasi-particle channels are negligible for these couplings as can be seen in figure 4.12. The main effect of increased couplings lies in a shifting of spectral density from the 1QP to the 2QP channel. This does not happen isotropically but in the obtained shape of a distorted chessboard, as found before in figures 1 and 2. Going to even larger couplings, the overall structure of S_{1+2} changes. Probably this is grounded by a further shifting of intensity to even higher quasi-particle numbers. As we are restricted in calculations to 1QP and 2QP, we can not prove this assumption. Moreover, we start to operate in the area of couplings where the different quasi-particle channels intersect (see section 4.2.2), making it even harder to compute reliable results as the uncertainty of the bare series and extrapolations rises.

4.2.3.2 Dynamical structure factor

After investigating the structure of the observable in k-space, we move on to the dynamical structure factor, also taking the energy ω into account. We have introduced the dynamical structure factor $S(\omega, k)$ in section 3.2.4 and already calculated $S_1(\omega, k)$ for the 1QP case in section 4.1.2. As discussed in both mentioned sections, we use the information about the eigenstates of the Hamiltonian (in k-space) to calculate the spectral density of the respective states.

This approach, written down in equation 3.2.22, has the limitation that we can only apply it to a discrete spectrum, as we use the shape of a δ-function when applying Dirac's identity. As we have seen in the previous discussion of the 2QP sector, the dispersion—apart from the (anti)-bound states—consists of three continua for the thermodynamic limit. To deal with the continua, one has to approach differently to the original spectral density definition in equation 3.2.21. Following [12, 41], one can calculate $S(k, \omega)$ by tridiagonalizing the distance matrix M_{dist} in a continued fraction expression.

Due to time limitations for this thesis, we will not use this tridiagonalization approach but restrict ourselves to the ansatz described above for 1QP, using equation 3.2.22. For our anti-bound states the usage of Dirac's identity is fine, as they are discrete in the spectrum of H_{eff}. As we calculate the eigenenergies of

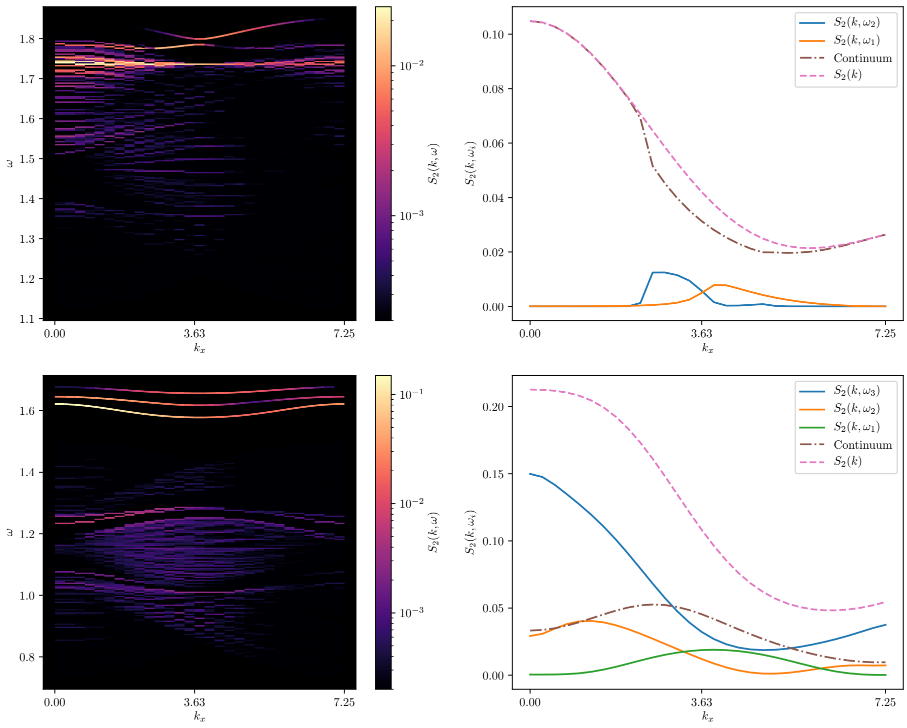

Figure 4.30: Dynamical structure factor for a uniform magnetic field $h = 1$ and uniform antiferromagnetic couplings $J < 0$. The spectral density is plotted for different momenta by varying k_x and setting $k_y = 0$. In the upper line of plots the coupling $J = -0.4$ and for the lower line of plots the coupling $J = -0.6$ is used. On the left side the energy of the 2QP states is plotted on the y-axis and the spectral density for the single states is given in color code. For the continua, we rasterize the spectrum in energy-slices and sum up the density of all states lying within this slice. For more information, see the main text. On the right side the spectral density is plotted directly for the anti-bound states (having ω_1 as the highest energy, with decreasing energies for higher indices) and the total density of all continua. The static structure factor is plotted in a dashed pink line.

the effective Hamiltonian using the finite distance matrix M_{dist}, we effectively obtain a discrete spectrum also for the region of the continua, as can be seen in several plots, as figure 4.17. So, we can use the obtained discrete eigenstates, to calculate the spectral density on them, as done for 1QP. For $\delta_{\max} \to \infty$, the number of states within the region of the continua goes towards infinity, resulting in a vanishing density on the single eigenstates. To deal with this problem, we rasterize the spectrum of energies in the area of the continua and accumulate the spectral densities of all states within the respective energy range. In that way, we obtain an approximation of the spectral density of the continuum, with an accuracy depending on $\delta_{\max}$ and the fineness of the raster.

As in the 1QP discussion, we use the standard parameter set and choose a momentum path along the x-axis in real space, by varying $k = k_1 = k_2$. The result can be seen in figure 4.30. As we found no anti-bound states for $J = -0.1$ in figure 4.17, we use larger couplings $J = -0.4, -0.6$ to be able to investigate the anti-bound states, too. On the left side the 2QP spectral density is plotted for the two couplings, while on the right side the magnitude of the respective densities is plotted for the anti-bound states and the total density of the continuum (by adding up all densities of the states in the continuum). As mentioned before, the continuum on the left-sided plots is approximated by rasterizing, resulting in a grained image, while the anti-bound states' density is directly calculated with equation 3.2.22. Note, that the left-handed plots are plotted with a logarithmic color code in order to visualize the spectral structure over several orders of magnitude.

For a better understanding of the upper left figure, we can relate it to figure 4.17, where the 2QP dispersion is plotted for the same parameters at $J = -0.4$. From there we know that only one anti-bound state has fully emerged out of the continuum, while a second anti-bound state only forms at momenta around $k = \pi$. The upper anti-bound state features very low intensity for small k-values. When going towards $k = \pi$, we obtain a strong increment of intensity which again vanishes when moving further to $k = 2\pi$. The increasing intensity of the upper anti-bound state, seems to be grounded in a shift of intensity from the lower anti-bound state emerging out of the continuum to the upper state. We have seen the same effect for the 1QP spectral density, where the intensity also shifted from one band to the other for momenta around $k = \pi$. Moving on to the continua, the upper continuum shows the highest density, especially for small momenta. One interesting feature is the formation of one bright density-line being constant in energy, touching the upper edge of the continuum for $k = \pi$. Comparing the overall intensity of the continua and the two anti-bound states, the continuum has the way higher contribution, as can be seen quantitatively in the upper right figure. The spectral densities of the anti-bound states do only have a considerable intensity around $k = \pi$. The kink in the density of the lower anti-bound state is located at the point where the state emerges out of the continuum, as we can only calculate a valid spectral density for the state when being outside of the continuum. For the rest of the momenta, we use the upmost state within the continuum, instead. When summing up both the continuum and anti-bound states' density, we obtain the static structure factor $S_2(k)$. The summed up densities and the previous result from figure 4.29 match with each other. The overall $S_2(k)$ decreases for larger k, as can be seen in figure 4.29 when varying the x-component of the momentum.

Moving on to the lower line of plots for the larger coupling $J = -0.6$, we obtain several qualitative differences. First, we have three anti-bound states which are clearly separated from the continuum, as can also be seen in figure 4.21 for $k = 0$. Next, the maximum intensity on the anti-bound states is increased with respect to the smaller coupling by around one order, while the overall density $S_2(k)$ only increases by a factor of three. Last, the density in the continuum has moved from the upper end of the continuum to the lower end of the upmost continuum and the other two continua.

Looking at the three anti-bound states, the lowest one has the highest intensity especially for small momenta. The other two states' intensities are on a similar scale, while the upmost state has its maximum intensity around $k = \pi$ and the middle state around $k = 0$. In contrast to the smaller coupling, we see no strong 'movement' of density from one anti-bound state to another. Instead the lowest one remains the state with the highest intensity for all investigated k. When looking at the densities at linear scale in the lower right figure, it gets clear that most of the overall intensity is located at the lowest anti-bound state. Overall, for rising interaction strength we find a shift in intensity from the continua to the anti-bound states while the overall density increases as well. The shift in intensity could probably take place at the upper end of the upmost continuum, where the high intensity line for $J = -0.4$ vanishes for $J = -0.6$, while the third anti-bound state forms out of the continuum with a high overall intensity. We have to keep in mind that we are in the regime of intersecting 1QP and 2QP for the large coupling, so especially for the lower continuum there may be a higher overall density because of possibly interactions with the upper 1QP band which has a way higher density than the total 2QP channel.

4.3 Comparison to density matrix renormalization group (DMRG) data

At the end of the discussion section, we want to combine our results from 1QP and 2QP to compare it to data calculated by Gohlke, Moessner and Pollmann [14]. As mentioned in the model section 2.2, they investigated the same model as we do in this thesis using the (infinite) density matrix renormalization group ((i)DMRG) method. The rough idea of DMRG is finding the ground state of a given system by iteratively reducing the effective dimensionality of the problem [54, 55]. Using this method they were able to characterize the phase diagram (as discussed in section 2.2) by finding the phase transition parameters and characteristic properties of the phases. In the obtained phases they studied the dynamical structure factor varying the parameters over a wide range. As we are restricted to the polarized phase, we will stick to the comparison of the dynamical structure factor in the polarized phase, as plotted in [14, figure 7]. The main focus will lie on proving or disproving a statement made at the end of section IV.B in their paper regarding a line of high intensity at the upper edge of the investigated spectrum. By examining the behavior of this line of intensity for varying parameters, they proposed that the origin of this feature could be an anti-bound state in the two quasi-particle sector. As we have all needed methods at hand (and already found and examined anti-bound states for some parameters), we will try to find this feature in our calculations and classify it.

First, we have to express the used parameter values for the given plot in our units. Taking the 1/2 factor for the spin operators and the different normalization constant into account, we obtain the relation

$$J = -\frac{h \cdot K_{\mathrm{p}}}{2h_{\mathrm{p}}} \,, \tag{4.3.1}$$

where the index p indicates the coefficients of the Gohlke paper. All parameters are chosen uniformly, meaning $J := J_x = J_y = J_z, h := h_x = h_y = h_z$. Inserting the parameter values, we obtain a coupling of $J \approx -0.86$ for our standard parameter $h = 1$, when taking figure 7 (a) of the paper. The other plots in the paper correspond to larger Kitaev-couplings J being closer to the phase transition to the intermediate phase. For the following discussion, we will stick to the $J \approx -0.86$ case, as we are losing quality for larger perturbations.

As discussed in section 3.4 and 4.2.2, we run into limitations for large perturbations. This starts with the mathematical aspect of calculating a perturbation series which has increasing errors when only investigating the series up to a finite order and for larger perturbation values. We deal with this problem by extrapolating the obtained series, as already done in the previous discussion. Furthermore, we found the intersection of different quasi-particle sectors as a physical aspect of inaccuracy, as we neglect all kind of interactions between the different particle channels. For this problem, we have not introduced a method to deal with it or measure the error. We can only state that the neglected interaction takes place at the lower end of the 2QP continuum which should have only minor effects on physics being energetically far away.

A further comment on the extrapolations: For the following plots we will use the dlog-Padé results for the two 1QP bands as we have calculated the bare series of these bands. In contrast, the 2QP energies are only given as floating numbers, as the diagonalization of a large distance matrix M_{dist} is way heavier to diagonalize when having series as entries in M_{dist}. Because of that, we insert the concrete coupling J into M_{dist} before diagonalizing the matrix. As a result of this work-around, we have no bare series where we can perform dlog-Padés on. So, the calculated 2QP physics may be of poorer quality than those of 1QP.

Before comparing the spectral densities, we take a look at the quality of the dispersion for the coupling of interest. As explained in the last paragraph, we mainly have to focus on the quality of the dlog-Padés for the two 1QP bands, as we have no extrapolations of the 2QP energies. To get a rough idea of the quality of the 2QP continua, we use the free particle approximation with the extrapolated 1QP bands to examine the difference between the edges of the continua in the approximation and the 2QP diagonalization. In contrast to section 4.2.1 (where we used the bare series for FPA), there should occur a difference between the two ways of calculation. For the anti-bound states we inspect the dependance of the chosen maximum order for the entries of M_{dist}. With this we get a rough estimate of the quality of the obtained energies. Nonetheless, we expect the maximum order being the most accurate result. So, we have to be careful when drawing conclusions of the overall quality of the results of the anti-bound states.

The result is plotted in figure 4.31. We use the same path in momentum space, as used in the Gohlke paper, varying k_x and setting $k_y = 0$, as done in several plots in the pervious discussion. On the left side the combined dispersion of 1QP and 2QP is plotted. For the 1QP bands and the free particle approximation, we use extrapolations to increase the quality. We obtain a very high quality of the lower 1QP band as already investigated in detail in figure 4.5 for $k = 0$. In contrast, the results of the upper 1QP band are of way lower quality, as can be seen by the standard deviation and the non-smooth behavior at some points. We identify this spreading of the extrapolants with the intersection of the upper 1QP band with the 2QP continuum. For the used coupling the upper band lies fully inside of the 2QP continuum. The 2QP continuum is calculated both with the obtained extrapolated 1QP dispersion and directly by diagonalizing M_{dist}. As proposed in the last paragraph, the two solutions do not fit, as we only extrapolated the 1QP bands and used different maximum orders. To keep the plot simple, we only plotted the maximum of the upmost continuum

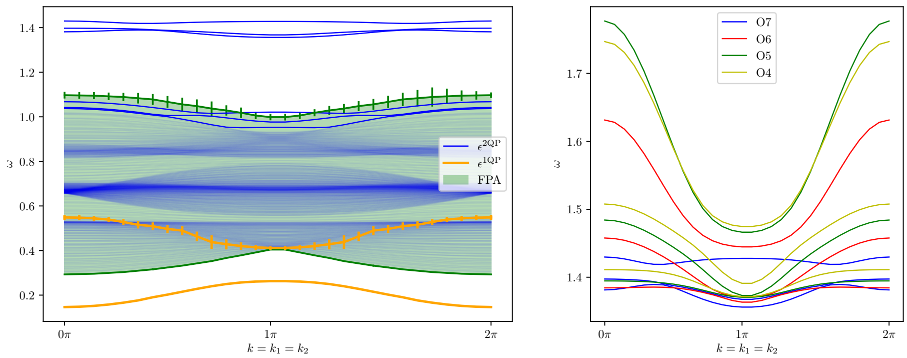

Figure 4.31: The dispersion of 1QP and 2QP for $J = 0.86$ and $h = 1$ is plotted. The momentum is varied in the x-component in the range of one period, by setting $k_1 = k_2$. The chosen parameters match with those of the Gohlke paper [14, figure 7]. On the left side, the eigenvalues of 1QP are plotted in orange color. The 2QP continuum is calculated by using the free particle approximation and diagonalizing the distance matrix M_{dist}. Because of calculation times, we calculate the free particle approximation using only the plotted 1QP path, so the range of the complete approximation may be wider. The eigenvalues of M_{dist} are plotted in light blue lines. Both for the 1QP bands and the free particle approximation, we use the results of the dlog-Padé extrapolants to obtain a higher quality of results. In the right plot we vary the maximum order for the diagonalization of M_{dist} for the anti-bound states. This serves as a rough estimate of the dependence of the obtained results of the actual maximum order.

and the minimum of the lowest one. Nonetheless, we can roughly identify the intersection of the three continua in the diagonalization data. We observe a very good agreement of the two results for the lower end of the continuum. This agrees with the high quality of the lower 1QP band, resulting in a low discrepancy of the bare series we use in 2QP and the extrapolated series we use in 1QP. In contrast, the upper edge results differ quite a bit. The reason lies both in the low quality of the dlog-Padés and the different maximum order of the 1QP and 2QP calculations, as we used order 8 for 1QP and order 7 for 2QP.

Far away from the continua, we observe the three anti-bound states, as expected. All three states show almost no dispersive behavior (no k-dependence) for the calculated order. This follows roughly the overall form of the anti-bound states we already investigated for smaller couplings, as in figure 4.19. To get a better estimate of the results' quality, we have plotted the energy of the three anti-bound states for different orders, as explained above. We observe an overall trend to lower energies, while the upper state varies most and the lower least in energy. Especially the upmost state changes qualitatively, as it starts from a strongly dispersive behavior in lower order, having the minimum at $k = \pi$. Because the band decreases fastest at the ends of the plotted momentum range, the k-dependance of the band decreases drastically. As another trend, the three states move closer together for increased order. While we can not get reliable data of the quality of the anti-bound states, we can state nonetheless that the three states will most probably stay in this region of energy, even when going to higher (and more accurate) order. Furthermore, they might be even closer together as predicted by our final order calculations, as the trend goes towards smaller distances when increasing the maximum order. When investigating the corresponding eigenvectors of the anti-bound states, we obtain a 'swapping' of

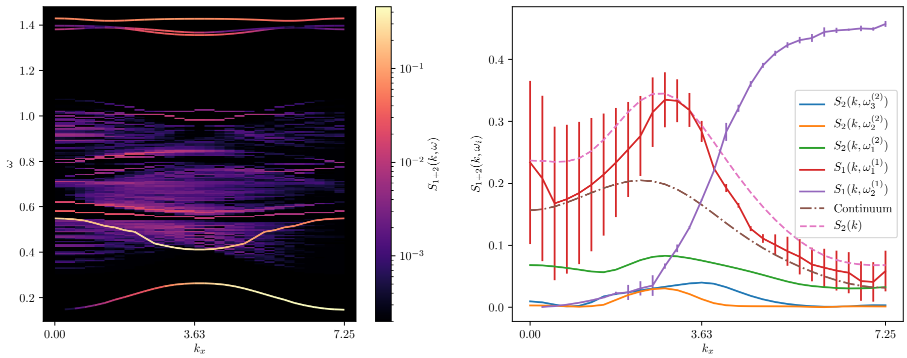

Figure 4.32: Dynamical structure factor for the same set of parameters as for [14, figure 7] being $h = h_x = h_y = h_z$ and $J = -0.86$. The spectral density is plotted for different momenta by varying k_x and setting $k_y = 0$, as done in the Gohlke paper. On the left side the energy of the 1QP and 2QP states is plotted on the y-axis and the spectral density for the single states is given in color code. For the continua, we rasterize the spectrum in energy-slices and sum up the density of all states lying within this slice. For more information, see the main text. On the right side the spectral density is plotted directly for the anti-bound states, the 1QP states, and the total density of all continua. The static structure factor is plotted in a dashed pink line. For 1QP, we use dlog-Padé extrapolations to improve the results. For clear view, the error bars are dropped for the sum of all densities, as it is directly connected to the errors of the constituents.

the order (not shown). As found in figure 4.23, the state with the highest energy has no phase difference for the different distances. For the larger coupling, this state has the lowest energy of the three states. In agreement to the lower couplings, all three states consist almost only out of states with distance one.

A last feature, we shortly want to mention, is the formation of another three anti-bound states directly above the continuum. One of the three states seems to be completely separated from the continuum—or at least for the investigated momenta—while the other two emerge out of the continuum only for momenta around $k = \pi$. The corresponding eigenvectors focus more on states with small distances, qualitatively different from the continuum-states we obtained in figures 4.23 and 4.25. Unlike the first three anti-bound states, the amplitude on distance $|\delta| = 1$ is comparably small in contrast to $|\delta| = 2$. So, the driving force may be the interaction of states with distance two. This would match to the number of three possible states with distance two, which are not translational invariant. It would be interesting to further analyze these three states and confirm the driving force. This remains challenging as all three states lie almost complete within the continuum obtained by the free particle approximation, which shows the limitations of the discussion with these large couplings.

After discussing the bare dispersion of 1QP and 2QP, we move on to the dynamical structure factor in figure 4.32. As for all other dynamical structure factors, the figure is divided up into two plots, where the left shows the actual spectral density as color code mapped onto the energies of the respective states and the right one concentrates on the spectral density. We again mention that the left density scale is logarithmic, while the right one is linear to prevent confusion. As for the energy, we have extrapolated the 1QP densities using dlog-Padés to increase the quality. Starting with the analysis of the absolute intensity, we find the two 1QP bands to carry the largest density. As for the smaller coupling case in figure 4.15, we obtain a shift of the intensity from the higher to the lower band for rising momenta k. The obtained density for the upper 1QP band is of comparable bad quality, as the standard deviation gets extremely large. Again, we can argue that the intersection between the state and the 2QP continuum is the reason for that. This explanation fits to the good quality of the calculated density of the lower band. As discussed in section 4.1.2, the intensity of the lower band drops totally for small k-values. All these findings—as well as the energy of the two bands—match to those of the Gohlke paper, qualitatively. Nonetheless, we have to state that the absolute intensities do not match. This might be because of a different normalization during the different types of calculations, where the paper ends up with broadened lines, while our results are δ-peaks in the energy regime.

Going on to the 2QP density, we first obtain an overall comparable weight to the 1QP sector, as we already found out in figure 4.12. For small k-values the portion of the 2QP weight to the overall weight is larger than for rising momenta. In contrast to the smaller 2QP densities investigated before in figure 4.30, the density distribution shifted slightly away from the anti-bound states to the overall continuum. Nonetheless, the intensity on the anti-bound states stays in the same order of magnitude as the 1QP bands. The obtained continuum itself stays comparably featureless, as the complete continuum shows an intensity of the same order of magnitude. Apart from this uniform intensity, there seem to be a few lines of higher intensity, as one lies a little bit above the upper 1QP band and one at around $\omega \approx 0.8$. These lightly highlighted lines can also be observed in the figure of the paper. Interestingly, the end of the 2QP continuum seems to match comparably well at $\omega \approx 1$, even though the quality of the upper edge is not quite good, as can be seen when comparing it to the free particle approximation in figure 4.31. This may be because the higher end of the continuum has a way lower intensity, as we can see some small features in the figure of the paper above $\omega \approx 1$ which could also come from the 3QP sector.

Lastly, getting to the three anti-bound states, the maximum in intensity has shifted from the lowest state to the upper one. This shift may be explained by the obtained shift of the states with respect to the eigenvectors' structure, as mentioned before. For all momenta, the upmost state features the highest intensity. All three anti-bound states have their maximum in intensity around $k_1 = k_2 = \pi$. When going to larger momenta, the overall intensity on all three states decreases and settles at lower intensities than at $k = 0$. When comparing the anti-bound states to the feature found in the paper, we first have to state the apparent different number of visible and distinguishable states, as the plot in the paper only features one line of high intensity. On the other side, the three obtained states match considerably well in energy to the high-intensity line in the paper. The upmost anti-bound states which features most of the intensity, fits quite well in energy although the dispersive behavior does not fit to that of the paper. As the two lower states, the feature in the paper bends down to a small dip at $k_1 = k_2 = \pi$, while the upper state bends upwards. So, the structure matches best with the two lower states. Also the decreasing intensity of all states for larger k values fits to the intensity line. The mismatch of only one visible line in the paper could also be explained by the line broadening of the DMRG paper, due to their method. If we would perform the same broadening of our δ-peaked structure, the results will be more similar. So, we can conclude with high confidence that the assumption having found an anti-bound state feature for 2QP, as made in the paper, is true. We can qualitatively reproduce the overall dynamical structure factor to quite good accuracy, especially for the 1QP sector. Obtaining a similar structure for the upper 1QP band furthermore affirms our made assumption of no interactions between the quasi-particle channels. Nonetheless, this may be the reason for quantitative differences, in addition to the finite perturbation order. It may be interesting to further investigate the behavior of the three anti-bound states and if we can deduce a further concentration on the state in the middle or find another explanation, as a further reduction of distances between the three states, as observed in figure 4.31. As a next step it also would be interesting to compare the results quantitatively, as we miss the absolute intensities by around one order, and for more different parameter values, especially for those with a smaller perturbation.

Chapter 5

Conclusion

We started this thesis with a motivation for simplifying complicated systems (or also not so complicated looking systems) involving a large number of interacting particles, by focusing on limiting cases to reduce the degrees of freedom and thus simplify the complexity of the problem. For our investigated model—the Kitaev honeycomb-model in a magnetic field—we introduced several methods which applied a number of assumptions onto the general model to make it possible to calculate physical quantities. By using the translational invariance induced by the structure of the lattice, we found the total momentum being a conserved quantity (see section 3.1). Most importantly, we used the pCUT method to transform the original Hamiltonian into a block diagonal form, where the number of quasi-particles is conserved. For doing so, we restricted the parameters to $h \gg J$, to guarantee acting in the polarized phase by applying the Kitaev-terms as a small perturbation (section 3.2). Furthermore, we introduced the free particle approximation in section 3.3 as a tool to approach the 2QP continuum by neglecting all interactions between the two particles, used extrapolations to improve the quality of our obtained series (see section 3.4), motivated by the changed structure of the chosen extrapolations, and investigated several limiting cases in the discussion, as the Compass model, which we solved analytically. All these methods and restrictions made it possible to investigate and partially solve the feature-rich model and understand it in more detail.

As a main advantage of pCUT, we were able to discuss physical quantities divided up into different quasi-particle channels in sections 4.1 and 4.2. Using the block-diagonal form, we studied the energy spectrum and spectral quantities for one and two quasi-particles, separately. In the discussion we mainly focused on the dispersion and gap of the Hamiltonian and spectral quantities of the observable $O = \sigma^z$. We were able to reproduce the findings regarding the 1QP gap of [47], which used the same pCUT method, and generalize it to different magnetic fields and non-uniform Kitaev couplings. Generally, we found a strong asymmetry of the dispersion under a sign-swap of the Kitaev-parameters J_α. While the gap closes for uniform antiferromagnetic Kitaev-couplings in the order of $J \approx 1$ and can be approximately fetched by extrapolations, the gap closing for ferromagnetic couplings can not be determined reasonably. This finding matched with [14, 17], as the phase transition between the polarized phase and the Kitaev-phases happens for way larger $|J|$ when having ferromagnetic couplings. Investigating two different magnetic fields, we generally found a slower closing of the gap—again being able to extrapolate the phase transition only for antiferromagnetic J. For the limiting case of setting one of the three Kitaev-couplings to zero, we obtained the Compass model, which features a phase transition for arbitrary small magnetic fields. For this case we were able to compare the perturbative results to an analytical solution, proving the good convergence of the pCUT series.

By analyzing the spectral weight of the observable O, we were able to motivate the consideration of the 2QP sector, as this sector starts to play a non-negligible role for rising Kitaev interactions when calculating spectral quantities, which can be examined in experiments. Investigating the spectrum of the 2QP energies, we were able to obtain a continuum of energies using 2QP calculations and the free particle approximation for two independent quasi-particles. Using this connection between 2QP and 1QP, we were able to understand the 2QP continua as a combination of two independent quasi-particles having an individual energy determined by the 1QP dispersion. The main focus in the 2QP spectrum laid on the possible formation of (anti)-bound states. As we focused on anti-ferromagnetic couplings, we only obtained the formation of anti-bound states, emerging out of the upper edge of the continuum. By discarding several types of processes and orders we found some key properties of the anti-bound states:

1. We find three anti-bound states emerging one after another out of the upmost continuum (see figures 4.19, 4.21).
2. To form an anti-bound state, we need to include at least order 2 or higher. For order 1 we find no anti-bound states, regardless of the magnitude of the Kitaev-coupling (see figure 4.24).
3. We find no anti-bound state (at least for vanishing momentum), when only using small couplings. The first anti-bound state begins to form for finite Kitaev couplings and first emerges at $k = \pi$ for the two investigated paths in momentum space (see figures 4.19, 4.20).
4. All three anti-bound states form out of a density-density interaction with the nearest neighbor. This means that the anti-bound states mainly consist of a superposition of states with two quasi-particles being next to each other. So, the number of three anti-bound states comes from the number of three nearest neighbor configurations in the honeycomb model (see figures 4.21, 4.22, 4.23).
5. The shape of the eigenvectors of the anti-bound states and the continuum differ qualitatively, as the anti-bound states mainly consist out of nearest neighbor configurations, while the states in the continuum spread over all possible distances (see figures 4.23, 4.25).

Even as the anti-bound states do not form for infinitesimal perturbations, we can nonetheless conclude the formation of three anti-bound states within good convergence of our perturbative approach. Although the next-neighbor density-density interaction is the driving factor of the anti-binding, at larger couplings also other types of correlations seem to play a role, as the anti-bounding effect decreases when only allowing density-density correlations. The possible formation of further anti-bound states using other correlations than the density-density for next-neighbored particles can not be verified or falsified, as the found effects occur at comparably large couplings. Nonetheless, it seems possible that further anti-bound states emerge for larger couplings.

Last, we investigated the spectral density of the 2QP regime. The overall weight of the 2QP channel is comparably small for small perturbations and can be neglected. In momentum space the static structure factor has the form of a tilted chessboard with alternating maxima and minima, following the direction of the lattice vector a_1. For larger couplings we found a shift of density from the 1QP to the 2QP channel, while the overall form of the static structure factor for 1QP and 2QP remains roughly the same, as discussed in figure 4.29. Within the 2QP channel, the density shifts for rising Kitaev couplings from the continuum to the three anti-bound states. For very large couplings—as discussed in section 4.3—a large part of the spectral density is found in the anti-bound states. Comparing the results for large perturbation with those of Gohlke et al. [14], we find a qualitative agreement of the data, especially for the 1QP spectrum. Even as the higher energies and density contribution does not match perfectly, we can nonetheless confirm the assumption of the paper that the anti-bound states in the 2QP sector inhibit a quite high spectral intensity and are located roughly at the proposed energy.

During the whole thesis, but especially for the comparison to [14], we faced the limits of the perturbative approach. This started with the bad quality of the determined point of gap-closing, as the phase transition (especially for ferromagnetic J) lies way outside of the convergence of our perturbative series. Even as we improved the quality of the results quite a bit by extrapolation techniques, we are not able to successfully determine the point of gap-closing. For the 2QP discussion we were not able to use the extrapolations—due to a more complex diagonalization—because we calculated the physical quantities as bare numbers and not as series, as done before for 1QP. We could improve the quality by calculating higher orders of the energies or spectral quantities. With a maximum order of 8 or sometimes even 6, we are several orders away from the accuracy which is achieved in other models where pCUT is applied [40, 48, 56–58]. The difference of the maximum order in contrast to other models, lies in the complexity of the investigated one. As the 2D structure combined with different couplings J_α results in a large variety of graphs, a graph-decomposition as done in other models seems not feasible to increase the maximum order [36]. Instead, we created different clusters depending on the different types of couplings as described in appendix A. We also tried to further subdivide the clusters by adding more different couplings (dividing each coupling J_α in two separate couplings alternating on the lattice) which did not improve the performance. It may be possible that the further separation of couplings may become beneficial, when calculating even higher orders, as also the done subdivision is only advantageous at higher orders.

Another limit is the intersection of the different quasi-particle channels for rising couplings. As we ignore all couplings between states with different particle number, we neglect all types of processes where the particle number does change (as originally desired by pCUT). This may lead to unphysical results in the area of intersecting QP channels. We found some evidence of these intersections by investigating the poles of dlog-Padés but are not able to estimate the 'magnitude' of the error we make, at the moment. It may be needed to re-implement the coupling between the 1QP and 2QP channels as a perturbation, to consider these processes and estimate the error of neglecting these processes.

Moving on to the possible next steps, a first improvement can be done in the calculation of the spectral density for the 2QP continuum. Due to limited time for the thesis, we concentrated on the anti-bound states and only estimated the density of the continuum by rasterizing through the finite set of states in the continuum obtained by diagonalizing the finite sized M_{dist}. By using the approach in [12, 41], we can calculate the dynamical structure factor by M_{dist}, which is applied iteratively onto the state $\mathcal{O}_{2,0}\left|0\right\rangle$ to obtain the needed coefficients for the density function. This would be a next step in comparing our results with those of the paper [14]. We also have to fix the difference in the absolute intensities between our results and those of the Gohlke paper to be able to investigate the quantitative agreement. In general, we could compare the results more closely and investigate other parameter values. Especially for lower Kitaev couplings, we expect our data to have a better quality, thus being able to discuss the results more closely. It also would be interesting to investigate the spectral properties of the anti-bound states in more detail. We were able to classify the anti-bound states very precisely but did not focus on the physical foundation of the strong spectral intensity for larger couplings. Probably we could find a key mechanism in the system leading to the observed density. In general, we could systematically enlarge the investigated parameter space. Up to now we have mainly focused on a uniform magnetic field and uniform couplings. Going to different limits could yield more insight in the 2QP properties.

On the technical side, it would be interesting to calculate the 2QP spectrum as a series, especially the anti-bound states. We did some approaches for a series-diagonalization of an arbitrary sized matrix but ran into problems when facing degenerate eigenvalues in first order. This phenomenon also leads to a divergence in the 1QP spectrum, which was solved by moving to diagonalizing single values. A robust solution to this problem would give more insight into the structure of the anti-bound states and would enable us to perform dlog-Padés onto them. Also the already mentioned implementation of couplings between 1QP and 2QP would be promising to understand the rising interaction between the different particle channels.

The Kitaev honeycomb model remains an interesting field of research. Even focusing only on the polarized phase, we found a variety of features in the 1QP and 2QP sectors. The detailed investigation of the anti-bound states gave us an intuitive picture, simplifying the rather complicated model with a huge number of interacting spins to two particles being closely connected to each other moving on the honeycomb lattice.

Appendix A

Creating clusters for pCUT-calculation

To be able to calculate the coefficients of the processes in equations 3.2.10 and 3.2.16, we have to define clusters, where we calculate the hopping on. We have already justified the restriction onto local processes by using the linked cluster theorem in section 3.2.2, and stated that we have to calculate the local processes on suitable large clusters. In the following chapter we will discuss the creation of these clusters in more detail. We will start with the requirements of the created clusters, followed by an algorithm established by [59], which we adapt to create the clusters automatically. Finally, we will introduce an optimization technique using the different coupling types of the Kitaev interaction.

A.1 Requirements of the clusters

We have met two different types of processes in this thesis where the calculation of coefficients using pCUT is needed. First, we introduced the calculation of hopping elements in equation 3.2.10 to obtain the energy levels of the corresponding quasi-particle sector. As the pCUT transformation is defined in such a way that the particle number is a conserved quantity for the Hamiltonian, we only have hoppings of the form where the bra and the ket state have the same number of quasi-particles in it. On the other side, the QP number is not conserved anymore for an arbitrary observable as discussed in section 3.2.4. As we restricted ourselves to processes at zero temperature, the ket state is always the ground state, while the bra state can have in principle an arbitrary number of quasi-particles in it, as can be seen in equation 3.2.16.

While we defined the processes arbitrarily, having general bra and ket states only with the restrictions discussed in the last paragraph, it is not possible to calculate the amplitudes between all possible states, as we have an infinite number of lattice sites in the thermodynamic limit. So, we first have to determine the possible (not vanishing) processes for a given order k. Using the linked cluster theorem, we know that only linked processes contribute to the final amplitude.

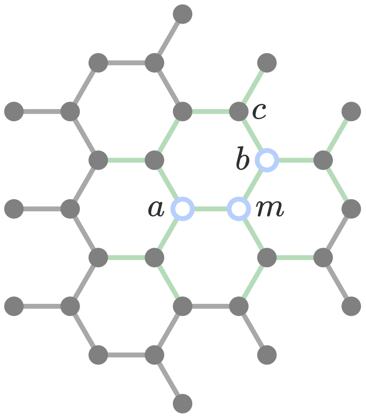

Figure A.1: Visualization of an exemplary hopping process. In this example a particle starting at site a moves to site b by an application of two T_0 operators, moving the particle along the sites $a \to m \to b$, marked with blue circled sites. The minimum order of this process is two. When calculating this hopping process in higher order, one has to enlarge the cluster for virtual processes. This is exemplary marked for order four in green bound color. We can find a maximum cluster for a given order k, where all optimized cluster lie within, when going k steps in all directions, as done for $k = 4$ with the complete visualized cluster, starting from site a.

This means that a (in principle possible) process where two particles are created far away from each other, will have no finite amplitude for finite perturbation order. More practically we examine an easy example of an 1QP particle hopping from an (arbitrarily chosen) site a to a site b as given in figure A.1. Using for example the hopping term in T_0 in equation 2.3.6, we can move the particle from site a to the intermediate site m. Applying another T_0 term moves the particle to the desired site b. Keep in mind, T_0 (and also the other T_α operators) being an infinite superposition of all possible next-neighbor interactions on the infinite lattice also including the term we used for this easy example. Because of that all possible other 'routes' between a and b are also taken by some of the operator terms. Nonetheless, the explained path $a \to m \to b$ is the shortest one and needs at least two applications of T_α. As the number of applied T_α operators is equal to the calculated order, we can conclude that the hopping $\langle b \mid H_{\text{eff}} \mid a \rangle$ starts at order two. Generalizing this idea, we define the contributing 1QP hopping processes:

Definition A.1. A 1QP hopping process $\langle i \mid H_{\text{eff}} \mid j \rangle$ starts to contribute at order d, where d is the minimum distance between the two sites. The distance is defined as the number of bonds between i and j in the graph G_{lat}, as defined in section 3.3.

For hoppings of a higher number of quasi-particles or the creation of quasi-particles during the process for the effective observable, we can generalize the above statement. For the following definition we use the fact that the higher particle number hopping terms are calculated for determining the H_n terms as defined in equation 3.2.7. As H_n only covers the processes of n correlated particles, we can conclude that all quasi-particles have to interact with each other, locally. We state:

Definition A.2.

1. An nQP hopping process $\langle i_1,\ldots,i_n \mid H_n \mid j_1,\ldots,j_n\rangle$ starts to contribute at order d, where d is the number of bonds of a minimum graph connecting all sites $i_1,\ldots,i_n,j_1,\ldots,j_n$ with each other.
2. A process $\langle i_1,\ldots,i_n \mid \mathcal{O}_{\text{eff}}^{T=0}(i) \mid 0\rangle$ starts to contribute at order d, where d is the number of bonds of a minimum graph connection all sites $i,i_1,\ldots,i_n$ with each other. The parameter i denotes the site where the local observable O is acting on, as defined in equation 4.1.7.

The minimum graph, as defined for determining the minimum order, can only directly be used to calculate the process in the given minimum order. When going to higher orders we have to take further virtual processes into account. Going back to our minimal example of the $\langle b \mid H_{\text{eff}} \mid a\rangle$ hopping, after the two sketched hoppings from a to b, further applications of T_α can for example create a second particle at c, move it some sites on the lattice and annihilate it in the end. So, we are ending with the same state $|b\rangle$, as we created and annihilated the virtual particle during the process. As this exemplary process can take place at all sites connected to the minimum graph, as given in the last definition, we have to expand the cluster used for calculation in all possible directions. The resulting cluster for order four is plotted in green bonds in figure A.1. For higher number of particles this enlargement for higher orders of the minimal cluster gets more complicated, as there can occur new graphs connecting all contributing sites which can not be accessed by enlarging the minimum graph of minimum order. To deal with this increasing complexity, we choose to use a brute-force algorithm to test all sub-clusters of a 'suitable large' finite cluster if they connect all contributing sites for the given order. The implementation follows the idea of Rücker in [59] and will be discussed in the next section. The 'suitable large' cluster can be chosen to connect one arbitrary chosen site a with all possible sites up to the given order, as sketched in figure A.1 for order four in gray bonds. As can be seen, the minimized cluster, sketched with green bonds, lies within the 'large' cluster.

A.2 Generating possible sub-clusters

As motivated at the end of the last section, for rising number of particles in the processes the creation of minimum clusters for calculation gets challenging. To circumvent the creation of a complicated algorithm for all possible clusters connecting the contributing sites, we use an algorithm written down in [59] to get all possible connected sub-clusters with k bonds of a given cluster $\mathcal{C}$. We denote the set of all found sub-clusters as $\mathcal{S}$. We sort out all clusters $s \in \mathcal{S}$ that do not match the requirements for the given process, namely connecting all contributing sites $l \in \mathcal{L}$, reading

$$\mathcal{S}_{\text{con}} := \{ s \in \mathcal{S} \mid \mathcal{L} \subset s \} , \tag{A.2.1}$$

where $\mathcal{L}$ is the set of all contributing sites as used in definition A.2 and $\mathcal{S}_{\text{con}}$ is the remaining set of clusters fulfilling the requirement. As we found a direct connection between the size of a cluster and the order of perturbation, a set in $\mathcal{S}_{\text{con}}$ represents a possible process in order k with the contributing sites $l \in \mathcal{L}$. Merging the remaining clusters as

$$\mathcal{C}_{\text{min}} = \bigcup_{s \in \mathcal{S}_{\text{con}}} s \tag{A.2.2}$$

give us the minimum cluster $\mathcal{C}_{\text{min}}$ for the calculation of the respective hopping element in order k. It remains to show the creation of the set of sub-clusters $\mathcal{S}$. We use a slightly modified algorithm for the creation of $\mathcal{S}$, for more information on the original algorithm, see [59].

First, before discussing the algorithm for itself, we define some object which will be used within it. First, we will use order k, which determines the size of the cluster. Additionally, we choose an (arbitrary) starting site $l \in L$, where L is the set of contributing sites. For the algorithm we define furthermore a sorted set B and a set F, which are empty at the start. We initialize the algorithm by inserting an arbitrary bond b of l (as defined in section 3.2.2) into $B = \{b\}$. The algorithm is performed iteratively with two possible types of steps, called 'step forward' or 'step backward'. A step forward is done if we can append a bond b' to B which is not yet in $B \cup F$ and is 'connected' to one of the bonds in B, meaning there exists a site with bonds b' and $\tilde{b} \in B$. If a step forward is not possible, we apply a step backward by removing the last inserted bond b' from B and add it to F, instead. Additionally, we check for bonds in F which were inserted at a moment where $|B|$ was larger than at the beginning of the step backward. All bonds which fulfill this condition are removed from F. After each step forward we check if $|B| = k$ and all sites in L are connected to at least one of the bonds in B. If this is the case, we can define a set of sites

$$s := \{c \in \mathcal{C} \mid c \text{ connected to at least one } b \in B\}\,, \tag{A.2.3}$$

where every site has at least one bond in B. As s fulfills all requirements for the above used sub-clusters, we add s to $\mathcal{S}$. The algorithm continues until $B = \emptyset$. If this is the case, another bound of l is inserted into B and the algorithm is started again. After inserting all bounds of l, we have found all connected sub-clusters of $\mathcal{C}$ which connect the sites in L. The step forward explores the possible connected configurations, starting at the site l, and the step backward resets the configuration partially if one part of the configuration space is fully explored. Some of the calculated sub-clusters s are visualized in figure A.2. Again, we use the example started in figure A.1 of hoppings in order four from site a to b. Merging all visualized cluster and the remaining nine which are not shown, we obtain the final cluster $\mathcal{C}_{\text{min}}$ as plotted with green bonds in figure A.1.

A.3 Minimizing clusters

The minimization of the clusters on which we perform calculations is crucial for optimizing the computation-time, as the dimensionality of the system grows exponentially with the size of the cluster. With the last section we have found the minimum cluster $\mathcal{C}_{\text{min}}$ for the computation of specified processes with

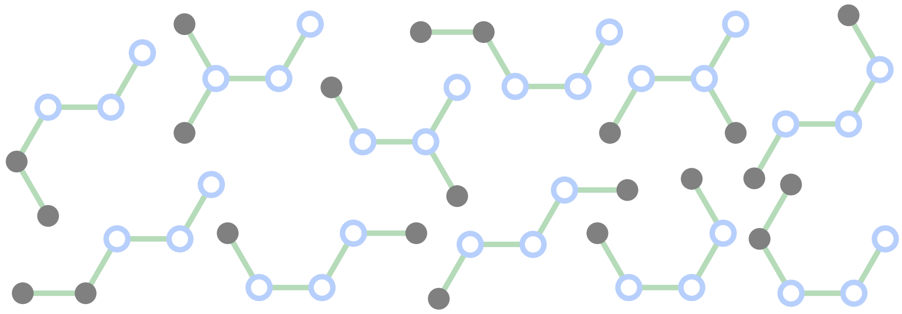

Figure A.2: A selection of sub-graphs calculated by the algorithm for a 1QP hopping as defined in figure A.1 for order four. When combining all 21 graphs we obtain the cluster for calculation as plotted in green bonds in figure A.1.

pCUT, as classified in definition A.2. The idea of this last section is a further dimensionality-reduction of the single computations by splitting the calculation of a single process into a number of smaller tasks. So, we trade the complexity of single pCUT calculations with the number of them.

For the creation of $\mathcal{C}_{\text{min}}$, we considered the perturbation order to restrict the number of bonds. In order to to minimize the size further, we will also take the particular combination of perturbation parameters J_x, J_y, J_z into account. This is motivated by the resulting series in equations 3.2.6 and 3.2.15, where each summand is proportional to a specific combination of those parameters varying in the exponent. So, for calculating one of the summands, we can also use the information of the exponent of the parameters in addition to the perturbation order. We split order k into $k = k_x + k_y + k_z$, where the k_α are defined as the exponents of J_x, J_y, J_z, respectively.

The changes we have to apply to the algorithm introduced in section A.2 are minimal. We leave the step forward and backward as it is and only modify the check after one step forward. As we now track the order of all three perturbations, we do not check $|B| = k$, but instead if $|B|_\alpha = k_\alpha$ for $\alpha \in \{x, y, z\}$, where $|B|_\alpha$ denotes the number of α-bonds in B. Again, the following creation of the set of sites connected to the bonds stays the same. Now, $\mathcal{S}$ consists out of clusters which fulfill the given perturbation order for each of the three perturbation parameters, as defined above. The resulting clusters are plotted in figure A.3 for our example of the above 1QP hopping. In contrast to before, some combinations of k_α are not possible as a connected cluster. For example for the given lattice, there exists no cluster with two x-bonds and no y- and z-bonds. Nonetheless, terms like J_x^2 can occur when acting twice on the same bound, thus restricting our needed cluster to only one x-bond. When implementing an algorithm which extracts the correct terms of a calculated pCUT series, one has to consider these terms which can be calculated with clusters of 'smaller' size than the exponents of the respective term. Another example is the left cluster of figure A.3, where the cluster stays the same when increasing k_z to higher values, while fixing $k_x = k_y = 1$.

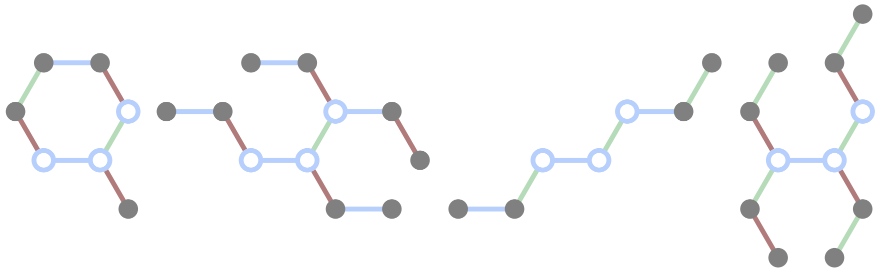

$k_x = 1, k_y = 1, k_z = 1$ $k_x = 2, k_y = 1, k_z = 1$ $k_x = 2, k_y = 2, k_z = 0$ $k_x = 1, k_y = 2, k_z = 1$

Figure A.3: Exemplary minimization of the green cluster in figure A.1 in order four. To stress the role of the different couplings J_α, the bonds are colored with respect to the different interactions. For order four we obtain four different graphs, with different k_α values determining the number of each of the different couplings for each individual hopping process. As the particle has to move from site a to site b, k_x and k_y have to be larger than zero. The left graph is a special case, as $k_x = k_y = k_z = 3$ is smaller than four. In fact the cluster will not change in size when fixing k_x, k_y and increasing k_z further. So, we can use the left cluster for all calculations of terms of the discussed form.

Appendix B

Hopping amplitudes

At the heart of the pCUT calculations lies the computation of single hopping terms. These are calculated in the form of equation 3.2.10 by using the effective Hamiltonian up to a given order, the needed states for the desired hopping, and a finite cluster which is chosen 'large enough' as described in more detail in appendix A. For the discussion of the 1QP and 2QP dispersion, we need to calculate all possible hoppings of one and two particles up to the given order, respectively. As mentioned in section 3.2.3, the obtained results depend on the cluster and have to be modified to receive the thermodynamic coefficients for the effective Hamiltonian. These corrections come in, iff a quasi-particle in the ket-state is not moved during the hopping process. For more information see section 3.2.3. For the following hoppings, we have already performed the subtractions to obtain the correct thermodynamic series. This means that all presented coefficient series for hoppings which include non-moving particles are not the bare result from the Solver.

As we have calculated the series for the effective Hamiltonian and the effective observable with respect to three different perturbation parameters J_x, J_y, J_z, the series get large and confusing quite fast when increasing the maximum order. To keep the printed series (comparably) compact we restricted all series to order 4 and to 4 decimal places. Hopefully, this serves nonetheless as a starting point for comparing results. Another excellent source for single hopping terms in pCUT for the uniform coupling case $J_x = J_y = J_z$, can be found in the master's thesis of Fey [47]. As the number of 2QP hoppings for the dispersion and the observable rises very fast for even small orders (around 1000 hoppings for order 4), we do not print them in the following.

B.1 One-particle hoppings

In the following we print the obtained series for the hoppings up to order 4. As mentioned above, we have already corrected the local hopping term in the form of equation 3.2.12. The series are denoted as $p_{x,y,z}$ as a short hand for the abstract notation $c_{i\to j}$ used in the methods chapter. The subscript variables

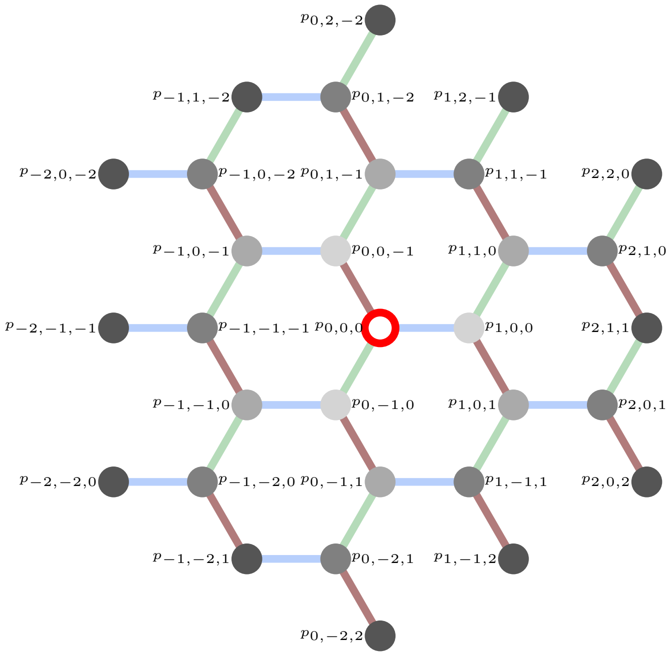

Figure B.1: Denomination of the honeycomb sites. The sites are named in the form $p_{x,y,z}$ where the indices give the minimum number of bonds of the respective bond-type between this site and the origin-site marked red. The different colors of the sites visualize the total distance to the original size which directly corresponds to the minimum non-vanishing order in the perturbation series.

x, y, z determine the position j of the quasi-particle in the bra state in relation to the starting position i. Therefore, the three variables denote the minimum number of bonds between i and j of their respective type. So, the local hopping is denoted as $p_{0,0,0}$. As further guide, the positions are printed in figure B.1. The terms within the single series are sorted first varying the J_z exponent, followed by the J_y and J_x exponent. Due to the general form of the series, we can identify the dependence of the needed exponents with the connecting path between the starting site i and the final site j. Taking $p_{1,0,1}$ as one example, we notice that all summands contain the factor J_xJ_z. This corresponds to the shortest connection between the two sites, which includes a x- and a z-bond. In the same way we can analyze the other terms. This is the reason why the terms are drastically reduced in complexity when moving i, j further apart from each other, as the 'prerequisites' for each summand get more demanding.

$$\begin{aligned}
p_{0,0,0} = &+0.1925J_z + 0.0556J_z^2 - 0.0143J_z^3 - 0.0015J_z^4 + 0.1925J_y - 0.1111J_yJ_z \\
&- 0.0071J_yJ_z^2 + 0.0267J_yJ_z^3 + 0.0556J_y^2 - 0.0071J_y^2J_z - 0.0298J_y^2J_z^2 \\
&- 0.0143J_y^3 + 0.0267J_y^3J_z - 0.0015J_y^4 + 0.1925J_x - 0.1111J_xJ_z - 0.0071J_xJ_z^2
\end{aligned}$$

$$
\begin{aligned}
&+ 0.0267 J_x J_z^3 - 0.1111 J_x J_y + 0.1711 J_x J_y J_z - 0.0432 J_x J_y J_z^2 - 0.0071 J_x J_y^2 \\
&- 0.0432 J_x J_y^2 J_z + 0.0267 J_x J_y^3 + 0.0556 J_x^2 - 0.0071 J_x^2 J_z - 0.0298 J_x^2 J_z^2 \\
&- 0.0071 J_x^2 J_y - 0.0432 J_x^2 J_y J_z - 0.0298 J_x^2 J_y^2 - 0.0143 J_x^3 + 0.0267 J_x^3 J_z \\
&+ 0.0267 J_x^3 J_y - 0.0015 J_x^4 \\
p_{0,-1,0} &= -0.1925 J_y - 0.037 J_y J_z + 0.0187 J_y J_z^2 + 0.0082 J_y J_z^3 + 0.0071 J_y^2 J_z \\
&- 0.0091 J_y^2 J_z^2 - 0.0071 J_y^3 + 0.0089 J_y^3 J_z - 0.037 J_x J_y + 0.0428 J_x J_y J_z \\
&- 0.0197 J_x J_y J_z^2 + 0.0071 J_x J_y^2 - 0.0247 J_x J_y^2 J_z + 0.0089 J_x J_y^3 + 0.0187 J_x^2 J_y \\
&- 0.0197 J_x^2 J_y J_z - 0.0091 J_x^2 J_y^2 + 0.0082 J_x^3 J_y \\
p_{0,0,-1} &= -0.1925 J_z - 0.0071 J_z^3 - 0.037 J_y J_z + 0.0071 J_y J_z^2 + 0.0089 J_y J_z^3 + 0.0187 J_y^2 J_z \\
&- 0.0091 J_y^2 J_z^2 + 0.0082 J_y^3 J_z - 0.037 J_x J_z + 0.0071 J_x J_z^2 + 0.0089 J_x J_z^3 \\
&+ 0.0428 J_x J_y J_z - 0.0247 J_x J_y J_z^2 - 0.0197 J_x J_y^2 J_z + 0.0187 J_x^2 J_z \\
&- 0.0091 J_x^2 J_z^2 - 0.0197 J_x^2 J_y J_z + 0.0082 J_x^3 J_z \\
p_{1,0,0} &= -0.1925 J_x - 0.037 J_x J_z + 0.0187 J_x J_z^2 + 0.0082 J_x J_z^3 - 0.037 J_x J_y \\
&+ 0.0428 J_x J_y J_z - 0.0197 J_x J_y J_z^2 + 0.0187 J_x J_y^2 - 0.0197 J_x J_y^2 J_z \\
&+ 0.0082 J_x J_y^3 + 0.0071 J_x^2 J_z - 0.0091 J_x^2 J_z^2 + 0.0071 J_x^2 J_y \\
&- 0.0247 J_x^2 J_y J_z - 0.0091 J_x^2 J_y^2 - 0.0071 J_x^3 + 0.0089 J_x^3 J_z \\
&+ 0.0089 J_x^3 J_y \\
p_{-1,-1,0} &= +(0.0093 + 0.016i) J_x J_y + (0.0125 + 0.0093i) J_x J_y J_z \\
&+ (-0.0086 - 0.0097i) J_x J_y J_z^2 + (0.0036 - 0.0123i) J_x J_y^2 \\
&+ (-0.0079 + 0.0048i) J_x J_y^2 J_z + (0.0029 - 0.0004i) J_x J_y^3 \\
&+ (0.0036 - 0.0123i) J_x^2 J_y + (-0.0079 + 0.0048i) J_x^2 J_y J_z \\
&+ (-0.0027 + 0.0036i) J_x^2 J_y^2 + (0.0029 - 0.0004i) J_x^3 J_y \\
p_{-1,0,-1} &= +(0.0093 - 0.016i) J_x J_z + (0.0036 + 0.0123i) J_x J_z^2 + (0.0029 + 0.0004i) J_x J_z^3 \\
&+ (0.0125 - 0.0093i) J_x J_y J_z + (-0.0079 - 0.0048i) J_x J_y J_z^2 \\
&+ (-0.0086 + 0.0097i) J_x J_y^2 J_z + (0.0036 + 0.0123i) J_x^2 J_z \\
&+ (-0.0027 - 0.0036i) J_x^2 J_z^2 + (-0.0079 - 0.0048i) J_x^2 J_y J_z \\
&+ (0.0029 + 0.0004i) J_x^3 J_z \\
p_{0,-1,1} &= +(0.0093 - 0.016i) J_y J_z + (0.0036 + 0.0123i) J_y J_z^2 + (0.0029 + 0.0004i) J_y J_z^3 \\
&+ (0.0036 + 0.0123i) J_y^2 J_z + (-0.0027 - 0.0036i) J_y^2 J_z^2 + (0.0029 + 0.0004i) J_y^3 J_z \\
&+ (0.0125 - 0.0093i) J_x J_y J_z + (-0.0079 - 0.0048i) J_x J_y J_z^2 \\
&+ (-0.0079 - 0.0048i) J_x J_y^2 J_z + (-0.0086 + 0.0097i) J_x^2 J_y J_z \\
p_{0,1,-1} &= +(0.0093 + 0.016i) J_y J_z + (0.0036 - 0.0123i) J_y J_z^2 + (0.0029 - 0.0004i) J_y J_z^3 \\
&+ (0.0036 - 0.0123i) J_y^2 J_z + (-0.0027 + 0.0036i) J_y^2 J_z^2 + (0.0029 - 0.0004i) J_y^3 J_z \\
&+ (0.0125 + 0.0093i) J_x J_y J_z + (-0.0079 + 0.0048i) J_x J_y J_z^2 \\
&+ (-0.0079 + 0.0048i) J_x J_y^2 J_z + (-0.0086 - 0.0097i) J_x^2 J_y J_z \\
p_{1,0,1} &= +(0.0093 + 0.016i) J_x J_z + (0.0036 - 0.0123i) J_x J_z^2 + (0.0029 - 0.0004i) J_x J_z^3 \\
&+ (0.0125 + 0.0093i) J_x J_y J_z + (-0.0079 + 0.0048i) J_x J_y J_z^2 \\
&+ (-0.0086 - 0.0097i) J_x J_y^2 J_z + (0.0036 - 0.0123i) J_x^2 J_z + \\
&(-0.0027 + 0.0036i) J_x^2 J_z^2 + (-0.0079 + 0.0048i) J_x^2 J_y J_z \\
&+ (0.0029 - 0.0004i) J_x^3 J_z \\
p_{1,1,0} &= +(0.0093 - 0.016i) J_x J_y + (0.0125 - 0.0093i) J_x J_y J_z \\
&+ (-0.0086 + 0.0097i) J_x J_y J_z^2 + (0.0036 + 0.0123i) J_x J_y^2 \\
&+ (-0.0079 - 0.0048i) J_x J_y^2 J_z + (0.0029 + 0.0004i) J_x J_y^3 \\
&+ (0.0036 + 0.0123i) J_x^2 J_y + (-0.0079 - 0.0048i) J_x^2 J_y J_z \\
&+ (-0.0027 - 0.0036i) J_x^2 J_y^2 + (0.0029 + 0.0004i) J_x^3 J_y
\end{aligned}
$$

$$
\begin{aligned}
p_{-1,-2,0} &= -0.0009 J_x J_y^2 - 0.0002 J_x J_y^2 J_z + 0.0007 J_x J_y^3 - 0.0045 J_x^2 J_y^2 \\
p_{-1,-1,-1} &= +0.0036 J_x J_y J_z - 0.0015 J_x J_y J_z^2 - 0.0015 J_x J_y^2 J_z - 0.0111 J_x^2 J_y J_z \\
p_{-1,0,-2} &= -0.0009 J_x J_z^2 + 0.0007 J_x J_z^3 - 0.0002 J_x J_y J_z^2 - 0.0045 J_x^2 J_z^2 \\
p_{0,-2,1} &= -0.0009 J_y^2 J_z - 0.0045 J_y^2 J_z^2 + 0.0007 J_y^3 J_z - 0.0002 J_x J_y^2 J_z \\
p_{0,1,-2} &= -0.0009 J_y J_z^2 + 0.0007 J_y J_z^3 - 0.0045 J_y^2 J_z^2 - 0.0002 J_x J_y J_z^2 \\
p_{1,-1,1} &= +0.0036 J_x J_y J_z - 0.0111 J_x J_y J_z^2 - 0.0015 J_x J_y^2 J_z - 0.0015 J_x^2 J_y J_z \\
p_{1,1,-1} &= +0.0036 J_x J_y J_z - 0.0015 J_x J_y J_z^2 - 0.0111 J_x J_y^2 J_z - 0.0015 J_x^2 J_y J_z \\
p_{2,0,1} &= -0.0009 J_x^2 J_z - 0.0045 J_x^2 J_z^2 - 0.0002 J_x^2 J_y J_z + 0.0007 J_x^3 J_z \\
p_{2,1,0} &= -0.0009 J_x^2 J_y - 0.0002 J_x^2 J_y J_z - 0.0045 J_x^2 J_y^2 + 0.0007 J_x^3 J_y \\
p_{-2,-2,0} &= -0.0001 J_x^2 J_y^2 \\
p_{-2,-1,-1} &= -0.0002 J_x^2 J_y J_z \\
p_{-2,0,-2} &= -0.0001 J_x^2 J_z^2 \\
p_{-1,-2,1} &= -0.0002 J_x J_y^2 J_z \\
p_{-1,1,-2} &= -0.0002 J_x J_y J_z^2 \\
p_{0,-2,2} &= -0.0001 J_y^2 J_z^2 \\
p_{0,2,-2} &= -0.0001 J_y^2 J_z^2 \\
p_{1,-1,2} &= -0.0002 J_x J_y J_z^2 \\
p_{1,2,-1} &= -0.0002 J_x J_y^2 J_z \\
p_{2,0,2} &= -0.0001 J_x^2 J_z^2 \\
p_{2,1,1} &= -0.0002 J_x^2 J_y J_z \\
p_{2,2,0} &= -0.0001 J_x^2 J_y^2
\end{aligned}
$$

B.2 One-particle channel of the observable

After investigating the hoppings for the Hamiltonian operator, in this section the terms for the observable are shown. As observable we use the (simple) local observable $O(i) = \sigma_i^z$, as defined in section 4.1.2. Keep in mind that we have to transform O before applying pCUT onto it according to the done rotation of the Hamiltonian, as stated in equation 4.1.9. In contrast to the last section, we do not calculate hoppings, as the quasi-particle number is not conserved anymore. As we restrict ourselves to the 1QP sector of the observable, we calculate terms of the form $\langle 1, j \mid \mathcal{O}_{\text{eff}}(i) \mid 0 \rangle$, where the effective observable is locally acting on site i, resulting in one quasi-particle at site j. We label the series analogously to the hoppings in the last section, having $o_{x,y,z}$ as the acting of the local observable at i with a resulting quasi-particle at position j, with a distance of bonds between i and j given by the three variables x, y, z. For the visualization of the positions we can again use figure B.1, with i being at the origin $p_{0,0,0}$ and j at the corresponding position $p_{x,y,z} \equiv o_{x,y,z}$.

$$
\begin{aligned}
o_{0,0,0} = {} & -0.8165 + 0.1571 J_z + 0.034 J_z^2 - 0.0182 J_z^3 - 0.0019 J_z^4 \\
& + (-0.0786 - 0.1361i) J_y + (-0.0605 + 0.0262i) J_y J_z + (0.0222 + 0.0132i) J_y J_z^2 \\
& + (0.0196 - 0.0047i) J_y J_z^3 + (0.0567 + 0.0393i) J_y^2 + (-0.0378 - 0.0239i) J_y^2 J_z \\
& + (-0.0063 - 0.013i) J_y^2 J_z^2 + (0.0047 + 0.0082i) J_y^3 + (0.0186 - 0.0002i) J_y^3 J_z \\
& + (-0.0075 - 0.0067i) J_y^4 + (-0.0786 + 0.1361i) J_x + (-0.0605 - 0.0262i) J_x J_z
\end{aligned}
$$

$$
\begin{aligned}
&+ (0.0222 - 0.0132i)J_x J_z^2 + (0.0196 + 0.0047i)J_x J_z^3 + 0.0756 J_x J_y \\
&+ 0.0349 J_x J_y J_z - 0.083 J_x J_y J_z^2 + (-0.0455 - 0.0599i)J_x J_y^2 \\
&+ (0.0525 + 0.0629i)J_x J_y^2 J_z + (-0.0035 + 0.0147i)J_x J_y^3 + (0.0567 - 0.0393i)J_x^2 \\
&+ (-0.0378 + 0.0239i)J_x^2 J_z + (-0.0063 + 0.013i)J_x^2 J_z^2 + (-0.0455 + 0.0599i)J_x^2 J_y \\
&+ (0.0525 - 0.0629i)J_x^2 J_y J_z + 0.0268 J_x^2 J_y^2 + (0.0047 - 0.0082i)J_x^3 \\
&+ (0.0186 + 0.0002i)J_x^3 J_z + (-0.0035 - 0.0147i)J_x^3 J_y + (-0.0075 + 0.0067i)J_x^4 \\
o_{0,-1,0} &= +(0.0393 - 0.068i)J_y + (-0.0302 + 0.0262i)J_y J_z + (-0.005 + 0.0066i)J_y J_z^2 \\
&+ (0.0045 - 0.0051i)J_y J_z^3 + (0.0227 + 0.0393i)J_y^2 + (-0.0007 - 0.0164i)J_y^2 J_z \\
&+ (0.0008 - 0.0126i)J_y^2 J_z^2 + (0.0031 + 0.0022i)J_y^3 + 0.0004 J_y^3 J_z \\
&+ (-0.0033 - 0.0056i)J_y^4 + (0.0378 - 0.0131i)J_x J_y + (0.0007 - 0.0063i)J_x J_y J_z \\
&+ (-0.0152 + 0.005i)J_x J_y J_z^2 + (-0.0269 - 0.0315i)J_x J_y^2 \\
&+ (0.0161 + 0.0337i)J_x J_y^2 J_z + (-0.0056 + 0.0141i)J_x J_y^3 \\
&+ (-0.0363 + 0.0324i)J_x^2 J_y + (0.0368 - 0.0205i)J_x^2 J_y J_z \\
&+ (0.0273 - 0.0087i)J_x^2 J_y^2 + (-0.0108 - 0.0035i)J_x^3 J_y \\
o_{0,0,-1} &= -0.0786 J_z + 0.0454 J_z^2 - 0.0018 J_z^3 - 0.0057 J_z^4 \\
&+ (-0.0076 - 0.0393i)J_y J_z + (-0.0204 + 0.0151i)J_y J_z^2 \\
&+ (0.0128 + 0.0052i)J_y J_z^3 + (-0.0057 + 0.0072i)J_y^2 J_z \\
&+ (0.0002 - 0.0163i)J_y^2 J_z^2 + (-0.0064 + 0.0024i)J_y^3 J_z \\
&+ (-0.0076 + 0.0393i)J_x J_z + (-0.0204 - 0.0151i)J_x J_z^2 \\
&+ (0.0128 - 0.0052i)J_x J_z^3 + 0.0073 J_x J_y J_z + 0.0148 J_x J_y J_z^2 \\
&+ (0.0062 - 0.0129i)J_x J_y^2 J_z + (-0.0057 - 0.0072i)J_x^2 J_z \\
&+ (0.0002 + 0.0163i)J_x^2 J_z^2 + (0.0062 + 0.0129i)J_x^2 J_y J_z \\
&+ (-0.0064 - 0.0024i)J_x^3 J_z \\
o_{1,0,0} &= +(0.0393 + 0.068i)J_x + (-0.0302 - 0.0262i)J_x J_z + (-0.005 - 0.0066i)J_x J_z^2 \\
&+ (0.0045 + 0.0051i)J_x J_z^3 + (0.0378 + 0.0131i)J_x J_y + (0.0007 + 0.0063i)J_x J_y J_z \\
&+ (-0.0152 - 0.005i)J_x J_y J_z^2 + (-0.0363 - 0.0324i)J_x J_y^2 \\
&+ (0.0368 + 0.0205i)J_x J_y^2 J_z + (-0.0108 + 0.0035i)J_x J_y^3 \\
&+ (0.0227 - 0.0393i)J_x^2 + (-0.0007 + 0.0164i)J_x^2 J_z \\
&+ (0.0008 + 0.0126i)J_x^2 J_z^2 + (-0.0269 + 0.0315i)J_x^2 J_y \\
&+ (0.0161 - 0.0337i)J_x^2 J_y J_z + (0.0273 + 0.0087i)J_x^2 J_y^2 \\
&+ (0.0031 - 0.0022i)J_x^3 + 0.0004 J_x^3 J_z + (-0.0056 - 0.0141i)J_x^3 J_y \\
&+ (-0.0033 + 0.0056i)J_x^4 \\
o_{-1,-1,0} &= +(0.0095 - 0.0033i)J_x J_y + (-0.0018 + 0.0032i)J_x J_y J_z \\
&+ (0.0003 - 0.003i)J_x J_y J_z^2 + (-0.0221 - 0.0202i)J_x J_y^2 \\
&+ (0.0177 + 0.0068i)J_x J_y^2 J_z + (-0.0053 + 0.0021i)J_x J_y^3 \\
&+ (-0.0047 + 0.0069i)J_x^2 J_y + (0.0054 - 0.0057i)J_x^2 J_y J_z \\
&+ (0.0122 + 0.0061i)J_x^2 J_y^2 + (-0.0006 - 0.0048i)J_x^3 J_y \\
o_{-1,0,-1} &= +(-0.0019 + 0.0098i)J_x J_z + (-0.0093 - 0.0019i)J_x J_z^2 \\
&+ (0.0015 - 0.0012i)J_x J_z^3 + (0.0047 - 0.0006i)J_x J_y J_z \\
&+ (0.0024 + 0.001i)J_x J_y J_z^2 + (0.0036 - 0.001i)J_x J_y^2 J_z \\
&+ (0.0029 - 0.0063i)J_x^2 J_z + (0.0009 + 0.0068i)J_x^2 J_z^2 \\
&+ (-0.003 + 0.0043i)J_x^2 J_y J_z + (0.0038 + 0.0001i)J_x^3 J_z
\end{aligned}
$$

$$
\begin{aligned}
o_{0,-1,1} &= +(-0.0019-0.0033i)J_yJ_z+(-0.0004+0.0019i)J_yJ_z^2\\
&\quad+(0.0019+0.0018i)J_yJ_z^3+(-0.021+0.0044i)J_y^2J_z\\
&\quad+(0.0085-0.009i)J_y^2J_z^2+(-0.0043-0.0028i)J_y^3J_z+0.0036J_xJ_yJ_z\\
&\quad+(-0.0055-0.0016i)J_xJ_yJ_z^2+(0.0144+0.0033i)J_xJ_y^2J_z\\
&\quad+(0.0065-0.0018i)J_x^2J_yJ_z\\
o_{0,1,-1} &= +(-0.0019-0.0098i)J_yJ_z+(-0.0093+0.0019i)J_yJ_z^2\\
&\quad+(0.0015+0.0012i)J_yJ_z^3+(0.0029+0.0063i)J_y^2J_z\\
&\quad+(0.0009-0.0068i)J_y^2J_z^2+(0.0038-0.0001i)J_y^3J_z\\
&\quad+(0.0047+0.0006i)J_xJ_yJ_z+(0.0024-0.001i)J_xJ_yJ_z^2\\
&\quad+(-0.003-0.0043i)J_xJ_y^2J_z+(0.0036+0.001i)J_x^2J_yJ_z\\
o_{1,0,1} &= +(-0.0019+0.0033i)J_xJ_z+(-0.0004-0.0019i)J_xJ_z^2\\
&\quad+(0.0019-0.0018i)J_xJ_z^3+0.0036J_xJ_yJ_z+(-0.0055+0.0016i)J_xJ_yJ_z^2\\
&\quad+(0.0065+0.0018i)J_xJ_y^2J_z+(-0.021-0.0044i)J_x^2J_z\\
&\quad+(0.0085+0.009i)J_x^2J_z^2+(0.0144-0.0033i)J_x^2J_yJ_z\\
&\quad+(-0.0043+0.0028i)J_x^3J_z\\
o_{1,1,0} &= +(0.0095+0.0033i)J_xJ_y+(-0.0018-0.0032i)J_xJ_yJ_z\\
&\quad+(0.0003+0.003i)J_xJ_yJ_z^2+(-0.0047-0.0069i)J_xJ_y^2\\
&\quad+(0.0054+0.0057i)J_xJ_y^2J_z+(-0.0006+0.0048i)J_xJ_y^3\\
&\quad+(-0.0221+0.0202i)J_x^2J_y+(0.0177-0.0068i)J_x^2J_yJ_z\\
&\quad+(0.0122-0.0061i)J_x^2J_y^2+(-0.0053-0.0021i)J_x^3J_y\\
o_{-1,-2,0} &= -0.0003iJ_xJ_y^2+(-0.0005+0.0019i)J_xJ_y^2J_z+(0.0028+0.0032i)J_xJ_y^3\\
&\quad+(0.0027-0.0018i)J_x^2J_y^2\\
o_{-1,-1,-1} &= +(0.0033+0.0032i)J_xJ_yJ_z+(-0.0007-0.0006i)J_xJ_yJ_z^2\\
&\quad+(0.0034-0.0017i)J_xJ_y^2J_z+(0.0022+0.0003i)J_x^2J_yJ_z\\
o_{-1,0,-2} &= +(-0.0005+0.0006i)J_xJ_z^2+(0.0019-0.0003i)J_xJ_z^3\\
&\quad+(0.0014-0.0013i)J_xJ_yJ_z^2+(0.0003+0.0002i)J_x^2J_z^2\\
o_{0,-2,1} &= -0.0005J_y^2J_z+(0.0032-0.001i)J_y^2J_z^2\\
&\quad+(0.0047-0.0008i)J_y^3J_z+(0.0001+0.0002i)J_xJ_y^2J_z\\
o_{0,1,-2} &= +(-0.0005-0.0006i)J_yJ_z^2+(0.0019+0.0003i)J_yJ_z^3\\
&\quad+(0.0003-0.0002i)J_y^2J_z^2+(0.0014+0.0013i)J_xJ_yJ_z^2\\
o_{1,-1,1} &= -0.0022J_xJ_yJ_z+0.0029J_xJ_yJ_z^2+(0.0058+0.0041i)J_xJ_y^2J_z\\
&\quad+(0.0058-0.0041i)J_x^2J_yJ_z\\
o_{1,1,-1} &= +(0.0033-0.0032i)J_xJ_yJ_z+(-0.0007+0.0006i)J_xJ_yJ_z^2\\
&\quad+(0.0022-0.0003i)J_xJ_y^2J_z+(0.0034+0.0017i)J_x^2J_yJ_z\\
o_{2,0,1} &= -0.0005J_x^2J_z+(0.0032+0.001i)J_x^2J_z^2\\
&\quad+(0.0001-0.0002i)J_x^2J_yJ_z+(0.0047+0.0008i)J_x^3J_z\\
o_{2,1,0} &= +0.0003iJ_x^2J_y+(-0.0005-0.0019i)J_x^2J_yJ_z\\
&\quad+(0.0027+0.0018i)J_x^2J_y^2+(0.0028-0.0032i)J_x^3J_y\\
o_{-2,-2,0} &= -0.0001iJ_x^2J_y^2\\
o_{-2,-1,-1} &= +(0.0002+0.0002i)J_x^2J_yJ_z\\
o_{-2,0,-2} &= +(-0.0001+0.0001i)J_x^2J_z^2\\
o_{-1,-2,1} &= +(-0.0002-0.0002i)J_xJ_y^2J_z
\end{aligned}
$$

$$
\begin{aligned}
o_{-1,1,-2} &= -0.0004 J_x J_y J_z^2 \\
o_{0,-2,2} &= -0.0001 J_y^2 J_z^2 \\
o_{0,2,-2} &= +(-0.0001 - 0.0001i) J_y^2 J_z^2 \\
o_{1,-1,2} &= -0.0002 J_x J_y J_z^2 \\
o_{1,2,-1} &= +(0.0002 - 0.0002i) J_x J_y^2 J_z \\
o_{2,0,2} &= -0.0001 J_x^2 J_z^2 \\
o_{2,1,1} &= +(-0.0002 + 0.0002i) J_x^2 J_y J_z \\
o_{2,2,0} &= +0.0001i J_x^2 J_y^2
\end{aligned}
$$

Index

Bibliography

[1] H. Bruns. Über die Integrale des Vielkörper-Problems. *Acta Mathematica*, 11:25 – 96, 1900. doi: 10.1007/BF02612319. URL `https://doi.org/10.1007/BF02612319`.

[2] Stephen Wolfram. *A New Kind of Science*. Wolfram Media, 2002. URL `https://www.wolframscience.com/nks/`.

[3] R. Broucke and D. Boggs. Periodic orbits in the planar general three-body problem. *Celestial mechanics*, 1975. doi: 10.1007/BF01228732. URL `https://doi.org/10.1007/BF01228732`.

[4] Richard Montgomery. A new solution to the three-body problem. *Notices of the American Mathematical Society*, 48, 2001.

[5] Milovan Šuvakov and V. Dmitrašinović. Three classes of newtonian three-body planar periodic orbits. *Physical Review Letters*, 110(11), 2013. ISSN 1079-7114. doi: 10.1103/physrevlett.110.114301. URL `http://dx.doi.org/10.1103/PhysRevLett.110.114301`.

[6] Carl D. Murray and Stanley F. Dermott. *The Restricted Three-Body Problem*, page 63–129. Cambridge University Press, 2000. doi: 10.1017/CBO9781139174817.004.

[7] Norbert Straumann. *Quantenmechanik - Ein Grundkurs über nichtrelativistische Quantentheorie*. Springer-Verlag Berlin Heidelberg, 2013. doi: 10.1007/978-3-642-32175-7.

[8] Piers Coleman. *Introduction to Many-Body Physics*. Cambridge University Press, 2015. doi: 10.1017/CBO9781139020916.

[9] Christian Knetter. *Perturbative Continuous Unitary Transformations: Spectral Properties of Low Dimensional Spin Systems*. PhD thesis, Universität zu Köln, 2003. URL `https://kups.ub.uni-koeln.de/942/`.

[10] Rodney J. Baxter. *Exactly Solved Models in Statistical Mechanics*. Elsevier, Amsterdam, 2016. ISBN 978-1-483-26594-0.

[11] Franz J. Wegner. Flow equations for hamiltonians. *Physics Reports*, 348(1):77–89, 2001. ISSN 0370-1573. doi: https://doi.org/10.1016/S0370-1573(00)00136-8. URL `https://www.sciencedirect.com/science/article/pii/S0370157300001368`. Renormalization group theory in the new millennium. II.

[12] Kai Phillip Schmidt. *Spectral properties of quasi one-dimensional quantum antiferromagnets perturbative continuous unitary transformations.* PhD thesis, Köln, Univ., 2004. URL `http://kups.ub.uni-koeln.de/volltexte/2004/1316/pdf/Diss2.pdf`.

[13] Alexei Kitaev. Anyons in an exactly solved model and beyond. *Annals of Physics*, 321(1):2–111, 2006. ISSN 0003-4916. doi: 10.1016/j.aop.2005.10.005. URL `http://dx.doi.org/10.1016/j.aop.2005.10.005`.

[14] Matthias Gohlke, Roderich Moessner, and Frank Pollmann. Dynamical and topological properties of the Kitaev model in a [111] magnetic field. *Phys. Rev. B*, 98:014418, 2018. doi: 10.1103/PhysRevB.98.014418. URL `https://link.aps.org/doi/10.1103/PhysRevB.98.014418`.

[15] Saptarshi Mandal and Arun M Jayannavar. An introduction to Kitaev model-I, 2020.

[16] Zheng Zhu, Itamar Kimchi, D. N. Sheng, and Liang Fu. Robust non-abelian spin liquid and a possible intermediate phase in the antiferromagnetic Kitaev model with magnetic field. *Phys. Rev. B*, 97:241110, 2018. doi: 10.1103/PhysRevB.97.241110. URL `https://link.aps.org/doi/10.1103/PhysRevB.97.241110`.

[17] Ciarán Hickey and Simon Trebst. Emergence of a field-driven u(1) spin liquid in the Kitaev honeycomb model. *Nature Communications*, 10(530), 2019. doi: 10.1038/s41467-019-08459-9. URL `https://doi.org/10.1038/s41467-019-08459-9`.

[18] Liujun Zou and Yin-Chen He. Field-induced qcd3-chern-simons quantum criticalities in Kitaev materials. *Physical Review Research*, 2(1), 2020. ISSN 2643-1564. doi: 10.1103/physrevresearch.2.013072. URL `http://dx.doi.org/10.1103/PhysRevResearch.2.013072`.

[19] Christoph Berke, Simon Trebst, and Ciarán Hickey. Field stability of Majorana spin liquids in antiferromagnetic Kitaev models. *Physical Review B*, 101(21), 2020. ISSN 2469-9969. doi: 10.1103/physrevb.101.214442. URL `http://dx.doi.org/10.1103/PhysRevB.101.214442`.

[20] F. Trousselet, A. M. Oleś, and P. Horsch. Compass-Heisenberg model on the square lattice —spin order and elementary excitations. *EPL (Europhysics Letters)*, 91(4):40005, 2010. ISSN 1286-4854. doi: 10.1209/0295-5075/91/40005. URL `http://dx.doi.org/10.1209/0295-5075/91/40005`.

[21] Shang-Shun Zhang, Gábor B. Halász, and Cristian D. Batista. Theory of the Kitaev model in a [111] magnetic field, 2021.

[22] Ciarán Hickey, Matthias Gohlke, Christoph Berke, and Simon Trebst. Generic field-driven phenomena in Kitaev spin liquids: Canted magnetism and proximate spin liquid physics. *Physical Review B*, 103(6), 2021. ISSN 2469-9969. doi: 10.1103/physrevb.103.064417. URL `http://dx.doi.org/10.1103/PhysRevB.103.064417`.

[23] Elliott H. Lieb. Flux phase of the half-filled band. *Physical Review Letters*, 73(16):2158–2161, 1994. ISSN 0031-9007. doi: 10.1103/physrevlett.73.2158. URL `http://dx.doi.org/10.1103/PhysRevLett.73.2158`.

[24] Frank Arute et al. Quantum supremacy using a programmable superconducting processor. *Nature*, 574, 2019. doi: 10.1038/s41586-019-1666-5. URL `https://doi.org/10.1038/s41586-019-1666-5`.

[25] Nicolai Friis, Oliver Marty, Christine Maier, Cornelius Hempel, Milan Holzäpfel, Petar Jurcevic, Martin B. Plenio, Marcus Huber, Christian Roos, Rainer Blatt, and et al. Observation of entangled states of a fully controlled 20-qubit system. *Physical Review X*, 8(2), Apr 2018. ISSN 2160-3308. doi: 10.1103/physrevx.8.021012. URL `http://dx.doi.org/10.1103/PhysRevX.8.021012`.

[26] Davide Castelvecchi. Quantum computers ready to leap out of the lab in 2017. *Nature*, 541, 2017. doi: 10.1038/541009a. URL `https://doi.org/10.1038/541009a`.

[27] Ciarán Hickey, Matthias Gohlke, Christoph Berke, and Simon Trebst. Generic field-driven phenomena in Kitaev spin liquids: Canted magnetism and proximate spin liquid physics. *Phys. Rev. B*, 103:064417, 2021. doi: 10.1103/PhysRevB.103.064417. URL `https://link.aps.org/doi/10.1103/PhysRevB.103.064417`.

[28] I. M. Georgescu, S. Ashhab, and Franco Nori. Quantum simulation. *Rev. Mod. Phys.*, 86:153–185, 2014. doi: 10.1103/RevModPhys.86.153. URL `https://link.aps.org/doi/10.1103/RevModPhys.86.153`.

[29] Ehud Altman, Kenneth R. Brown, Giuseppe Carleo, Lincoln D. Carr, Eugene Demler, Cheng Chin, Brian DeMarco, Sophia E. Economou, Mark A. Eriksson, Kai-Mei C. Fu, Markus Greiner, Kaden R.A. Hazzard, Randall G. Hulet, Alicia J. Kollár, Benjamin L. Lev, Mikhail D. Lukin, Ruichao Ma, Xiao Mi, Shashank Misra, Christopher Monroe, Kater Murch, Zaira Nazario, Kang-Kuen Ni, Andrew C. Potter, Pedram Roushan, Mark Saffman, Monika Schleier-Smith, Irfan Siddiqi, Raymond Simmonds, Meenakshi Singh, I.B. Spielman, Kristan Temme, David S. Weiss, Jelena Vučković, Vladan Vuletić, Jun Ye, and Martin Zwierlein. Quantum simulators: Architectures and opportunities. *PRX Quantum*, 2:017003, 2021. doi: 10.1103/PRXQuantum.2.017003. URL `https://link.aps.org/doi/10.1103/PRXQuantum.2.017003`.

[30] Tatiana A. Bespalova and Oleksandr Kyriienko. Quantum simulation and ground state preparation for the honeycomb Kitaev model, 2021.

[31] Zheng Zhu, Zheng-Yu Weng, and D. N. Sheng. Magnetic field induced spin liquids in s=1 Kitaev honeycomb model. *Phys. Rev. Research*, 2: 022047, 2020. doi: 10.1103/PhysRevResearch.2.022047. URL `https://link.aps.org/doi/10.1103/PhysRevResearch.2.022047`.

[32] Ciarán Hickey, Christoph Berke, Panagiotis Peter Stavropoulos, Hae-Young Kee, and Simon Trebst. Field-driven gapless spin liquid in the spin-1 Kitaev honeycomb model. *Phys. Rev. Research*, 2:023361, 2020.

doi: 10.1103/PhysRevResearch.2.023361. URL `https://link.aps.org/doi/10.1103/PhysRevResearch.2.023361`.

[33] Hui-Ke Jin, W. M. H. Natori, F. Pollmann, and J. Knolle. Unveiling the s=3/2 Kitaev honeycomb spin liquids, 2021.

[34] T. Matsubara and H. Matsuda. A lattice model of liquid helium. *Progress of Theoretical Physics*, 16:416–417, 1956.

[35] C. Knetter and Götz Uhrig. Perturbation theory by flow equations: Dimerized and frustrated s = 1/2 chain. *The European Physical Journal B - Condensed Matter and Complex Systems*, 13, 2000. doi: 10.1007/s100510050026. URL `https://doi.org/10.1007/s100510050026`.

[36] Patrick Adelhardt. Quantum criticality of long-range generalized quantum spin systems. Master's thesis, Friedrich-Alexander-Universität Erlangen-Nürnberg, 2020.

[37] Kris Cöster. *Quasiparticle pictures and graphs - from perturbative to non-perturbative linked-cluster expansions.* PhD thesis, TU Dortmund University, 2015.

[38] Martin Gelfand, Rajiv Singh, and David Huse. Perturbation expansions for quantum many-body systems. *Journal of Statistical Physics*, 59:1093–1142, 1990. doi: 10.1007/BF01334744.

[39] Sébastien Dusuel, Michael Kamfor, Kai Phillip Schmidt, Ronny Thomale, and Julien Vidal. Bound states in two-dimensional spin systems near the Ising limit: A quantum finite-lattice study. *Physical Review B*, 81 (6), 2010. ISSN 1550-235X. doi: 10.1103/physrevb.81.064412. URL `http://dx.doi.org/10.1103/PhysRevB.81.064412`.

[40] Patrick Adelhardt, Jan Alexander Koziol, Andreas Schellenberger, and Kai Phillip Schmidt. Quantum criticality and excitations of a long-range anisotropic xy chain in a transverse field. *Physical Review B*, 102 (17), 2020. ISSN 2469-9969. doi: 10.1103/physrevb.102.174424. URL `http://dx.doi.org/10.1103/PhysRevB.102.174424`.

[41] C. Knetter, K. P. Schmidt, and G. S. Uhrig. High order perturbation theory for spectral densities of multi-particle excitations: S = 1/2 two-leg Heisenberg ladder. *The European Physical Journal B - Condensed Matter*, 36(4):525–544, 2003. ISSN 1434-6036. doi: 10.1140/epjb/e2004-00008-2. URL `http://dx.doi.org/10.1140/epjb/e2004-00008-2`.

[42] C. Knetter, K. P. Schmidt, M. Grüninger, and G. S. Uhrig. Fractional and integer excitations in quantum antiferromagnetic spin 1/2 ladders. *Phys. Rev. Lett.*, 87:167204, 2001. doi: 10.1103/PhysRevLett.87.167204. URL `https://link.aps.org/doi/10.1103/PhysRevLett.87.167204`.

[43] Richard P. Feynman. *The Feynman lectures on physics.* Reading, Mass.: Addison-Wesley Pub. Co., 1963-1965. URL `https://www.feynmanlectures.caltech.edu/info/`.

[44] Silvia Viola Kusminskiy. *Quantum Magnetism, Spin Waves, and Optical Cavities*. Springer International Publishing, 2019. doi: 10.1007/978-3-030-13345-0.

[45] George A. Baker and Peter Graves-Morris. *Padé Approximants*. Encyclopedia of Mathematics and its Applications. Cambridge University Press, 2 edition, 1996. doi: 10.1017/CBO9780511530074.

[46] W.H. Press, S.A. Teukolsky, W.T. Vetterling, and B.P. Flannery. *Numerical Recipes 3rd Edition: The Art of Scientific Computing*. Cambridge University Press, 2007. ISBN 9780521880688. URL `https://www.cambridge.org/de/academic/subjects/mathematics/numerical-recipes/numerical-recipes-art-scientific-computing-3rd-edition?format=HB`.

[47] Sebastian Fey. Field-driven instabilities of the non-abelian topological phase in the Kitaev model. Master's thesis, Technische Universität Dortmund, 2013.

[48] L. Lenke, M. Mühlhauser, and K. P. Schmidt. High-order series expansion of non-hermitian quantum spin models, 2021.

[49] Max Hörmann and Kai Phillip Schmidt. Dynamic structure factor of Heisenberg bilayer dimer phases in the presence of quenched disorder and frustration. *Physical Review B*, 102(9), 2020. ISSN 2469-9969. doi: 10.1103/physrevb.102.094427. URL `http://dx.doi.org/10.1103/PhysRevB.102.094427`.

[50] M. Mühlhauser, M. R. Walther, D. A. Reiss, and K. P. Schmidt. Quantum robustness of fracton phases. *Physical Review B*, 101(5), 2020. ISSN 2469-9969. doi: 10.1103/physrevb.101.054426. URL `http://dx.doi.org/10.1103/PhysRevB.101.054426`.

[51] Sebastian Fey, Sebastian C. Kapfer, and Kai Phillip Schmidt. Quantum criticality of two-dimensional quantum magnets with long-range interactions. *Physical Review Letters*, 122(1), 2019. ISSN 1079-7114. doi: 10.1103/physrevlett.122.017203. URL `http://dx.doi.org/10.1103/PhysRevLett.122.017203`.

[52] Joji Nasu, Yasuyuki Kato, Yoshitomo Kamiya, and Yukitoshi Motome. Successive Majorana topological transitions driven by a magnetic field in the Kitaev model. *Physical Review B*, 98(6), 2018. ISSN 2469-9969. doi: 10.1103/physrevb.98.060416. URL `http://dx.doi.org/10.1103/PhysRevB.98.060416`.

[53] Wen-Long You, Peter Horsch, and Andrzej M. Oleś. Quantum phase transitions in exactly solvable one-dimensional compass models. *Phys. Rev. B*, 89:104425, 2014. doi: 10.1103/PhysRevB.89.104425. URL `https://link.aps.org/doi/10.1103/PhysRevB.89.104425`.

[54] Steven R. White. Density matrix formulation for quantum renormalization groups. *Phys. Rev. Lett.*, 69:2863–2866, 1992. doi: 10.1103/PhysRevLett.69.2863. URL `https://link.aps.org/doi/10.1103/PhysRevLett.69.2863`.

[55] Karen A. Hallberg. New trends in density matrix renormalization. *Advances in Physics*, 55(5-6):477–526, 2006. ISSN 1460-6976. doi: 10.1080/00018730600766432. URL `http://dx.doi.org/10.1080/00018730600766432`.

[56] P. Adelhardt, J. Gritsch, M. Hille, D. A. Reiss, and K. P. Schmidt. Quantum phase transitions to topological Haldane phases in spin-one chains studied by linked-cluster expansions. *Physical Review B*, 96(23), 2017. ISSN 2469-9969. doi: 10.1103/physrevb.96.235123. URL `http://dx.doi.org/10.1103/PhysRevB.96.235123`.

[57] K. Coester and K. P. Schmidt. Optimizing linked-cluster expansions by white graphs. *Physical Review E*, 92(2), 2015. ISSN 1550-2376. doi: 10.1103/physreve.92.022118. URL `http://dx.doi.org/10.1103/PhysRevE.92.022118`.

[58] K. Coester, W. Malitz, S. Fey, and K. P. Schmidt. Quantum disorder and local modes of the fully-frustrated transverse field Ising model on a diamond chain. *Physical Review B*, 88(18), 2013. ISSN 1550-235X. doi: 10.1103/physrevb.88.184402. URL `http://dx.doi.org/10.1103/PhysRevB.88.184402`.

[59] G. Rücker and C. Rücker. Automatic enumeration of all connected subgraphs. *MATCH Communications in Mathematical and in Computer Chemistry*, pages 145–149, 2000.

Acknowledgments

At the end of this thesis—and with this also at the end of a good bunch of work—I want to say 'Thank you' to some people in and all around university who helped me during the time of this thesis.

The first and most important 'thanks' goes to Kai Schmidt, giving me the topic for this thesis attached with a bunch of papers, theses, and information, but also always supporting and advising me at all stages of the work. I found this close support not self-evident and I am thankful and impressed by the commitment Kai is investing for all people in this group. Not enough having one advisor, I had two. Thank you Max for a lot of text messages we exchanged with each other for answering questions to various topics for this thesis. The option to get an answer within short time was a good compensation for the lack of casual meetings during this time of home office. Also thanks to the whole group for the pleasant atmosphere, even as there sadly was not a lot of 'normal office time' during the last year.

Leaving university (virtually), I want to thank family (and newly family-in-law), friends, and people at church, SMD, and sports for being the 'other part' of life apart from studying. I am very thankful being surrounded by all of you. This time of the master's thesis will stay connected to my wedding and the beginning of the married life. Sophia, I am very happy for this coincidence, all your help during this time, and being a nice and special neighbor in home-office.

Lastly, I want to thank all kinds of talented composers who sweetened the time working on this thesis by their orchestral sounds. Even if it might not be the case for the one not hearing the heroic drums and majestic strings: If you are coding while listening, each line of code feels epic.

Eidesstattliche Versicherung

Hiermit versichere ich, dass ich die vorliegende Arbeit selbstständig verfasst und keine anderen als die angegebenen Quellen und Hilfsmittel benutzt habe, dass alle Stellen der Arbeit, die wörtlich oder sinngemäß aus anderen Quellen übernommen wurden, als solche kenntlich gemacht sind und dass die Arbeit in gleicher oder ähnlicher Form noch keiner Prüfungsbehörde vorgelegt wurde.

Erlangen, den 1. November 2021 Andreas Schellenberger